Karlsruhe Institute of Technology

Faculty of Physics
Institute of Astroparticle Physics

Characterization and commissioning of a cold trap for the KATRIN experiment

Master Thesis
of

Marcel Walter

at the Institute of Astroparticle Physics

Reviewer:	Prof. Dr. Guido Drexlin
Second Reviewer:	Prof. Dr. Kathrin Valerius
Advisor:	Dr. Carsten Röttele

Bearbeitungszeit: 01.09.2019 – 06.10.2020

Declaration of authorship

With this declaration, I declare that I have written this dissertation on my own and have not used any other sources and tools than those indicated. All passages of the work which have been taken over literally or analogously from other sources are marked as such. This thesis has not yet been submitted to any audit authority in the same or similar form.

Erklärung zur Selbstständigkeit

Ich versichere, dass ich diese Arbeit selbstständig verfasst habe und keine anderen als die angegebenen Quellen und Hilfsmittel benutzt habe, die wörtlich oder inhaltlich übernommenen Stellen als solche kenntlich gemacht und die Satzung des KIT zur Sicherung guter wissenschaftlicher Praxis in der gültigen Fassung vom 27.11.2014 beachtet habe.

Karlsruhe, den 06.10.2020, _____

Marcel Walter

Als Prüfungsexemplar genehmigt von

Karlsruhe, den 06.10.2020, _____

Prof. Dr. Guido Drexlin

Contents

List of Figures

List of Tables

1. Introduction

In neutrino physics, great efforts have been made to determine the mass of the neutrino since they were postulated by Wolfgang Pauli in 1930 [Pau64]. Neutrinos play a major role in astrophysics and are important for our understanding of particle physics. It is known that neutrinos are massive since the discovery of neutrino oscillation in 1998 [FHI+98]. This is in contrast to the standard model of particle physics. Therefore, experiments like the KArsruher TRItium Neutrino experiment (KATRIN) try to determine the effective neutrino mass model-independently by investigating the β-decay spectrum of tritium.

The Magnetic Adiabatic Collimation with Electrostatic filter (MAC-E filter) concept [AAB05] with a windowless tritium gas source is applied at KATRIN to determine the endpoint energy region of the β-decay of molecular tritium, and thus the neutrino mass with a designed sensitivity of 0.2 eV. This concept requires an extremely stable and well-determined tritium gas source.

In this thesis, a cold trap, designed to remove impurities from gas stream injected into the windowless gaseous tritium source, is examined and commissioned. Therefore, the cold trap was tested to investigate the reduction of methane from a deuterium flow at an operational temperature of 30 K using cryo pumping. If this test with a non-radioactive gas is successful, it can be installed in the tritium injection system of KATRIN. Furthermore, the conductance of the cold trap is determined in order to find the operational design parameters.

The thesis is structured as follows:

The basic principles of neutrino physics are explained in chapter 2. The discovery of the neutrino and the problems of early neutrino models are presented. Furthermore, the discovery of the neutrino oscillation and the introduction of methods to determine the mass of the neutrino are discussed.

Chapter 3 introduces the KATRIN experiment with the setup, the main functions and their physical foundation.

In chapter 4, the fundamental theories of cryopumping and fluid dynamics are explained, which will be applied to determine the characteristics of the cold trap. Therefore, an overview of the different pumping phenomenons is given including the characteristics of a cryopump, and the basic theory for the determination of the conductance.

Chapter 5 introduces the cold trap and the experimental test setup for conductance and reduction measurements. Furthermore, considerations are made about the thermal load, the impact of the accumulated methane during operation on the pumping capacity and conductance, as well as the different flow conditions during operation.

The conductance of the cold trap is determined in chapter 6 by measuring at different flow and temperature conditions and gases. The measurement results are verified with simulation data and theoretical models.

The reduction capabilities of the cold trap are analyzed in chapter 7. The cold trap was tested with a methane-deuterium mixture, as well as methane and deuterium separately. Furthermore, tests are executed under different temperatures in order to verify the reduction measurements and test the temperature behavior of the cold trap.

Chapter 8 summarizes the thesis and gives an outlook for possible application scenarios.

2. Introduction to neutrino physics

Neutrinos are the lightest massive particles known and of high interest for particle- and astrophysics.

Neutrinos are important for our understanding of the processes in stars, supernovae, forming of galaxies, etc.. The neutrino mass is relevant in many of these models, and therefore the subject of many investigations. Measuring the neutrino mass is a great challenge due to its low interaction rate. In the following, the basic physical background and principles of neutrino physics are introduced.

2.1. The discovery of the neutrino

With the discovery of the β^--decay and the continuous β-spectrum, by James Chadwick in 1914 [Cha14], there was a first experimental hint for a new particle. The energy spectrum for a two-body decay should result in a discrete peak analog to the α-decay spectrum, which was already known at that time. Therefore, a continuous spectrum would be a violation of the energy conservation law.

A new light electrical neutral particle with spin $\frac{1}{2}$ was postulated by Pauli in his letter to Enrico Fermi in 1930, the neutrino [Pau64]. The two-body decay becomes a three-body decay with this particle and the continuous β-spectrum agrees with the energy conversation law:

$$\mathrm{n} \rightarrow \mathrm{p} + \mathrm{e}^- + \overline{\nu_\mathrm{e}} \,. \tag{2.1}$$

The first observation of the neutrino was made by the Cowan-Reines-Neutrino experiment in 1956 [CRH$^+$56]. It used a nuclear reactor emitting a high flux of electron-antineutrinos $\overline{\nu}_\mathrm{e}$. In the detector the antineutrino can be observed by the products of an inverse β-decay:

$$\overline{\nu}_\mathrm{e} + \mathrm{p} \rightarrow \mathrm{e}^+ + \mathrm{n} \,. \tag{2.2}$$

The products of the β-decay were detected as a delayed pulse pair by hydrogen liquid scintillator, which contained a high number of target protons. The first pulse was the slowing down and annihilation of the e^+, which emitted two γ's with an energy of 0.511 MeV. The second pulse was the capture of the moderated neutron by cadmium dissolved in the scintillator. The coincidence of the two signals was proof of the inverse β-decay and thus of the electron neutrino.

In addition to the electron neutrino, there are two more flavors known today: The muon and tau neutrino. The ν_μ was discovered by Leon M. Lederman, Melvin Schwartz, and Jack Steinberger at the Brookhaven National Laboratory in 1962 [DGG$^+$62]. In their experiment, high energy protons from a particle accelerator stroke a beryllium target and produced pions. The particles hit an iron shielding placed 21 m behind the target, which absorbed muons, pions, and neutrons. The neutrinos passed through and were observed in the 10 t aluminum spark chamber behind the shielding.

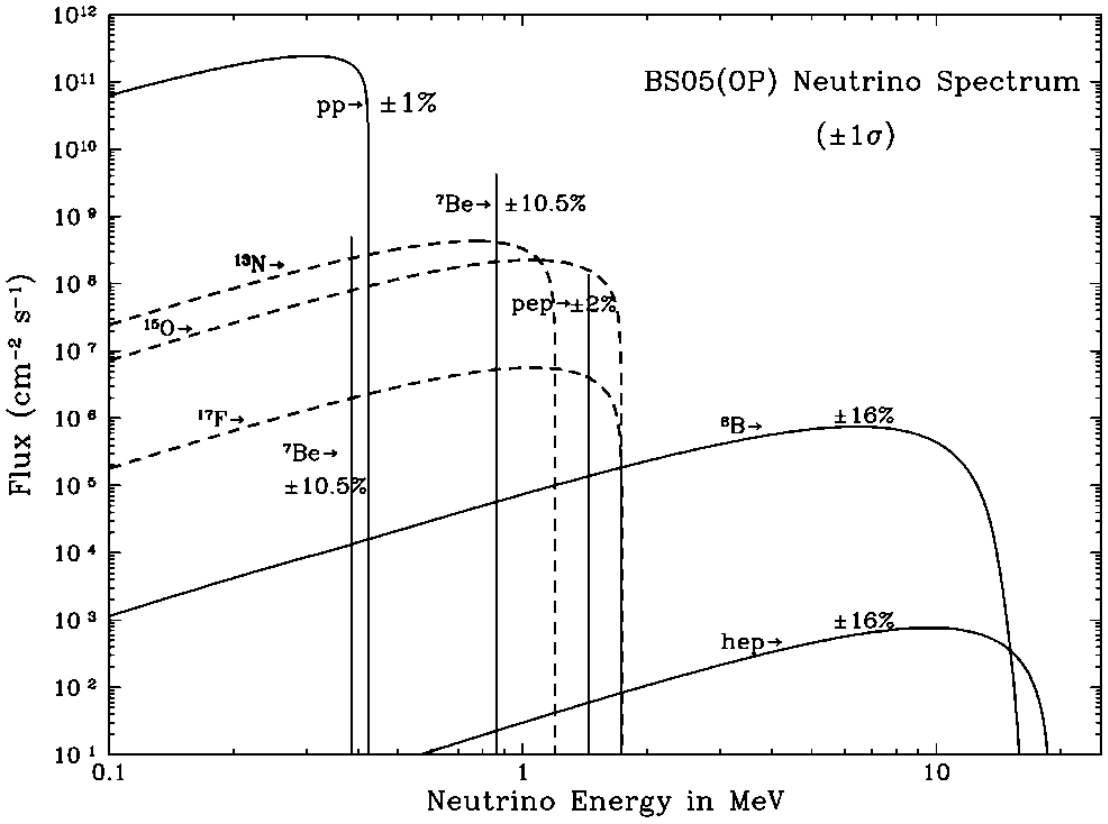

Figure 2.1.: Standard Solar Model: Energy spectrum of solar neutrinos created by reactions in the sun for different processes (pp, ^{7}Be, etc.) The figure is taken from [BSB05].

The tau neutrino was postulated by Martin Lewis Perl in 1975 [PAB+75]. During experiments at the Stanford Linear Accelerator Center - Lawrence Berkeley Laboratory (SLAC-LBL) magnetic detector at the SLAC colliding-beams facility SPEAR with a center-of-mass-energy $\geq 4\,\mathrm{GeV}$, it was found:

$$\mathrm{e}^+ + \mathrm{e}^- \rightarrow \mathrm{e}^\pm + \mu^\mp + \text{missing energy}. \tag{2.3}$$

The tau neutrino was discovered by the DONUT experiment in 2001 [KUA+01]. DONUT used the 800 GeV proton beam from the Fermi Lab Tevatron to produce tau neutrinos via decay of charmed mesons. A nuclear emulsion was used as the target. The tau neutrino was expected to decay within 2 mm after its creation to a single charged daughter. The resulting track with kink characterizes a decay with large transverse momentum. The emulsion was used to analyze the tracks.

2.2. The solar neutrino problem

The solar neutrino problem describes a deficit in the neutrino flux of the sun, predicted by the standard solar model (SSM) by Bahcall [Bah64] shown in figure 2.1. The neutrino flux of different energies originates from the different fusion processes of the sun, which starts at the pp reaction given by:

$$\mathrm{p} + \mathrm{p} \rightarrow {}^2\mathrm{H} + \mathrm{e}^+ + \nu_\mathrm{e}\,. \tag{2.4}$$

The Homestake experiment [DHH68] aimed to confirm the predicted neutrino flux of the SSM. It was sensitive to the ^{8}B and ^{7}Be solar electron neutrinos. The measurements

showed that the flux for ^{8}B-neutrinos is a factor 3 below the expected flux [Dav94] for the SSM.

Homestake was only sensitive to electron neutrinos. It was not possible to determine the energy, direction, or arrival time of the neutrino due to its experimental setup. Other experiments like (Super)-Kamiokande and SNO are based on the detection of Cerenkov light. This method is sensitive to all neutrino flavors and allows to measure the number of neutrinos passing through the detector volume, the direction, energy, and time coordinate. The total neutrino flux of all three flavors matched the expected flux of ν_e. It was possible to confirm the solar neutrino problem and the MSW effect with these measurements. This effect explains that the effective mass of the flavor eigenstates depends on the propagation through the mass. [Wol78, MS86]

2.3. Neutrino oscillation

The observation of neutrino oscillation was the first proof that neutrinos have mass. It was postulated in 1957 by Bruno Pontecorvo [Pon68]. The so called "solar neutrino problem" was the first observational hint, it was discovered in the 1970's by the Homestake-Experiment and confirmed in 1998 by Super-Kamiokande and SNO. The lower limit of the neutrino mass was determined by these experiments with 0.01 eV.[FHI$^+$98, AAA$^+$01].

Theoretical description of the neutrino oscillation parameters

In order to understand the neutrino oscillation, a simplified two flavor oscillation can be derived analog to the well known CKM-matrix. For the two generations ν_e and ν_μ:

$$\begin{pmatrix} |\nu_e\rangle \\ |\nu_\mu\rangle \end{pmatrix} = \begin{pmatrix} \cos\theta & \sin\theta \\ -\sin\theta & \cos\theta \end{pmatrix} \cdot \begin{pmatrix} |\nu_1\rangle \\ |\nu_2\rangle \end{pmatrix}. \tag{2.5}$$

The disappearance probability is [Per08]:

$$P(\nu_e \to \nu_e) = 1 - \sin^2 2\theta \cdot \sin^2\left(1.27 \cdot \Delta m^2_{21} \cdot \frac{L}{E}\right), \tag{2.6}$$

with the difference of the square masses of the eigenstates ν_1 and ν_2:

$$\Delta m^2_{21} = \Delta m^2 = m^2_{\nu_1} - m^2_{\nu_2}\ . \tag{2.7}$$

The appearance probability is $P(\nu_e \to \nu_\mu) = 1 - P(\nu_e \to \nu_e)$. L is the flight distance of the neutrino. Hence, the oscillation length λ is given by:

$$\lambda = 2.5 \cdot \frac{E}{\Delta m^2}\ . \tag{2.8}$$

It is easily recognized in equation (2.6) that the oscillation amplitude is only dependent on the mixing angle with $\sin^2 2\theta$.

The PMNS-Matrix connects the flavor eigenstates with the mass eigenstates for a three-flavor oscillation:

$$\begin{pmatrix} |\nu_e\rangle \\ |\nu_\mu\rangle \\ |\nu_\tau\rangle \end{pmatrix} = U \begin{pmatrix} |\nu_1\rangle \\ |\nu_2\rangle \\ |\nu_3\rangle \end{pmatrix}, \tag{2.9}$$

where $|\nu_\alpha\rangle$ $(\alpha \in \{e, \mu, \tau\})$ are the flavor eigenstates, $|\nu_i\rangle$ $(i \in \{1, 2, 3\})$ are the mass eigenstates and U is a unitary 3×3 mixing matrix:

$$U = \begin{pmatrix} 1 & 0 & 0 \\ 0 & \cos\theta_{23} & \sin\theta_{23} \\ 0 & -\sin\theta_{23} & \cos\theta_{23} \end{pmatrix} \cdot \begin{pmatrix} \cos\theta_{13} & 0 & \sin\theta_{13} \cdot e^{-i\delta} \\ 0 & 1 & 0 \\ -\sin\theta_{13} \cdot e^{-i\delta} & 0 & \cos\theta_{13} \end{pmatrix} \cdot \begin{pmatrix} \cos\theta_{12} & \sin\theta_{12} & 0 \\ -\sin\theta_{12} & \cos\theta_{12} & 0 \\ 0 & 0 & 1 \end{pmatrix} \tag{2.10}$$

with the CP violating phase δ. This postulated oscillation is only possible when the neutrino is massive.

Experimental results of neutrino oscillation

For neutrinos generated by different sources, the mixing angles θ_{ij} and the two independent square neutrino mass differences Δm^2_{ij} can be determined by the observation of neutrino oscillation.

Due to the unkown sign of the relative mass splitting between Δm^2_{12} and Δm^2_{23}, there are two possible neutrino mass orderings. The normal ordering with $m_1 < m_2 \ll m_3$, and the inverted ordering $m_3 \ll m_1 < m_2$. A survey has shown that the normal ordering is preferred to the inverted ordering with a significance of 3.4σ [dFT$^+$18].

The observation of solar neutrinos makes use of the long propagation length of approximately 150×10^6 km. The mixing angle between first and second generation θ_{12} and Δm^2_{12} is determined by experiments like SNO. The values between the first and second generation are [Par18]:

$$\begin{aligned} \sin^2\theta_{12} &= 0.307^{+0.013}_{-0.012} \\ \Delta m^2_{12} &= (7.53 \pm 0.18) \times 10^{-5}\,\mathrm{eV}^2 \,. \end{aligned} \tag{2.11}$$

The parameters for the second and third generation are made by the observation of atmospheric neutrinos. Experiments like Super-Kamiokande measure neutrinos originating from pion-decays of cosmic rays:

$$\begin{aligned} \pi^+ \rightarrow & \mu^+ + \nu_\mu \\ & \hookrightarrow e^+ + \nu_e + \overline{\nu}_\mu \,. \end{aligned} \tag{2.12}$$

Therefore, the neutrino ratio produced in the upper atmosphere is $N_{\nu_\mu}/N_{\nu_e} = 2/1$. Due to the experimental capabilities of track and energy analysis, different propagation lengths can be used to determine the origin and neutrino energy. Neutrinos originating from above the detector only have to pass the atmosphere with an oscillation length of approximately 25 km, neutrinos from the detector downside have to travel through the earth with approximately 12 000 km. The different propagation lengths correspond with the oscillation probability of equation (2.6) [FHI$^+$98].

A two-detector setup is used at accelerator experiments. The flux of a near and far detector are measured and compared in order to determine the mass differences. Neutrinos are produced by firing a particle beam (e.g. protons) to a target. This creates pions with a decay channel like in equation (2.12). The advantage of this neutrino source is that the neutrino energy can be fine-tuned. This method allows the measurement of mass differences with high precision. The $\nu_\mu - \nu_\mu$ disappearance channel for the 23 parameters, and the $\nu_\mu - \nu_e$ appearance channel for the 13 parameters. The values are [Par18]:

$$\begin{aligned} \sin^2\theta_{23} &= 0.545 \pm 0.021 \text{ (normal mass odering)} \\ \sin^2\theta_{23} &= 0.547 \pm 0.021 \text{ (inverted mass odering)} \\ \Delta m^2_{23} &= (2.453 \pm 0.034) \times 10^{-3}\,\mathrm{eV}^2 \text{ (normal mass odering)} \\ \Delta m^2_{23} &= -2.546^{+0.034}_{-0.040} \times 10^{-3}\,\mathrm{eV}^2 \text{ (inverted mass odering)} \end{aligned} \tag{2.13}$$

The parameters for oscillation between the first and third generation are determined by reactor neutrino experiments like Double Chooz [AAA$^+$12], RENO [ACC$^+$12], and Daya Bay[ABB$^+$12]. A fission reactor is used to create an electron anti-neutrino flux. This flux is a byproduct of the reactor fuels β-decay. A far (approximately 1.4 km at RENO) and a near (approximately 400 m at RENO) detector use the inverse β-decay to measure the flux and compare it to the theoretical rate. Δm^2_{13} can be derived by Δm^2_{12} and Δm^2_{23}, $\sin^2\theta_{13}$ is [Par18]:

$$\sin^2\theta_{13} = (2.18 \pm 0.07) \times 10^{-2} \,. \tag{2.14}$$

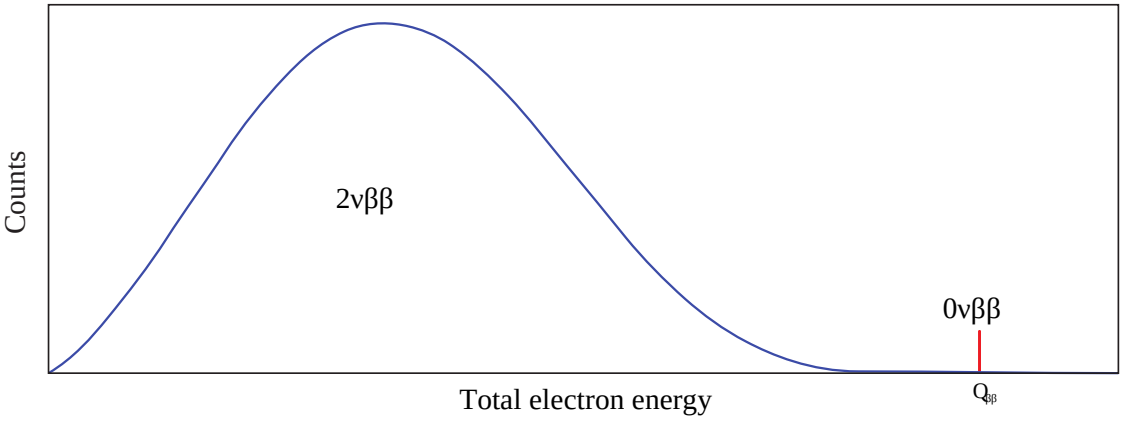

Figure 2.2.: Schematic energy spectrum of a $2\nu\beta\beta$- and $0\nu\beta\beta$-decay. The continuous spectrum of a $2\nu\beta\beta$-decay is shown on the left-hand side. If a $0\nu\beta\beta$ exists, the discrete line at the endpoint energy appears, which is shown with the red line on the right-hand side. The figure is taken and modified from [DMVV16].

2.4. Determination of the neutrino mass

Neutrino are massive, in opposition to the predictions of the standard model, as shown in section 2.3. The lower limit for the electron neutrino mass was determined by oscillation experiments to 0.01 eV. The upper limit is set by model-independent measurements to 1.1 eV [AAA$^+$19].

There are different approaches to determine the neutrino mass. One approach is the observation of a neutrinoless double β-decay ($0\nu\beta\beta$), this is based on the theory that neutrinos are Majorana particles (particle = anti particle). Whether neutrinos are Marjorana particles or not is still unknown.

Another approach is the observation of stellar objects like galaxy clusters. This method is highly dependent on theoretical models and therefore has a high uncertainty.

A model-independent approach is the observation of the β-decay energy spectrum. This method is only based on kinematic and energy-momentum conservation. Hence, a completely model-independent measurement is possible.

2.4.1. Neutrinoless double β-decay

The neutrinoless double β-decay can be used, if it exists, to determine the neutrino mass by the experimental determination of half life $T_{1/2}$ for the element under investigation.

The existence of the $0\nu\beta\beta$-decay requires neutrinos to be Majorana particles. This means that the neutrino is its own anti-particle ($\nu = \overline{\nu}$). In this case, the lepton number conversation is violated, and therefore forbidden in the standard model. That observation would indicate physics beyond the standard model.

The binding energy of nucleons in a nucleus is described by the Bethe-Weizsäcker-Equation [vW35] and can be represented as parabola for isobaric isotopes. For an even nucleus number the mass-parabola is split into an even-even (lower mass) and an odd-odd (higher mass) parabola due to the spin coupling between the constituents.

$$m(Z, A = \text{constant}) \;\propto\; \text{constant} + \alpha Z + \beta Z^2 + \delta p \;, \tag{2.15}$$

with δp as empirical pairing energy, A nucleon and Z proton number of the nucleus, α the factor accounting for the coulomb force, and β accounting for the increasing total energy

caused by the Pauli exclusion principle. The pairing term is:

$$\delta p = \begin{cases} -apA^{-\frac{1}{2}} \text{ for even-even nuclei} \\ 0 \\ +apA^{-\frac{1}{2}} \text{ for odd-odd nuclei} \end{cases} \tag{2.16}$$

with $ap \approx 12\,\text{MeV}$. This split can lead to a forbidden single β-decay of even-even nucleus if the neighbor odd-odd nucleus has higher binding energy. In this case, the odd-odd nucleus undergoes a double β-decay to a lower even-even nucleus [Zub11].

The double β-decay was first discussed by Goeppert-Mayer in 1935 as a two-neutrino-double β-decay ($2\nu\beta\beta$) [Goe35]. This decay is a higher-order effect and therefore the half-life is in the order of 10^{20} a [Par18], which is a few orders of magnitudes larger than the single β decay. The $0\nu\beta\beta$-decay based on the Majorana theory was discussed for the first time by Furry in 1939 [Fur39] in the form of:

$$(Z, A) \rightarrow (Z \pm 2, A) + \begin{cases} 2e^- \ (0\nu\beta^-\beta^-) \\ 2e^+ \ (0\nu\beta^+\beta^+) \end{cases} \quad . \tag{2.17}$$

An additional discrete line would appear in the energy spectrum at the endpoint energy for a two-body process (figure 2.2).

The effective mass of the Majorana neutrino can be calculated by the observation of the half-life time for the double β-decay. In case of a light massive Majorana neutrino, it yields:

$$\langle m_{\beta\beta} \rangle^2 = \left(T_{1/2}^{0\nu\beta\beta} \cdot G^{0\nu\beta\beta}(E_0, Z) \cdot \left| M_{GT}^{0\nu\beta\beta} - \frac{g_V^2}{g_A^2} M_F^{0\nu\beta\beta} \right|^2 \right)^{-1} , \tag{2.18}$$

where $T_{1/2}^{0\nu\beta\beta}$ is the experimental observable, $G^{0\nu\beta\beta}(E_0, Z)$ the phase-space integral, M_{GT} and M_F the Gamov-Teller Matrix elements and g_V, g_A the (axial-) vector coupling constant of the electroweak interaction. $\langle m_{\beta\beta} \rangle$ is the coherent sum of the neutrino eigenstates ν_1, ν_2, ν_3

$$\langle m_{\beta\beta} \rangle = \left| \sum_{i=1}^{3} |U_{e,i}|^2 \, m_i \cdot e^{i\alpha_i} \right|^2 , \tag{2.19}$$

where $e^{i\alpha_i}$ is the CP violating Majorana phase.

Untill today, none of the experiments, like NEMO-3 and EXO-200, have had a positive result. The lower limit for $T_{1/2}^{0\nu\beta\beta}$ is derived by investigating different $2\nu\beta\beta$ isotopes as sources. It is in the order of 10^{23} a, coresponding to an upper limit for $m_{\beta\beta} < 0.061\,\text{eV}$ to 22 eV [Par18].

2.4.2. Cosmic neutrinos

The observation of cosmological phenomenons is another way to determine the neutrino mass indirectly. These phenomenons are the density fluctuation in the universe hence forming of galaxies in the early universe, and the cosmic microwave background (CMB). The energy density parameter is $\Omega = 1$ for an euclidean universe, where Ω is the sum of all its constituents (matter, radiation, and vacuum). With the Friedmann-Lemaître-equation

$$H^2 \frac{8\pi G}{3} \rho = H_0^2 \frac{\rho}{\rho_c^0} , \tag{2.20}$$

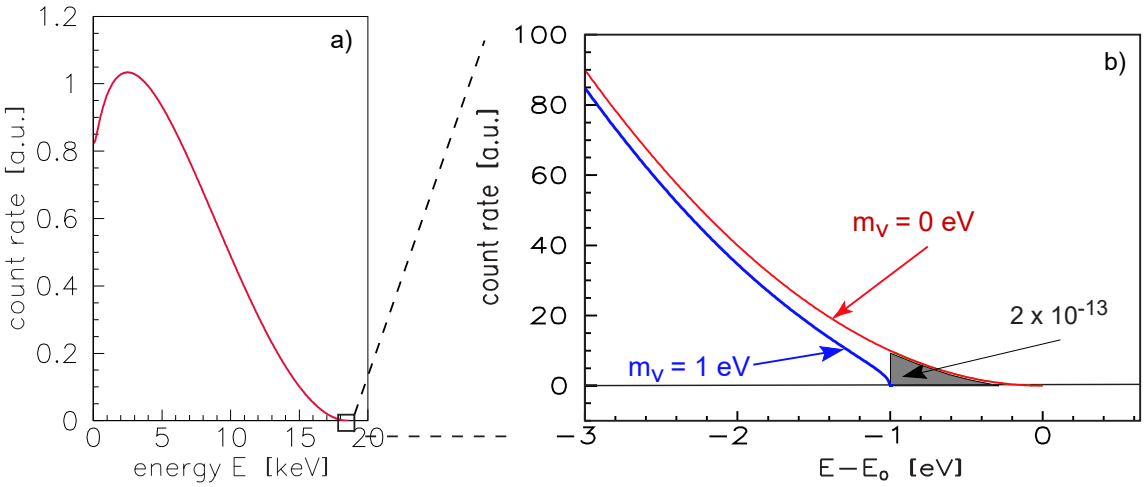

Figure 2.3.: Energy spectrum of a tritium β decay. a) Complete spectrum b) Enlarged endpoint region of the spectrum with a neutrino mass $m_\nu = 0\,\text{eV}$ red line, and $m_\nu = 1\,\text{eV}$ blue line. The figure is taken from [AAB05].

where G is the gravitational constant, ρ the mass, ρ_c the critical mass density, and H the hubble parameter while the index 0 means the day of observation with t_0 the age of the universe. Historically, it is defined by:

$$h = \frac{H_0}{100\,\text{km}\,\text{Mpc}^{-1}\,\text{s}^{-1}} \,. \tag{2.21}$$

The energy density parameter for the neutrino is:

$$\Omega_\nu = \frac{\rho_\nu}{\rho_c^0} = \frac{\sum_i m_i}{93.14 \cdot h^2\,\text{eV}} \,. \tag{2.22}$$

$\sum_i m_i$ is the sum of all neutrino species. The neutrino density, with respect to the matter density, is:

$$\frac{\Omega_\nu}{\Omega_m} = \frac{\rho_\nu}{\rho_{CDM} + \rho_b + \rho_\nu} \,. \tag{2.23}$$

ρ_{CDM} is the energy density of the cold dark matter and ρ_b for barionic matter. [LP14]

The upper limit for the neutrino mass is with consideration of all the cosmological parameters [Pla14]:

$$m_\nu < 0.23\,\text{eV} \,. \tag{2.24}$$

2.4.3. Kinematics of β decay

The investigation of the β-decay spectrum is based on the kinematic of a three-body decay and the energy released during the process. It is described as:

$$\text{M}(A, Z) \rightarrow \text{D}(A, Z+1) + e^- + \overline{\nu}_e \,, \tag{2.25}$$

$\text{M}(A, Z)$ is the mother and $\text{D}(A, Z+1)$ the daughter nucleus. For a nucleus at rest, the electron energy E_e should be according to the energy conservation:

$$m_e \leq E_e \leq m_M - m_D - T_D - E_\nu \,. \tag{2.26}$$

T_D is the recoil energy of the nucleus, E_ν the neutrino energy, m_M the mass of the mother and m_D of the daughter nucleus. The released energy during the decay is given by the Q-value:

$$Q = \Delta m \ , \tag{2.27}$$

where $\Delta m = m(Z, A) - m(Z + 1, A)$ [Zub11]. With equation (2.26) the endpoint energy is:

$$E_0 = Q - T_D \ . \tag{2.28}$$

The β-decay with neutrino is a three-body decay. Hence, the energy spectrum is a continuum as shown in figure 2.3. The determination of this spectrum can be accomplished in different ways. For example, the synchrotron radiation of the β-electrons is measured from tritium in a homogeneous magnetic field in Project 8, and the endpoint region of the spectrum is observed [Kof15].

3. The KATRIN experiment

This chapter gives an overview of the objectives and methods of the KATRIN experiment, which aims to investigate the endpoint region of the β-decay spectrum for tritium and determine the effective mass of the electron neutrino via high-precision spectroscopy.

3.1. Physics of KATRIN

This section discusses the objectives of KATRIN and presents the physical principle of the MAC-E filter, which plays the key role in achieving the aimed energy resolution.

3.1.1. Objectives

The KArlsruhe TRitium Neutrino experiment is located at the KIT in Karlsruhe. It aims to measure the electron neutrino mass by observing the end point energy of the β-decay spectrum from molecular tritium with a sensitivity of

$$m_{\nu_e} \leq 0.2\,\text{eV}\ (90\,\%\ \text{CL})\ . \tag{3.1}$$

This will be an improvement in sensitivity, compared to previous experiments, by one order of magnitude [AAB05]. It is possible to investigate the sub-eV neutrino mass scale with this high sensitivity. This is of high interest in particle physics, astrophysics, and cosmology. The investigation of the β-decay spectrum is only based on kinematic relations and energy-momentum conversation. Hence, it is a completely model-independent measurement of the neutrino mass.

KATRIN uses a large spectrometer with a usable diameter of 9 m applying the Magnetic Adiabatic Collimation with Electrostatic filter (MAC-E filter) technique [AAB05]. The tritium decay takes place in the WGTS. The resulting β-electrons are guided by magnetic fields through the spectrometer. They have to pass the differential pumping section, the cryogenic pumping section, the pre-spectrometer between WGTS and spectrometer, and hit the detector if they overcome the main spectrometer potential.[Sch16]

3.1.2. MAC-E filter

A high luminosity and energy resolution is required in order to achieve the targeted sensitivity in the observation of the endpoint region of the β-decay spectrum. The MAC-E filter combines these two requirements and enables the high energy resolution of 0.93 eV [AAB05].

The main part of the MAC-E-Filter is a magnetic field covering the main spectrometer tank. The field guides β-electrons on a cyclotron motion around the field lines. The field strength drops many orders of magnitude towards the spectrometer center. Due to this gradient, most of the cyclotron energy is transformed into longitudinal motion. If the

magnetic fields change slowly, the momentum is transformed adiabatically and therefore the magnetic moment μ keeps constant in first order.

$$\mu = \frac{E_\perp}{B} = \text{const.} \tag{3.2}$$

These electrons, parallel to the field lines, run against the electrostatic potential U in the spectrometer center. A cylindrical electrode forms the potential which filters the lower energetic electrons. The electrons with a sufficiently high energy get re-accelerated to the detector where they are counted.

The minimum magnetic field B_A in the spectrometer center and the maximum B_max at one end define the relative sharpness $\Delta E/E$ of this filter:

$$\frac{\Delta E}{E} = \frac{B_\mathrm{A}}{B_\mathrm{max}} \,. \tag{3.3}$$

The magnetic mirror effect is used to suppress electrons with a high scattering probability. Therefore, the β-electron source is placed in a magnetic field $B_\mathrm{S} < B_\mathrm{max}$. This effect restricts the accepted maximum starting angle of the electron to:

$$\sin\theta_\mathrm{max} = \sqrt{\frac{B_\mathrm{S}}{B_\mathrm{max}}} \,. \tag{3.4}$$

With equations (3.2), (3.3) and (3.4) the transmission function T with retarding potential U and electron charge q is given by:

$$T(E, qU) = \begin{cases} 0 & E - qU < 0 \\ \dfrac{1 - \sqrt{1 - \dfrac{E - qU}{E}\dfrac{B_\mathrm{S}}{B_\mathrm{A}}}}{1 - \sqrt{1 - \dfrac{\Delta E}{E}\dfrac{B_\mathrm{S}}{B_\mathrm{A}}}} & 0 \leq E - qU \leq \Delta E \\ 1 & E - qU > \Delta E \end{cases} \tag{3.5}$$

For $T = 0$ the electron with energy E is reflected while for $T = 1$ the electron is transmitted. [AAB05]

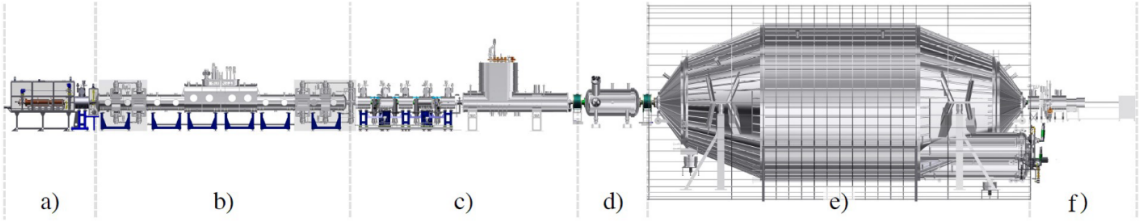

Figure 3.1.: Overview of the experimental setup of the KATRIN. a) Rear section, b) windowless gaseous tritium source (WGTS), c) pumping section: DPS, CPS, cryostats and MAC-E-filters, d) pre-spectrometer, e) main spectrometer with aircoil system. Figure is taken from [AAA+19].

3.2. Source and transport section

In order to achieve the desired precision in the β-decay endpoint measurements, big efforts have been made to assure a stable and controlled tritium source. This chapter explains the main parts of this system.

3.2.1. Rear section

The rear section is part of the Calibration and Monitoring System (CMS) of the tritium related components. It monitors the source activity by β-induced X-ray spectrometry and the electron gun. Additionally, the rear section houses the golden rear wall, which defines the source potential. [Sch16]

3.2.2. Windowless gaseous tritium source

The Windowless Gaseous Tritium Source (WGTS) is the β-electron source for KATRIN. Windowless describes that there is no physical barrier for the gas. The molecular tritium with a temperature of 27 K and a pressure of $p = 3.4 \times 10^{-3}$ mbar is injected through a capillary at the middle of the WGTS tube with a diameter of 90 mm and a length of 10 m [AAB05]. The tritium then diffuses to both ends of the tube, where the gas is pumped into the circulation loop.

The density profile is influenced by the tube conductance. In order to achieve a source stability of 0.1 %, the source temperature is regulated by a two-phase neon cooling system at 30 K with a stability and homogeneity of 0.1 % [GBH$^+$13]. The nomnial colum density is $pd = 5 \times 10^{17}\,\mathrm{cm}^{-1}$ [Hö12], the stability is provided by a pressure-controlled buffer vessel.

With a transport time in the order of 1 s, the decay rate is in the order of $10^{11}\,\mathrm{s}^{-1}$. The electrons produced by the β-decay are guided to both ends of the WGTS by a magnetic field of 3.6 T. [AAB05]

3.2.3. LOOP system

The LOOP system, shown in figure 3.2, is installed in order to stabilize the tritium injection rate at the WGTS with a stability of better than 0.1 % [PSB15]. It controls the injection rate, monitors the purity of the injected tritium, and filters all non-hydrogen molecules from the gas. A high isotopic purity of larger than 95 % and a throughput of approximately $40\,\mathrm{g\,d}^{-1}$ can be provided [AAB05]. The system consists of 3 subsystems.

The **circulation loop** supplies the WGTS with tritium. The gas gets pumped and recycled at both ends of the WGTS. The pumped gas is fed through a palladium filter. This filter uses a silver-palladium membrane to extract all non-hydrogen species. These impurities occur by radio-chemical reactions or decay from tritium. Additionally, approximately 1.4 sccm gas is constantly extracted from the permeator. The purified gas gets transferred to a buffer vessel (BV04). From the buffer vessel, the tritium is fed through a Laser-Raman sampling cell into the pressure- and temperature- (operated at 318 K with a stability better than 0.5 K) controlled injection vessel (BV05). The Laser-Raman cell measures the composition of the gas inline using the Raman-effect. Due to the inelastic scattering of light on molecules, each molecule has characteristic lines in the analyzed spectrum. The installed system can detect all hydrogen isotopes at a level of 0.1 % within 100 s. [PSB15, Pri13]

The palladium filter (permeator) is connected to the **exhaust loop**. The filtered gas is stored in the waste buffer (BV03), where the waste gas gets transferred to the TLK's (Tritium Laboratory Karlsruhe) exhaust processing system [PSB15].

The **feed loop** replaces the filtered amount of gas. It is connected to the TLK infrastructure and provides the circulation loop with high purity tritium via buffer vessel BV01 [PSB15].

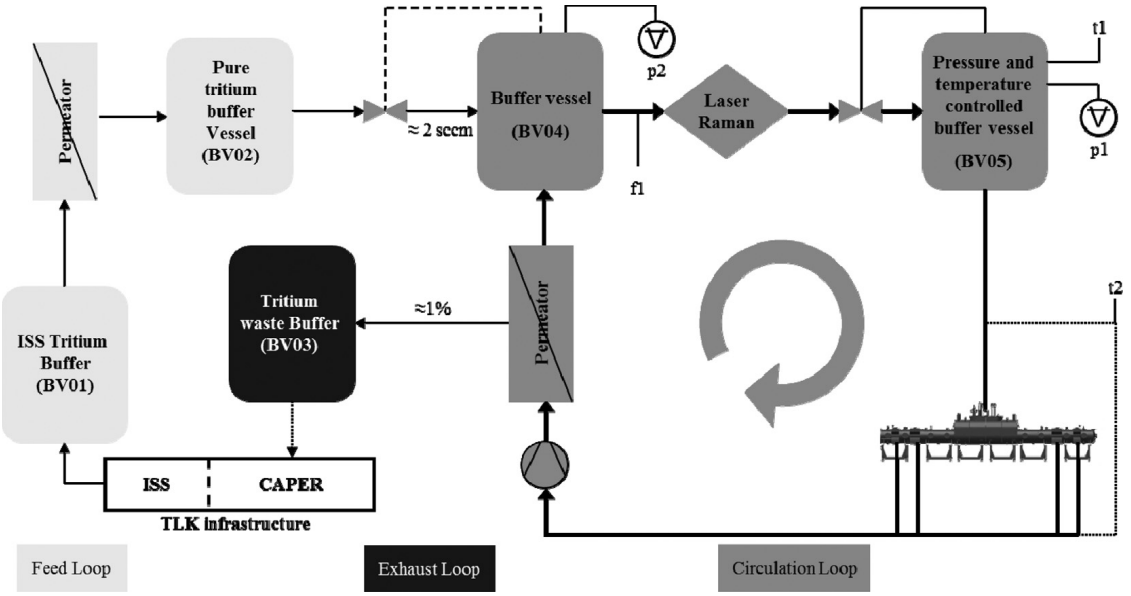

Figure 3.2.: Simplified scheme of the KATRIN tritium loop system at the WGTS. The Circulation Loop with essential components is shown for pressure stabilized injection, tritium cleaning (Permeator) and monitoring (Laser Raman). The Feed Loop provides pure tritium, and the Exhaust Loop transfers waste gas to the TLK infrastructure. Figure is extracted from [PSB15].

3.2.4. Transport system

In order to achieve the requirements for a low background rate in the order of 10 mcps [Har15] in the main spectrometer, the neutral tritium flow has to be reduced to at least $10^{-14}\,\mathrm{mbar}\,\ell\,\mathrm{s}^{-1}$ [AAB05]. Therefore, the transport system (DPS and CPS) is installed between the WGTS and the pre-spectrometer.

The **differential pumping section** (DPS) is located next to the WGTS. To prevent a straight trajectory for the tritium molecules, five 1 m-long beam tubes equipped with superconducting solenoids are arranged in 20° angle. The signal electrons are guided by the 5.6 T magnetic field of the superconducting solenoids through the cryogenic pumping section (CPS). Four turbo molecular pumps (TMP) are installed alongside the solenoids. Each TMP has a pumping speed of higher than $2000\,\ell\,\mathrm{s}^{-1}$ for H_2. The designed overall reduction factor of the DPS together with the pumps of the WGTS is larger than 10^7 [AAB05]. Ions caused by β-decay in the source are unaffected by the DPS. In order to remove these ions, three dipol electrodes, which cause a drift towards the DPS walls, and a ring-shaped blocking electrode are installed [Win11, Kle19].

The **cryogenic pumping section** (CPS) is located next to the DPS. Its working principle is to trap tritium that impinges on the 3 K surface of the tube. Alongside the transport tube, transport magnets are installed, which guide the signal electron with the transport field of 5.6 T through the section. Each section is tilted to each other by 15°. In order to enlarge the effective surface area, an argon-frost layer is prepared on the inner surface of the beam tube. The CPS will be regenerated after 60 days to remove tritium on the surface. Overall, the CPS reduces the tritium flow by more than 7 magnitudes additionally [Rö19].

3.3. Spectrometer and detector section

The KATRIN experiment uses two spectrometers and the focal plane detector in order to filter electrons below the threshold level and detect signal electrons.

3.3.1. Pre-spectrometer

The pre-spectrometer is installed between the transport section and the main spectrometer. It has a length of 3.88 m and an inner diameter of 1.68 m. A MAC-E-Filter is applied to pre-filter and reduce the $10^{10}\,s^{-1}$ electron flux to $10^{4}\,s^{-1}$. The pre-filter requires an energy resolution of $\Delta E \approx 100\,eV$ [AAB05]. The retreating energy is fixed to 10.4 kV [AAA$^+$19], in order to reject the electrons that have no information about the neutrino mass.

3.3.2. Main spectrometer

The main spectrometer with its high resolution MAC-E-Filter is the key component of the KATRIN experiment. It has a length of 23.3 m and a diameter of 10 m. Two superconducting solenoids generate the inhomogeneous magnetic field for the MAC-E-Filter. The diameter of the analyzing plane is 9 m. Additional air coils are installed to fine-tune the magnetic field and compensate the earths magnetic field. The spectrometer tank hull serves as a guard electrode for the high voltage on the inner wire electrodes and is therefore at a high potential. An electrode wire system is used to fine-tune the electric potential inside the tank. The transmitted electrons are re-accelerated to their initial energy and guided to the focal plane detector. To reduce the outgassing rate of hydrogen from the stainless steel and fit the requirements of the ultra high vacuum of 10^{-11} mbar inside the tank, the main spectrometer must be backed out at 200 °C. [AAB05]

3.3.3. Focal plane detector

The focal plane detector (FPD) is installed at the end of the setup. The β-decay electrons are detected by a monolithic 148 pixel p-i-n (positive-intrinsic-negative doted silicon) diode array. The sensitive area of the detector has a diameter of 90 mm, surrounded by a 2 mm guard and a 15.5 mm bias ring. The FDPs radial geometry allows corrections for electrical and magnetic inhomogeneities in the analyzing plane. The post-acceleration electrode (PAE), located before the diode, shifts the electron energy to a range with a lower background. This leads to an energy resolution of $\Delta E \approx 1.6\,keV$ [Hub20] (Full Width at Half Maximum FWHM) at the 18.6 keV endpoint energy of the spectrum. [ABB$^+$15]

3.4. First tritium measurement and challenges

The tritium measurements executed in spring 2019 improved the upper limit for the neutrino mass to 1.1 eV (90 % confidence level) [AAA$^+$19]. During this measurement, it was observed that the injection flow decreased over time (see figure 3.3), because methane freezed out on the injection capillary of the WGTS. The impurity in the tritium gas was caused by radio-chemical reactions. Hence, a cold trap was planned to remove the methane before it can reach the part of the injection capillary inside the WGTS cryostat.

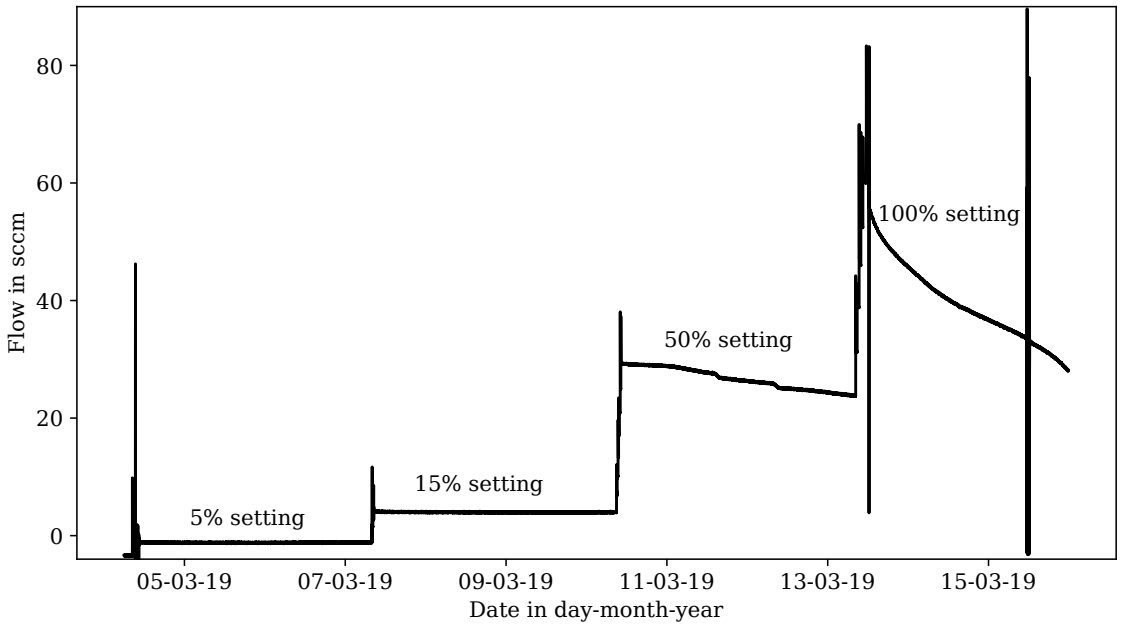

Figure 3.3.: Decrease in tritium flow. Injection flow to the WGTS shows decrease over time at higher injection rates (50 %, and 100 % setting) as a result of methane freezing out at the injection capillary.

4. Theory of cryopumping and fluid dynamics

In order to understand the basic physics applied in this thesis, this chapter explains the fundamental theories of cryopumping and fluid dynamics.

4.1. Sorption phenomenons

Cryogenic baffles do not only work by entrapment through condensation but also have characteristics of sorption pumps.

Gas molecules or atoms hitting the surface have a sticking probability $s \leq 1$ and a probability of being reflected of $s - 1$. The adsorbate can be an atom or a molecule sticking on the surface. The adsorption energy E_{ads} is the energy of the adsorption process caused by physisorption (dipole or Van-der-Waals forces) or chemisorption (electron exchange forces). The desorption is the reverse process to adsorption, in which a stored atom or molecule degas. Desorption energy E_{des} is the energy needed to desorb the particles. It is equal to the adsorption energy $E_{\text{des}} = E_{\text{ads}}$ if the activation energy for absorption is 0. [Jou04]

4.1.1. Sorption

If the surface of the sorbent material is covered with more than one layer of particles to adsorb, the desorption energy E_{des} of the layers $n \neq 1$ is similar to the enthalpy of vaporization Δh. With the Langmuir assumption that a particle only can be adsorped if it hits a non-covered surface area (layer $n = 1$), it follows:

$$f(\theta) = 1 - \theta \; . \tag{4.1}$$

The corresponding adsorption rate for an in first order not temperature dependent sticking probability s_0 is:

$$j_{\text{ads}} = s_0 \cdot (1 - \theta) \cdot \frac{n \cdot c}{4} \; , \tag{4.2}$$

c is the mean velocity of the medium, θ the degree of covered surface area. [Jou04]

4.1.2. Desorption

Desorption is the reverse process of sorption. A particle with a kinetic energy $E_{\text{kin}} \geq E_{\text{des}}$ can be desorbed. According to Boltzmann, $\Delta\tilde{n}$ out of $\tilde{n}$ particles fulfill the necessary energy requirement:

$$\Delta\tilde{n} = \tilde{n} \cdot \exp\left(-\frac{E_{\text{des}}}{R \cdot T}\right) \; . \tag{4.3}$$

T is the surface temperature, R the ideal gas constant. The desorption rate is given with the surface frequency of the stored particles in the order of $\nu_0 \approx 10^{13}\,\mathrm{s}^{-1}$:

$$j_{\mathrm{des}} = \frac{\mathrm{d}\tilde{n}}{\mathrm{d}t} = -\nu_0 \cdot \tilde{n} \cdot \exp\left(-\frac{E_{\mathrm{des}}}{R \cdot T}\right) . \tag{4.4}$$

And the mean sojourn time τ:

$$\tau = \frac{1}{\nu_0} \exp\left(\frac{E_{\mathrm{des}}}{R \cdot T}\right) , \tag{4.5}$$

where $E_{\mathrm{des}} = -\Delta H_{\mathrm{ads}}$, and H_{ads} is the adsorption enthalpy. [Jou04]

4.2. Physics of cryopumping

Cryopumping describes the entrapment through condensation of the residual gases on the inner surface of the pump at temperatures below 120 K. The equilibrium vapor pressure has to be equal or less than the pressure in the chamber [fS81].

4.2.1. Cryocondensation

Cryocondensation makes use of the different saturation pressure curves of molecular gases. A cold surface captures the targeted gas molecules and therefore pumps them. The pressure in a cryopumping system is usually below the triple point, where the temperature and pressure of all three phases are in equilibrium. In this case, gas undergoes a direct phase change from gaseous to solid. Hence, the saturation and the sublimation pressure curves are identical. [Day07]

Figure 4.1 shows the saturation pressure curves of different gases. For example, the saturation temperature of tritium is one magnitude lower than the one of methane. Methane can be separated in this case by adjusting the surface temperature of the cryogenic pump higher than tritium but lower than the methane saturation temperature at the desired pressure level.

The saturation pressure curves in figure 4.1 are plotted for thermodynamic equilibrium at the phase boundary of the corresponding gas. This results in a zero particle flux which unavoidably leads to a zero pumping speed. A factor 100 larger pressure than the saturation is recommended to accomplish a sufficient pumping speed [Day07].

4.2.2. Thermal stability

One aspect of the cold trap design is thermal stability. Small variations in temperature can change the species of pumped gas as shown in figure 4.1. For example, the saturation pressure curves of D_2 and T_2 differ by less than 1 K.

The housing of a cryopump is usually at ambient temperature of approximately 300 K, while the cryopanel is refrigerated. For steady temperature conditions, the heat flux towards the panel $\dot{Q}$ must be equal to the cooler refrigeration power. The thermal conductivity of the solids $\dot{Q}_S$, gas heat conduction $\dot{Q}_G$, thermal radiation $\dot{Q}_R$, phase transition temperature $\Delta\dot{H}_{PT}$, and the phase change enthalpy $\Delta\dot{H}_{PC}$ generate the heat flux [Day07]:

$$\dot{Q} = \dot{Q}_S + \dot{Q}_G + \dot{Q}_R + \Delta\dot{H}_{PT} + \Delta\dot{H}_{PC} . \tag{4.6}$$

$\dot{Q}_S$ is proportional to:

$$\dot{Q}_S \sim \frac{\lambda}{L} \cdot A , \tag{4.7}$$

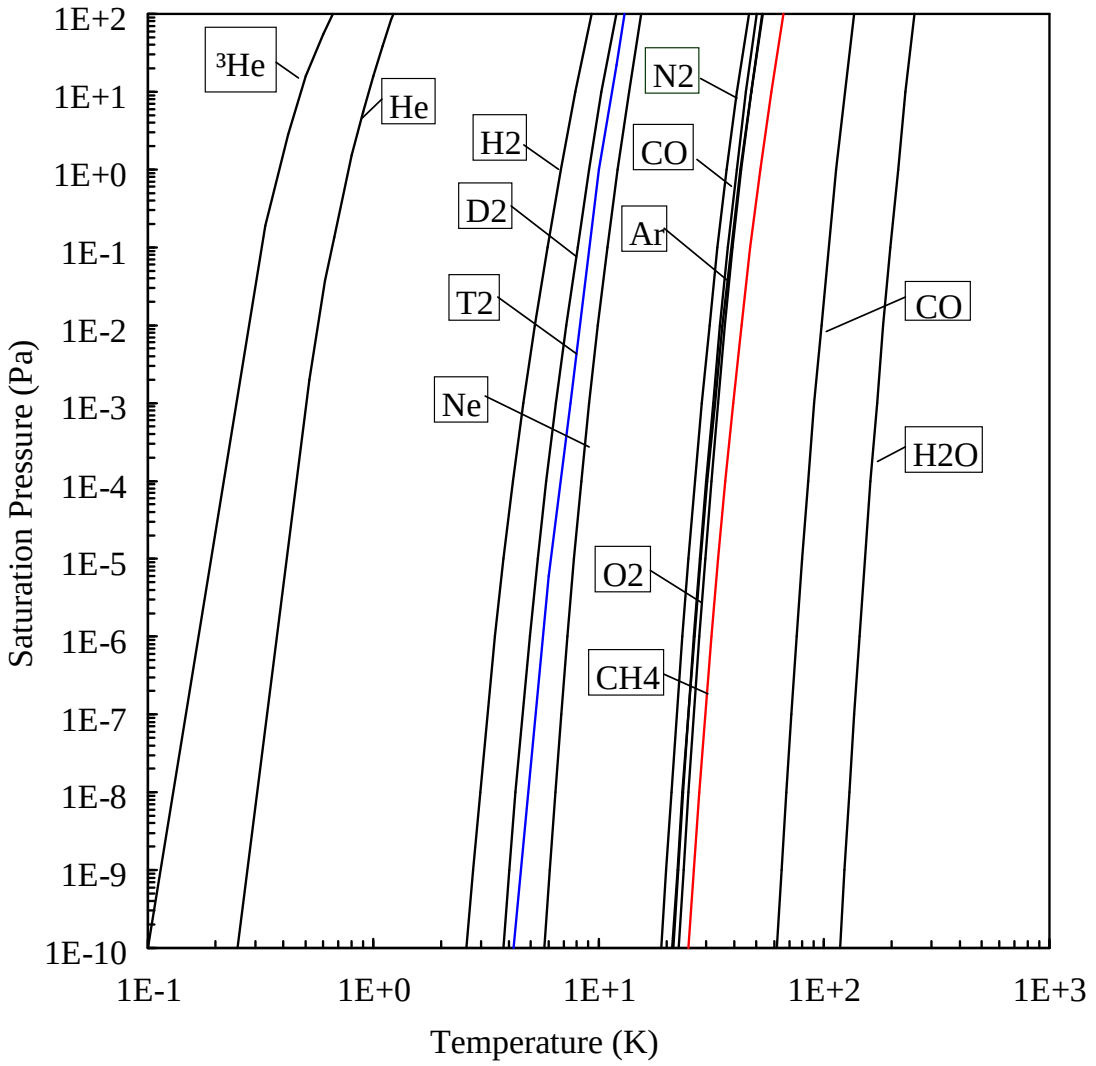

Figure 4.1.: Saturation pressure curves. The saturation pressure curves for different gases including CH_4 (red line) and T_2 (blue line) are displayed. Figure modified from [Day07].

λ is the thermal conductivity, A the cross section, and L the conductor length.

The gas heat conduction $\dot{Q}_G$ is the quantity of energy transfer, caused by the collision of the gas molecules and the surface of the pump. This effect correlates with the mean free path Λ and the vessel dimension ℓ. The heat transfer depends only on the number of molecules for $\Lambda > \ell$. The Knudsen number Kn characterizes the different flow regimes, like laminar and continuum flow etc.:

$$Kn = \frac{\Lambda}{\ell} \, . \tag{4.8}$$

The usual operational state of cryopumps is given by $Kn \gg 1$. The system is in a molecular flow and gas heat conduction can be neglected while the radiation heat transfer $\dot{Q}_R$ is dominant in this environment. The radiation heat exchange for two surfaces A_1 and A_2 with emissivity ε_1 and ε_2 is:

$$\dot{Q}_{12} = C_{12} \cdot A_1 \cdot \left(T_1^4 - T_2^4 \right) \, , \tag{4.9}$$

with the exchange number:

$$C_{12} = \frac{\sigma \cdot \varepsilon_1 \cdot \varepsilon_2}{1 - (1 - \varepsilon_1) \cdot (1 - \varepsilon_2) \cdot \varphi_{21}} \,, \tag{4.10}$$

with the Stefan-Bolzmann constant σ. φ_{21} is the geometric shape factor defined by the fraction of heat radiating from surface 1 and absorbed by surface 2. [Day07]

As shown in equation (4.9), a big temperature difference of the cryopump housing at ambient temperature and cryopump leads to a high $\dot{Q}_R$. Therefore, a shielding between housing and pump can be necessary. The shielding is used as a second cryopanel, which operates at higher temperatures than the pump, but lower than the outer housing. It blocks the direct path from the housing to the pump of photons and residual gas molecules in an isolation vacuum to reduce the temperature difference. A low emissivity $\varepsilon \ll 1$ of the cryopump surface, where 1 is equal to a black body, is preferred.

4.2.3. Pumping characteristics of cryo pumps

The pumping characteristics of a cryo pump are quantified by the following parameters [Day07]:

- The **pumping speed** S is the quotient of throughput Q and working pressure p as long as p is smaller than the ultimate pressure of the pump:

$$S = \frac{Q}{p} \,. \tag{4.11}$$

- The **capture coefficient** c is the ratio of actual pumping speed S to the ideal pumping speed S_{id}. Hence,

$$S = c \cdot S_{\mathrm{id}} = c \cdot A_{\mathrm{inlet}} \cdot \sqrt{\frac{R \cdot T}{2\pi \cdot M}} \,. \tag{4.12}$$

  A_{inlet} is the area of cryo surface, M molecular weight of pumped gas, R ideal gas constant, and T the gas temperature. An approximation of c is:

$$\frac{1}{c} = \frac{1}{\alpha} + \frac{1}{w} - 1 \,. \tag{4.13}$$

  α is the sticking probability of the particles impinging on the cryo surface, w the transmission probability defined by the installed baffles and other geometric factors that reduce the speed of particles. The sticking probability mainly depends on gas type, temperature, and pumping phenomenon of the baffle material.

- The **maximum throughput** is defined as the maximum gas flow rate that can be pumped at a cryo surface temperature below 20 K and a gas temperature of 273.15 K.
- The **pumping capacity** is defined as the quantity of pumped gas until S is reduced to 50 % of the initial pumping speed. This decrease of pumping speed can be caused by a rising temperature gradient at the cryo panels, due to the coverage of frozen gas. The pump must undergo a regeneration procedure when the pumping capacity is reached.
- **Ultimate pressure** is the lowest base pressure the pump can reach after appropriate preparations, such as baking out. It has to be operated at the minimum operating temperature for at least 24 h.
- **Crossover** is defined as the minimum amount of nitrogen gas that can be fed into the pump in $\Delta t = 3\,\mathrm{s}$, while the cryo panel temperature retains at below 20 K.cryo panel

4.2.4. Regeneration

In order to restore the initial pumping speed when the capacity of a cryopump is reached, a regeneration process is necessary. This is done by heating the cryo surface of the pump while pumping the released gas. The pumped gas gets released at equilibrium temperature of phase transition or desorption. The pump must be isolated from the main vacuum system, in order to not contaminate it, before the pump is heated and until it is cooled down to pumping temperature after regeneration. A quasi-continuous pumping system, which can regenerate itself, can be achieved by combining several cryogenic pumps that are operated in staggered intervals. [Day07]

4.3. Basics of fluid dynamics

The conductance in fluid dynamics is defined analog to Ohm's law, where the gas flow ϕ is similar to current I, the pressure difference Δp is similar to the electrical potential U and the conductance C is the inverse of the electrical resistance R:

$$C = \frac{\phi}{\Delta p} \,. \tag{4.14}$$

For a system of i connected parts, the overall conductance is calculated in a serial configuration by:

$$\frac{1}{C} = \sum_i \frac{1}{C_i} \,. \tag{4.15}$$

In a parallel configuration, it yields:

$$C = \sum_i C_i \,. \tag{4.16}$$

The conductance can be determined by analytical methods in molecular flow conditions. An aperture connecting two volumes under molecular flow ϕ is defined by the mean thermal velocity $\overline{c}$ of the particles, the pressure difference of the two volumes Δp, and the cross section area of the aperture A:

$$\phi = A \cdot \frac{\overline{c}}{4} \cdot \Delta p \,. \tag{4.17}$$

With equation (4.14) and the mean thermal velocity, defined as weighted mean speed of the gas particles is:

$$\overline{c} = \sqrt{\frac{8 \cdot k_B \cdot T}{\pi \cdot m}} \,, \tag{4.18}$$

where m is the molecular weight. Hence, the conductance can be written as:

$$C_{\text{aperture}} = A \cdot \sqrt{\frac{k_B \cdot T}{2\pi \cdot m}} \,. \tag{4.19}$$

The conductance of a long pipe is the product of the aperture conductance and the pipe probability of passage of the pipe for the gas particles P. The probability can be derived from Monte Carlo simulations. For a long pipe with diameter d and length ℓ, it is calculated by:

$$P_{\text{pipe}} = \frac{4}{3} \cdot \frac{d}{\ell} \,. \tag{4.20}$$

Hence, the conductance for a pipe is given by:

$$\begin{aligned} C_{\text{pipe}} &= C_{\text{aperture}} \cdot P_{\text{pipe}} \\ &= \frac{\overline{c} \cdot \pi \cdot d^3}{12 \cdot \ell} \\ &= \sqrt{\frac{k_B \cdot T \cdot \pi}{18 \cdot m}} \cdot \frac{d^3}{\ell} \ . \end{aligned} \tag{4.21}$$

As shown, the conductance is dependent on gas species and temperature in addition to the geometry of the installation. [Jou04]

The viscosity must be taken into account at laminar-flow conditions, which leads, in case of a pipe, to:

$$C = \frac{\pi \cdot d^4 \cdot \overline{p}}{128 \cdot \eta \cdot \ell} \ , \tag{4.22}$$

where η is the viscosity, $\overline{p}$ the mean pressure, ℓ the length, and d the diameter of the pipe [Gmb13].

The conductance of a thin aperture is well known under different flow conditions and can be adjusted according to the corresponding Knudsen number [JKS98].

5. Experimental setup for cold trap measurements

5.1. Cold trap

In the presence of stainless steel walls, tritium can produce different species of methane CX_4 ($X \in \{H, D, T\}$) by radio-chemical reactions [Gil80]. Since the WGTS and the LOOP system are primarily made of stainless steel, methane can occur in the gas mixture fed into the WGTS tube. One of the key parameters for a time- and space-homogeneous gas column is the temperature of the main tube. Therefore, the temperature is regulated at about 30 K [Pri13]. The feed in is directly attached to the outer side of the main tube which leads to a thermal equilibrium. Due to this low temperature, residual methane freezes on the walls of the feed in, as described in section 4.2.1. This reduces the effective diameter so that the gas flow drops significantly over a short period of time during the first full tritium measurements.

Equation (4.22) shows the conductance is very sensitive to changes in diameter. A small decrease can change the gas flow significantly. The goal of the designed cold trap, which is introduced and tested in the scope of this thesis, is to freeze the methane before it enters the feed in.

5.1.1. Cold trap cryo panels

The inner geometry of the installed cold trap is shown in figure 5.1. The gas mixture is fed into the trap (lower right-hand side) and has to pass the chicane of cooled cryo panels. The panels block the direct path, so that the gas molecules at room temperature have to hit the cryo-surface. The methane freezes out on the panels due to phase change according to the saturation pressure as described in section 4.2.1.

A SHI RDK-415D cryocooler (in combination with the heaters) is installed to refrigerate the panels to the target temperature on the top plane of the trap (left-hand side). The cryo panels are arranged with a distance of 7 mm. The holes forming the passage through the cryo panels have a radius of 5 mm. The total surface of the cryo panels is $A_{\text{cryo}} \approx 3 \times 10^{-2}\,\text{m}^2$. The cleaned gas gets fed through the outlet (top left-hand side) into the WGTS.

Methane accumulation on the cold trap inner surface

The growth rate of the methane layer is an indicator of the pump capacity and change in conductivity. In order to approximate the methane accumulation on the inner surface of the cold trap during operation, the number of CH_4 molecules is calculated. The following calculations are executed under the assumption of an ideal gas, which is sufficient for an approximation under the given conditions. The number of methane molecules for an ideal

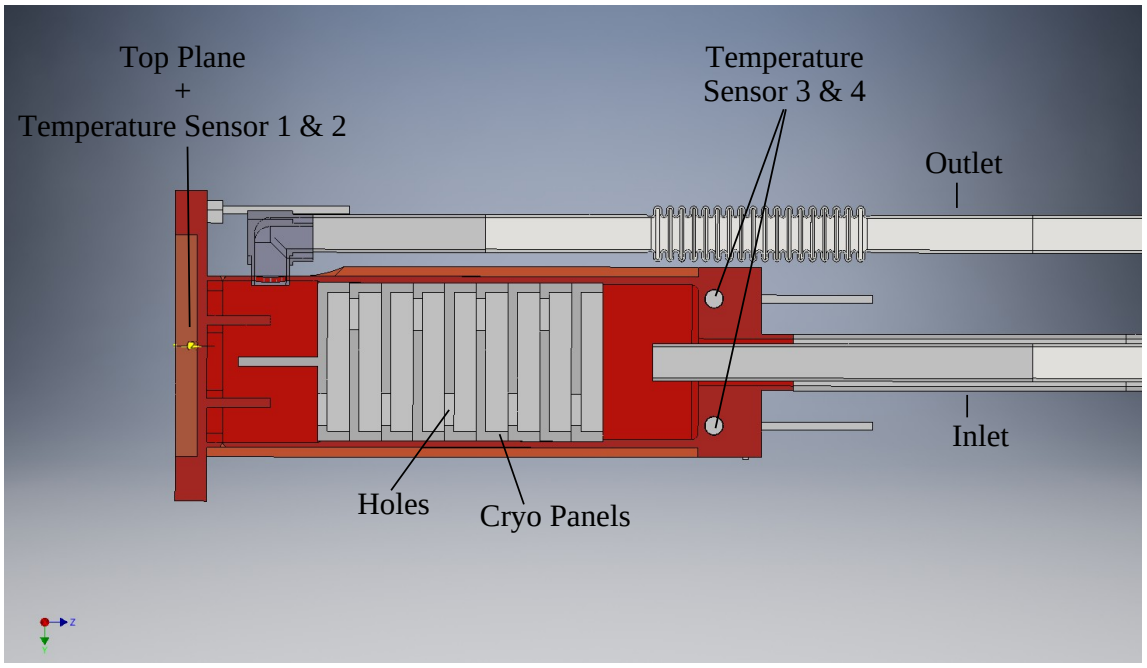

Figure 5.1.: Inner geometry of the cold trap. The cross-section is shown through the center of the cold trap along the longitudinal axis. The temperature sensors on the top (left-hand side) and bottom (right-hand side) of the cold trap monitor the cold trap temperature.

gas and an assumed CH_4 gas flow of $\phi_{CH_4} = 1 \times 10^{-4}\,\mathrm{mbar}\,\ell\,\mathrm{s}^{-1}$ is:

$$\begin{aligned} n_{CH_4}(t) &= \frac{\phi_{CH_4}}{R \cdot T_{\mathrm{gas}}} \\ &\approx 4 \times 10^{-9}\,\mathrm{mol}\,\mathrm{s}^{-1}\ . \end{aligned} \tag{5.1}$$

The gas is at room temperature $T_{\mathrm{gas}} = 300\,\mathrm{K}$ and R is the ideal gas constant.

With a methane diameter of $d_{CH_4} = 3.24\,\text{Å}$ [HH06], the covered area with a rectangular molecule distribution (78 % coverage) per second is:

$$\begin{aligned} A_{CH_4}(t) &= \left(\sqrt{n_{CH_4}} \cdot d_{CH_4}\right)^2 \\ &= 253.4 \times 10^{-6}\,\mathrm{m}^2\,\mathrm{s}^{-1}\ . \end{aligned} \tag{5.2}$$

Hence, an area of $1\,\mathrm{m}^2$ cooled surface is covered with a single layer of CH_4 every 1.1 h of operation. This is equal to a growth of $11.7\,\mathrm{a}\,\mathrm{mm}^{-1}$ for the installed cryo surface area. For a realistic time of operation the change in pump capacity and conductance is negligible.

5.1.2. Thermal sensors and heaters

The outer surface of the cold trap is shown in figure 5.2. The temperature sensors are connected to the red/white wires connected to the copper wires. They are thermally connected to the cold trap body and fixed with the aluminum tape.

The thermal connection is necessary to minimize the variation in temperature measurement, taking into account the long wire length ℓ and the relation for resistance R of the entire wire:

$$R = \rho(T) \cdot \frac{\ell}{A}\ , \tag{5.3}$$

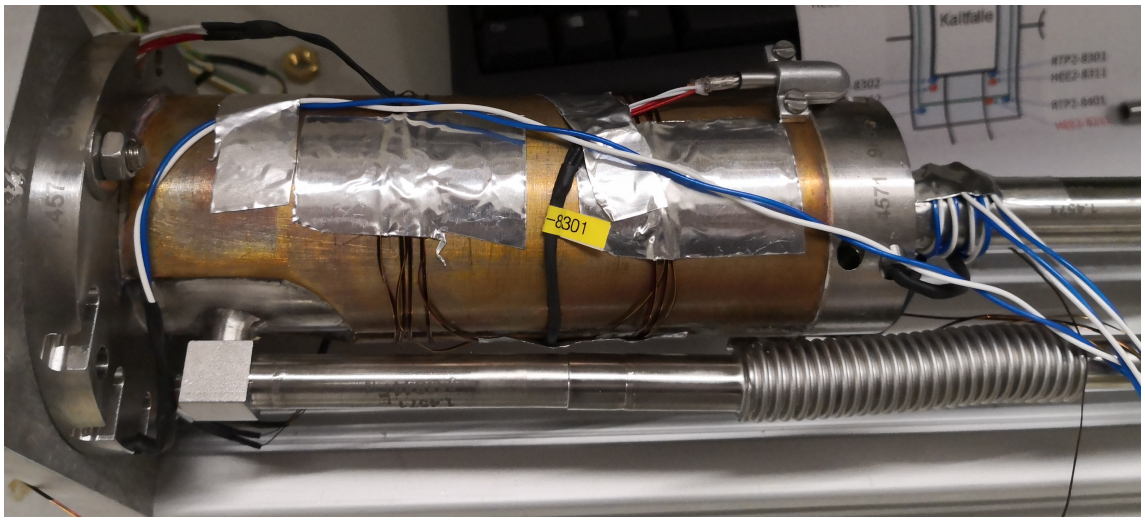

Figure 5.2.: Cold trap with thermal sensors. The thermal sensors are connected to the red/white wires, and the heating elements are connected to the blue/white on the left- and right-hand side. The exhaust pipe is shown on the bottom with bulk to absorb stress caused by temperature changes. The gas injection pipe (not shown: bulk to absorb stress caused by temperature changes) is displayed on the right-hand side.

with the cross section area A of the wire, and a temperature dependent specific resistance $\rho(T)$.

The blue and white wires are connected to heating elements installed on the top and bottom of the cold trap, regulating the baffle temperature.

5.1.3. Thermal load and shielding

The partly assembled radiation shielding is shown in figure 5.3. The shielding is located in an insulation vacuum between the outer housing (at room temperature) and the cold trap (at 30 K). The heat radiation transfer is dominant for $Kn \gg 1$ (section 4.2.2). This is the case at insulation vacuum conditions for the housing.

The purpose of the cryocooler is to cool down the cold trap and maintain stable temperature conditions in cooperation with the heaters. The cooling power must be greater than the thermal load caused by the radiation and by the gas.

The free path length Λ for molecular flow is:

$$\Lambda = \frac{1}{\sqrt{2}\pi \cdot D \cdot d^2} \,, \tag{5.4}$$

where d is the average diameter of the particle and D the particle density is given by:

$$D = \frac{N}{V} \,. \tag{5.5}$$

Hence, Λ with the ideal gas law $p \cdot V = N \cdot k_b \cdot T$ can be written as:

$$\Lambda = \frac{k_B \cdot T}{\sqrt{2}\pi \cdot p \cdot d^2} \,. \tag{5.6}$$

The pressure at the designed tritium injection flow of $\phi = 1.8\,\mathrm{mbar}\,\ell\,\mathrm{s}^{-1}$ and an assumed conductance of the cold trap in the order of $C = 1\,\ell\,\mathrm{s}^{-1}$ is with equation (4.14) in the order of $p = 1.8\,\mathrm{mbar}$.

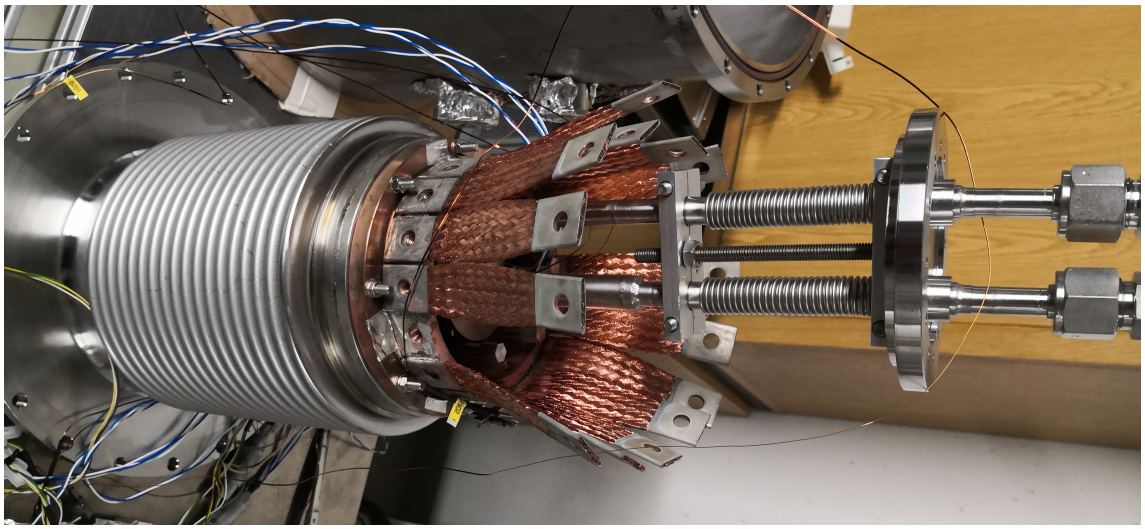

Figure 5.3.: Cold trap with radiation shielding. The bulk with a low heat transfer coefficient to reduce heat transfer is on the left-hand side. Copper strips are attached to the bulk as radiation shielding. The injection and exhaust of the cold trap is next to the copper shielding with bulks to absorb stress due to shifts caused by temperature gradient. The shielding is mechanically connected to the cryocooler (figure 5.4).

The free path length Λ is approximated to 1 mm for molecular hydrogen with a diameter of approximately $d_{\mathrm{D}_2} = 0.74\,\text{Å}$ [HH06], a gas temperature of $T = 300\,\mathrm{K}$, and the pressure p.

The characteristic length d (equation (4.8)) is in the cm scale for the given geometry of the cold trap (radius $r = 4.9\,\mathrm{cm}$ and distance of the cryo panels 7 mm). The requirement for a molecular flow $Kn > 10$ is not satisfied. To accomplish a stable cryo surface temperature, the heat transfer from gas to cryo surface $\dot{Q}_G$ has to be taken into account.

The maximal thermal flux to the cryo panel by the gas is approximated under the assumption that all gas particles are cooled by the surface leading to $\Delta T = 270\,\mathrm{K}$. The thermal energy is:

$$\Delta Q_{\mathrm{th}} = c \cdot N \cdot k_B \cdot \Delta T \ . \tag{5.7}$$

c is the specific heat capacity $c = \frac{f}{2}$ with f the degree of freedom ($f = 3$ for an ideal gas). The number of particles to cool down $N(t)$ is given by the gas flow $\phi = 1.8\,\mathrm{mbar}\,\ell\,\mathrm{s}^{-1}$:

$$N(t) = N_A \cdot \frac{\phi}{R \cdot T_{\mathrm{gas}}} \ , \tag{5.8}$$

with the Avogadro constant N_A. Assuming all particles are cooled down to the target temperature immediately, the thermal load caused by the gas can be written as:

$$\begin{aligned} \dot{Q_{\mathrm{G}}} &= \frac{3}{2} \cdot N(t) \cdot k_B \cdot \Delta T \\ &\approx 240\,\mathrm{mW} \ . \end{aligned} \tag{5.9}$$

The thermal load caused by radiation from the outer housing at ambient temperature is calculated with equations (4.9) and (4.10). The view factor is $\varphi_{21} = 1$, because the radiation shielding blocks the entire path from the housing to cold trap. The emission coefficient of the housing ε_1 is approximated with the coefficient of polished stainless steel $\varepsilon_1 \approx 0.07$ [ET20].

The cold trap radiation shielding is installed inside a bulk in order to reduce the thermal load caused by radiation. It has a low heat transfer coefficient, which decouples the cold

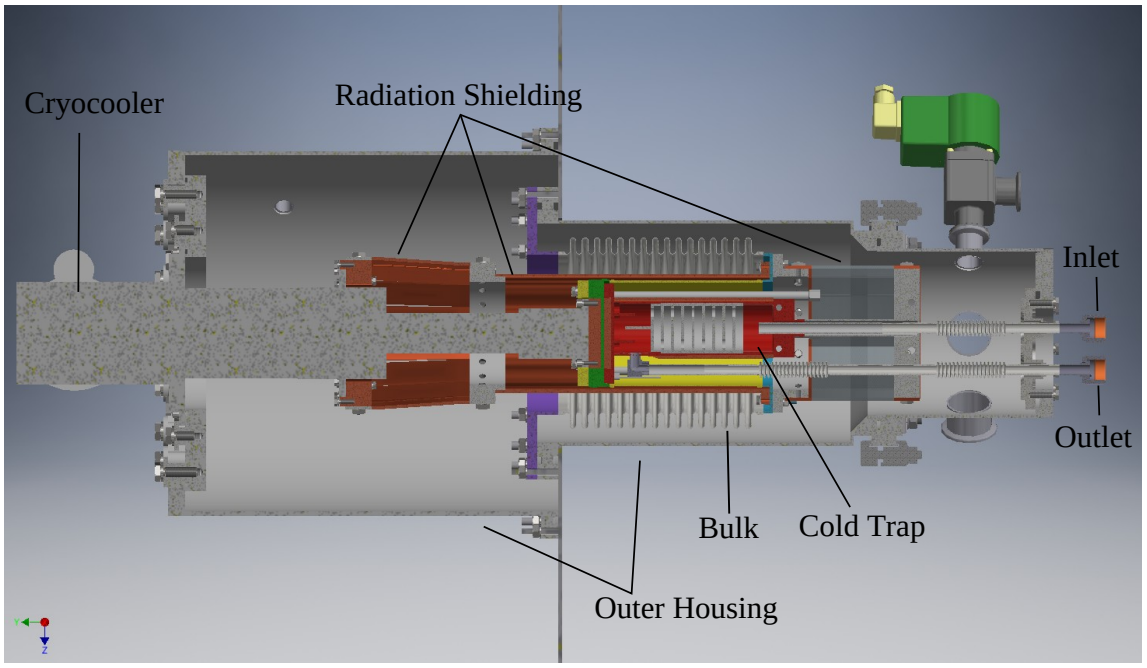

Figure 5.4.: Cold trap test setup CAD. In addition to the cold trap shown in figure 5.1, the housing needed for the isolation vacuum during the measurements, radiation shielding, the bluk for stress reduction on the mountings due to thermal changes, and the cryocooler are shown here.

trap from the outer housing. The radiation emitting area is a cylinder with $d_{\text{down}} \approx 22\,\text{cm}$, $h_{\text{down}} \approx 24\,\text{cm}$ for the part located in the lower end of the setup (figure 5.4 right-hand side) and $d_{\text{up}} \approx 35\,\text{cm}$, $h_{\text{up}} \approx 21\,\text{cm}$ for upper part (left-hand side).

The load is calculated to $\dot{Q}_R \approx 2.9\,\text{W}$ with an emission coefficient for the copper cold trap surface of $\varepsilon_2 \approx 0.02$ [ET20]. The aimed cooling power should be greater than 3.1 W with the thermal load caused by the gas. The installed cryocooler SHI RDK-415D has a cooling power of 35 W at the temperature of 50 K and 1.5 W at 4.2 K operated at an European 50 Hz grid [Gro19], which is therefore sufficient.

5.1.4. Verification of cryo temperature

The partial pressure of CH_4 for a flow of $\phi_{CH_4} = 10^{-4}\,\text{mbar}\,\ell\,\text{s}^{-1}$ and an assumed conductivity of $C = 1\,\ell\,\text{s}^{-1}$ is in the order of $10^{-4}\,\text{mbar}$. The saturation pressure curve temperature for CH_4 (figure 4.1) is approximately 50 K, for the given deuterium flow approximately 10 K.

Therefore, the cryo panel temperature of approximately 30 K is in the temperature gap where CH_4 condensates on the surface while neither D_2 or T_2 are affected.

5.1.5. Flow conditions

The flow condition inside the cold trap is approximated with the Knudsen number Kn (see equation (4.8)). The length ℓ a gas molecule can travel is estimated by the distance of the cryo panels.

The maximum pressure inside the cold trap for molecular flow conditions can be calculated with equation (5.6) at room temperature $T = 300\,\text{K}$ and the kinetic diameter for the different gas species. The results are listed in table 5.1.

Table 5.1.: Maximum pressure for molecular flow conditions. The upper pressure limits $p_{\mathrm{max}}^{\mathrm{mol}}$ for different gases, where molecular flow conditions are still present in the cold trap, are listed. d is the kinetic diameter of the gas molecule.

Gas Species	d in pm	$p_{\mathrm{max}}^{\mathrm{mol}}$ in mbar
D_2	289[1]	1.6×10^{-3}
CH_4	380[1]	0.9×10^{-3}
He	260[2]	1.9×10^{-3}
Ar	34[3]	1.2×10^{-3}
N_2	364[1]	1.0×10^{-3}

An upper molecular flow limit can be approximated for an assumed conductivity $C = 1\,\ell\,\mathrm{s}^{-1}$ of the cold trap and $p_{\mathrm{max}}^{\mathrm{mol}} = \Delta p = 10^{-3}\,\mathrm{mbar}$ ($\lambda = 70\,\mathrm{mm}$) with equation (4.14):

$$\phi_{\mathrm{max}}^{\mathrm{mol}} = 1 \times 10^{-3}\,\mathrm{mbar}\,\ell\,\mathrm{s}^{-1}\ . \tag{5.10}$$

The upper limit for transition flow conditions is accordingly ($\lambda = 0.7\,\mathrm{mm} \rightarrow p_{\mathrm{max}}^{\mathrm{trans}} \approx 10^{-1}\,\mathrm{mbar}$):

$$\phi_{\mathrm{max}}^{\mathrm{trans}} = 1 \times 10^{-1}\,\mathrm{mbar}\,\ell\,\mathrm{s}^{-1}\ . \tag{5.11}$$

The upper limit for slip flow ($\lambda = 0.07\,\mathrm{mm} \rightarrow p_{\mathrm{max}}^{\mathrm{slip}} \approx 1\,\mathrm{mbar}$) is:

$$\phi_{\mathrm{max}}^{\mathrm{slip}} = 1\,\mathrm{mbar}\,\ell\,\mathrm{s}^{-1}\ . \tag{5.12}$$

These numbers can only be regarded as a rough approximation of the real flow conditions due to the complex geometry.

5.2. Test setup for conductance and reduction measurements

The test setups for conductance and reduction measurement are designed to simulate the conditions of the future application. The gas injection and the measurement systems are explained in this section.

5.2.1. Gas injection system

The former deuterium injection system for the cryogenic pumping section at KATRIN is used as CH_4 injection system [Rö19]. The CH_4 buffer vessel in figure 5.5 replaces the D_2 buffer vessel of the original setup. The system is designed to regulate the molecular gas flow of a given gas in a range of $10^{-5}\,\mathrm{mbar}\,\ell\,\mathrm{s}^{-1}$ to $10^{-3}\,\mathrm{mbar}\,\ell\,\mathrm{s}^{-1}$ within a low error margin. A detailed description of the injection system can be found in [Fri17].

The flow is regulated via the pressure upstream an aperture using the known condutance values which are displayed in table 5.2

The conductance under molecular flow conditions depends on the molar mass of the gas species. The conductance for a gas with M_2 and a given conductance $C(M_1)$ is:

$$C(M_2) = C(M_1)\sqrt{\frac{M_1}{M_2}}\ . \tag{5.13}$$

[1] [IKM15]
[2] [MYFP06]
[3] [Bre73]

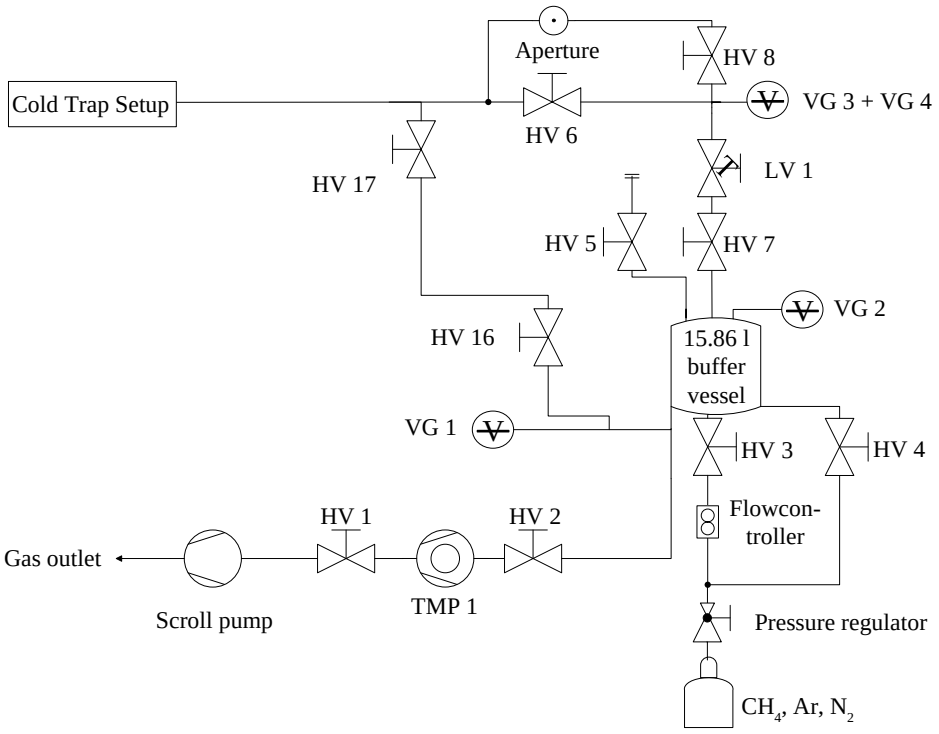

Figure 5.5.: Methane inlet system setup scheme. Manual valves are labeled as HV, control valvs as CV, leak valvs as LV, and the vacuum gauges as VG. Downstream the injection system on the upper left-hand side the connection between cold trap test setup and injection system is named as "Cold Trap Setup" and corresponds to "CH_4 injection system" in figure 5.7 and "Injection system" in 5.6. VG 1 is a Pfeiffer MPT 200 AR, VG 2 a Baratron 690A 1000 torr, VG 3 Baratron 690A 1 torr, and VG 4 a Baratron 722B 100 torr (only used for conductance measurement). TMP 1 is a Leybold Turbovac TW 70H. Partly modified version of the setup scheme is taken from [Rö19].

The pressure upstream of the aperture is controlled by leak valve LV 1 and monitored by the pressure gauge VG 3 (and VG 4 for conductance measurement). During the measurement HV 7 is fully open, LV 1 is set to target pressure level, the other valves are closed.

The flow rate is calculated according to equations (4.14) and (5.13). Values calculated for different flow rates are shown in table 5.3, the uncertainty is given by the Gaussian propagation and an uncertainty in the pressure of 0.5 %.

Table 5.2.: Conductance of the aperture for different gases. The conductance values under molecular flow conditions of the aperture used to regulate the injected gas flow are displayed for different gases. The values are taken from [Fri17].

Gas	C in $10^{-2}\,\ell\,\mathrm{s}^{-1}$	Uncertainty in $10^{-2}\,\ell\,\mathrm{s}^{-1}$
D_2	4.893	0.029
He	4.887	0.002
Ar	1.554	0.001
N_2	1.873	0.002

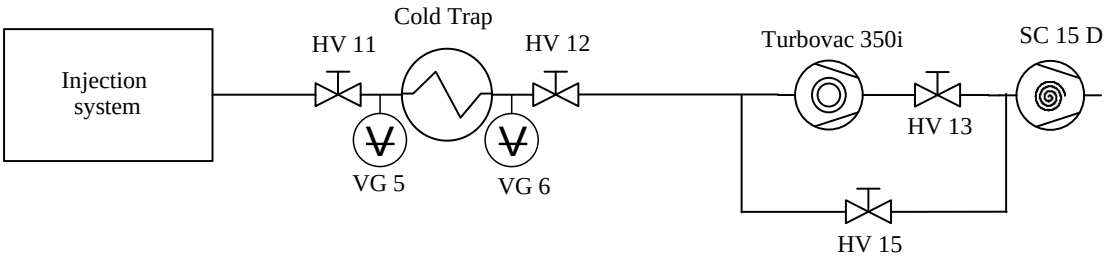

Figure 5.6.: Cold trap conductance measurement setup scheme. The "Injection system" on the left-hand side (shown in figure 5.5) is connected to the cold trap inlet via manual valve HV 11 and pressure gauges VG 5 (Baratron 722B 20 torr). The pump port (TMP Turbovac 350i and scroll pump SC 15D) on the right-hand side is attached to the cold trap outlet via pressure gauge VG 6 (Baratron 722B 20 torr) and manual valve HV 12.

5.2.2. Conductance measurement setup

The setup to measure the conductance of the cold trap is shown in figure 5.6. As gas source the injection system is installed upstream the cold trap via HV 11. VG 5 and VG 6 are Baratron 722B 20 torr pressure gauges. They measure the pressure difference caused by the conductance of the cold trap. These gauges are installed at the inlet and outlet of the cold trap. The Turbovac 350i and SC 15 D are connected downstream the cold trap via HV 12. The TMP can be bypassed by opening HV 5 and closing HV 13 for high flow rate measurements.

5.2.3. Reduction measurement setup

The setup for the reduction measurements is shown in figure 5.7. The deuterium flow to the $4\,\ell$ buffer vessel can be regulated by FC 1 to $100\,\mathrm{sccm}_{\mathrm{H_2}}$. The $4\,\ell$ buffer vessel is installed to ensure a homogeneous gas mixture from the deuterium tank and methane injection system to the cold trap. FC 2 is set to $100\,\mathrm{sccm}_{\mathrm{H_2}}$ and regulates the entire gas flow to the cold trap. The control valves CV 2 and CV 3 split the gas flow downstream of the cold trap in order to maintain the working pressure of the RGA from 10^{-11} mbar to 10^{-4} mbar. The split ratio is adjusted to maximize the gas flow at the RGA. The pressure gauges VG 4, VG 5 and VG 6 are installed to monitor the system pressure during the tests and are not used in the analysis. The RGA is used to analyze the exhaust gas of the cold trap, the Penning gauge VG7 monitors the pressure environment of the RGA.

Table 5.3.: Pressure values for different flow rates at the injection system. The pressures p is the upstream pressure of the aperture shown in figure 5.5, and correspond to the methane flow rate $\phi_{\mathrm{CH_4}}$.

$\phi_{\mathrm{CH_4}}$ in mbar $\ell\,\mathrm{s}^{-1}$	p in mbar
$(5.00 \pm 0.04) \times 10^{-6}$	2.04×10^{-4}
$(1.00 \pm 0.01) \times 10^{-5}$	4.08×10^{-4}
$(1.00 \pm 0.01) \times 10^{-4}$	4.08×10^{-3}

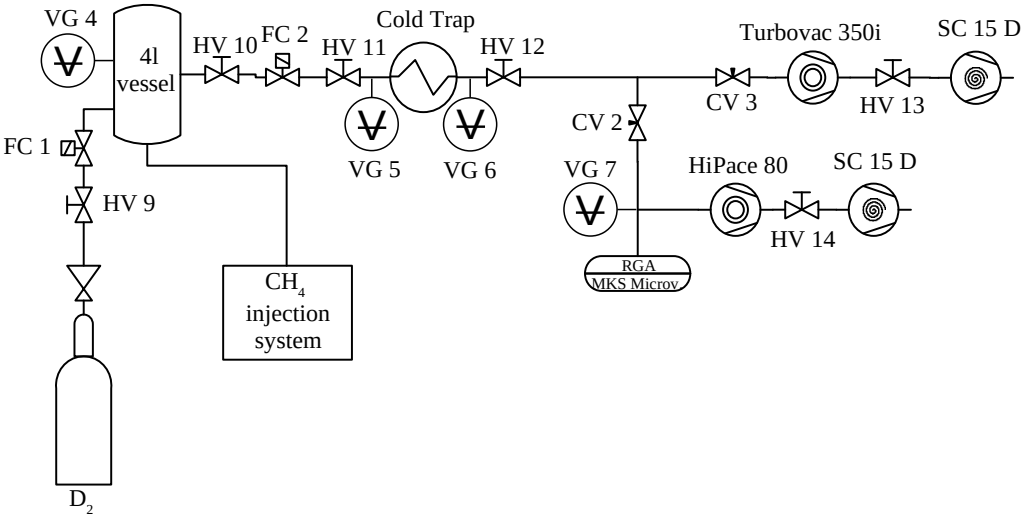

Figure 5.7.: Cold trap reduction measurement setup scheme. The D_2 tank (with flow controller FC 1), and the "CH_4 injection system" (see figure 5.5) are on the left-hand side of the cold trap. Both are connected to the $4\,\ell$ vessel with pressure gauge VG 4 (Baratron 722B 100 torr). The $4\,\ell$ buffer vessel is attached to the cold trap inlet via flow controller FC 2 and pressure gauge VG 5 (Baratron 722B 20 torr). The pressure gauge VG 6 (Baratron 722B 20 torr), which links the cold trap outlet to the main pump port (scroll pump (SC 15D) and TMP (Turbovac 350i)) and RGA (MKS Microvison Plus Quadrupol) with Penning gauge VG 7, TMP HiPace 80 and scroll pump SC 15D, is on the right-hand side of the cold trap. The control valves CV 2 and CV 3 regulate the flow to pump port and RGA.

6. Conductance measurements

The conductance of every component in a vacuum system is an important parameter. It is dependent on the geometry of the component which characterizes the fundamental fluid dynamics of a vacuum system together with pressure and gas flow.

An analytical determination can be challenging in case of a complex geometry. Therefore, the conductivity of the cold trap introduced in chapter 5 is simulated at molecular flow conditions, and tested under various flow (section 6.3) and temperature (section 6.4) conditions with different gases.

6.1. Simulation and results

In order to calculate the conductivity of the cold trap with analytical methods, many assumptions and simplifications have to be made, which makes the result inaccurate. A simulation based on simple physical models offers a good approximation to the real values and can be executed with standard computers. With the software tool MolFlow+, it is possible to simulate molecular flow conditions for any given geometry.

6.1.1. Molflow+

MolFlow+ [Ady16] is a software tool provided by CERN to simulate the molecular flow inside complex structures. It uses Monte Carlo simulations to calculate the pressure distribution in an ultra-high vacuum environment.

The test particle Monte Carlo method (TPCM) is used in the simulation. This method uses a limited number of test particles to represent the larger number of particles matching the parameters of e.g. de- and adsorption, pumping speed. Generated particles in the system are traced until they are pumped during the simulation. Collisions with the walls are registered and stored if necessary, while ignoring the ones between gas particles since the free path length is larger than the characteristic length of the system under molecular flow conditions.

The number of hits and the distribution of molecule velocity is determined with a ray-tracing engine and a custom GUI framework, in order to calculate the pressure and density.

The sources are represented by facets which are the geometrical representation of the object's surface. This applies to a steady-state simulation with a continuous gas influx and constant pumping speed. The particle rate $\mathrm{d}N_f/\mathrm{d}t$ of each facet is calculated with the predefined outgassing rate and the ideal gas equation:

$$p \cdot V = N_f \cdot k_B \cdot T_f \ . \tag{6.1}$$

T_f is the temperature of the gas emitted by the corresponding facet, hence the facet temperature. MolFlow+ automatically chooses the start position for a particle if more than

one facet emits particles. The probability, that a facet is emitting a particle, is proportional to the local flux on the facet. The particle position on each facet is chosen randomly with a uniform distribution on the surface. The number of particles in a system can rise very fast, even at low flow rates. Each simulated particle represents a higher number of real particles in order to reduce the computing time and to allow simulation on a standard desktop PC.

The direction of generated and rebound particles is determined by the Knudsen cosine law. The Mersenne-Twister algorithm is used to generate random numbers between 0 and 1 to get the angles between particles and the azimuth angle.

The Maxwell-Bolzmann distribution determines the speed of particles under ideal gas conditions. According to the sojourn time and the so caused thermalization, the speed of the particles changes at every collision. Due to the simulation method where the particles are generated as flux through facet, fast particles pass and hit a surface more frequently. The speed distribution of these particles can be calculated with a given probability density function. They are generated according to the numerical inversion method.

After hitting a facet, the particle is either pumped or bounced off, depending on the sticking coefficient of the facet. After direction and velocity are calculated, MolFlow+ uses a ray tracing algorithm to determine the location of the next hit in case of a rebound.

The geometrical surface area A and volume V extracted from the CAD file are needed in order to calculate the physical parameters of the simulation. The number of collisions per second and per area is the hit rate z on a facet with:

$$z = \frac{N_{\text{hit}} \cdot K}{A} \ . \tag{6.2}$$

The counted number of hits N_{hit} on a facet is multiplied by the factor K, divided by the facet area A. K is the factor by which the number of simulated particles are reduced compared to the particles in a real system with the set values. This takes into account that only a fraction of particles can be simulated in order to run on a desktop PC.

The pressure on the walls is defined by momentum exchange from particles hitting a facet, divided by the facet area. Every facet has a counter to store the number of hits N_{hit}, the total orthogonal momentum change $I_\perp$ and the reciprocals of the orthogonal speed components $v_\perp^{-1}$. The pressure can be calculated by:

$$p = \frac{\sum I_\perp \cdot K}{A} \ . \tag{6.3}$$

The number of particles in a volume defines the density which cannot be calculated directly, because MolFlow+ only simulates events on the surface. The particle count in the volume $A \cdot \Delta t \cdot v_\perp$ is related to the number of collisions on the surface A, which is needed to calculate the density. A molecule with a travel speed of $v_\perp$ heading to the facet will hit the surface in a time interval Δt if it is closer than $\Delta t \cdot v_\perp$, hence,

$$n_{\text{collisons}} = \frac{N}{V} \cdot A \cdot \Delta t \cdot v_\perp \ . \tag{6.4}$$

The density can be calculated by using the $v_\perp^{-1}$ counter, integrating N/V over the velocity distribution function, and with the speed distribution on an adjacent facet:

$$\langle n \rangle_{\text{volume}} = \frac{N_{\text{hit}}}{\sum v_\perp^{-1}} \ . \tag{6.5}$$

The documentation for the software can be found in [Ady16].

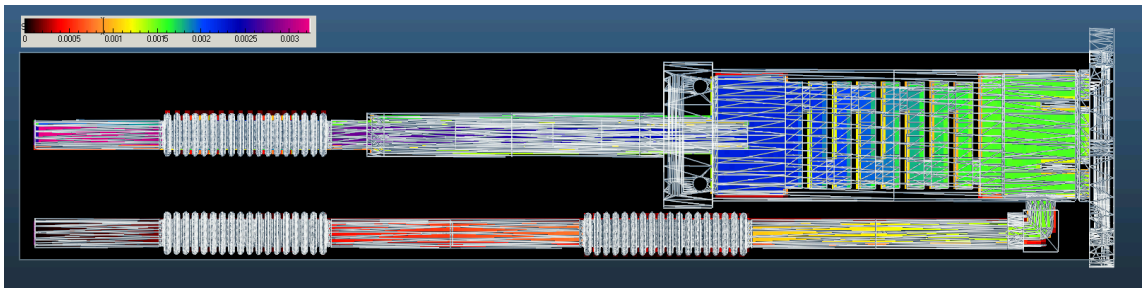

Figure 6.1.: Pressure distribution cold trap simulation. The cross section of the tested cold trap is shown with simulated pressure distribution. The gas injection tube is on the top left-hand side, the gas exhaust tube is on the bottom. Violet indicates regions of high pressure, and red regions of low pressure. The color scale is linear.

6.1.2. Results

A MolFlow+ simulation with the cold trap CAD model is executed to determine the conductance. The conductance C is calculated with equation (4.14), where Δp is the pressure difference at the start of the intake p_{in} and the end of exhaust p_{out}.

The pressure distribution inside the cold trap (figure 6.1) shows a high pressure gradient between intake and exhaust representing a low conductivity. The results of the simulation for a flow rate of $\phi = 10^{-3}\,\text{mbar}\,\ell\,\text{s}^{-1}$ for different gases and temperatures are listed in table 6.1. The facet covering the intake and representing the gas source was assumed to be opaque for this simulation.

The sticking probability of all facets, except the facet representing the pump, is set to 0 and the pump is set to 1. No molecules will be adsorbed by the walls and every simulated molecule will eventually hit the pump with these sticking parameters.

A facet covering the intake is chosen as a source with a cosine distribution to generate the required particle flow ϕ. The initial gas temperature is controlled by the source facet temperature. The pump is represented by a facet with sticking probability 1 covering the exhaust. The simulation is based on the ideal gas law and therefore the gas type is controlled by the molecular weight.

The simulation in the tested temperature range for a molecular flow environment shows that the pressure at the intake is in the same magnitude as the injection flow, the pressure at end of the exhaust is two to three magnitudes lower than the intake pressure.

All results are in the magnitude of $10^{-1}\,\ell\,\text{s}^{-1}$ depending on the gas type and temperature.

6.2. Measurement procedure

The setup scheme of the methane injection system is shown in figure 5.5 and the scheme of the cold trap setup in figure 5.6. The following procedure is carried out in order to experimentally determine the conductance of the cold trap under test for a wider flow range.

1. The cold trap is preconditioned to the target temperature by the cold head and heaters.
2. The $15.863\,\ell$ buffer vessel in figure 5.5 is filled with the necessary gas type up to approximately 0.5 bar using HV 4.
3. The desired gas flow is adjusted via the leak valve LV 1 and monitored by the pressure gauges VG 3 and VG 4 (depending on the flow rate/pressure level) upstream of the aperture.

4. The pressure upstream of the aperture is stabilized for approximately 10 min in order to increase the statistics.
5. The input and output pressure is measured by VG 5 upstream and VG 6 downstream the cold trap.

This procedure is followed up to a pressure of 1 bar upstream the aperture. The gas flow corresponding to a pressure above 1 bar can not be stabilized which does not allow an accurate read-out. Therefore, the pressure is adjusted to the maximum range of VG 4 in order to achieve a higher gas flow. The TMP is bypassed with HV 15 open and HV 13 closed in order to reach flow rates that exceed the capability of the TMP. The pressure readings of the gauges are recorded continuously and a conductance curve is calculated.

6.3. Gas dependence of conductance

The conductance is dependent on the gas type and temperature, as shown in equations (4.14) and (4.17). Therefore, the cold trap is tested at room temperature for different gas species.

6.3.1. Low-flow regime

This test is performed in order to determine the conductance of the cold trap for helium, argon, and nitrogen with 99.999 % gas purity at room temperature in a low-flow environment.

The conductance for a low-flow regime is shown in figure 6.2 for nitrogen. The flow-conductance relation has an in first order linear behavior for a flow range of $10^{-3}\,\mathrm{mbar}\,\ell\,\mathrm{s}^{-1}$ to $10^{-2}\,\mathrm{mbar}\,\ell\,\mathrm{s}^{-1}$ and is fitted by:

$$C(\phi) = \phi \cdot m + C_0 \,. \tag{6.6}$$

A transitional flow at the edge of molecular flow for the lowest pressure readings is present during this measurement according to the calculations in section 5.1.5.

The data points are the mean value of a stabilized pressure recorded for approximately 10 min. The error bar is the standard deviation of the mean pressure, which is added to the systematic error for uncertainty of the Baratron pressure gauges of 0.5 % [MKS20] using equation (4.15) and the Gaussian propagation of uncertainty.

Table 6.1.: Conductance simulation for different gases. The MolFlow+ simulation results are listed for helium, argon, nitrogen, methane, and deuterium with a flow rate of $10^{-3}\,\mathrm{mbar}\,\ell\,\mathrm{s}^{-1}$ at different temperatures. p_{in} is the intake pressure and p_{out} the exhaust pressure.

Gas	T in K	p_{in} in mbar	p_{out} in mbar	C in $\ell\,\mathrm{s}^{-1}$
He	5	1.9×10^{-3}	3.2×10^{-6}	0.53
He	30	2.2×10^{-3}	7.7×10^{-6}	0.46
He	80	2.5×10^{-3}	1.3×10^{-5}	0.40
He	300	3.2×10^{-3}	2.4×10^{-5}	0.31
Ar	300	1.0×10^{-2}	7.7×10^{-5}	0.10
N_2	300	8.7×10^{-3}	6.4×10^{-5}	0.12
CH_4	300	6.5×10^{-3}	4.9×10^{-5}	0.16
D_2	300	3.3×10^{-3}	2.4×10^{-5}	0.31

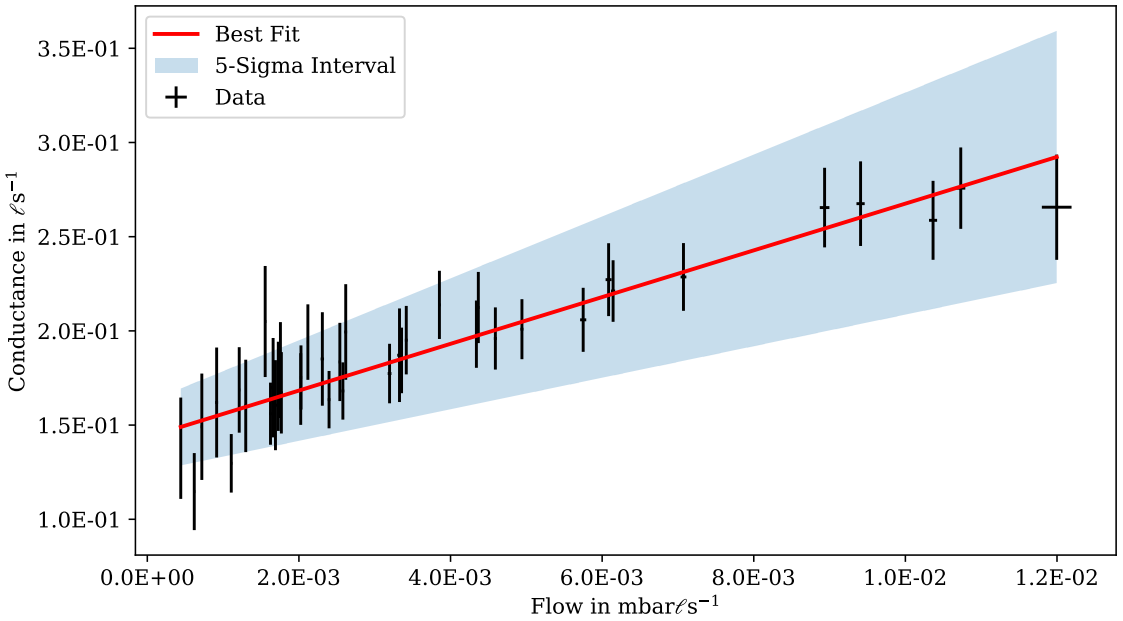

Figure 6.2.: Flow-conductance dependency for cold trap with nitrogen gas at room temperature. The conductance of the cold trap at room temperature is shown for N_2 depending on the gas injection flow. The flow regime is on the edge of a molecular flow. The data is fitted with linear orthogonal distance regression, the error bars are used as a weight.

The injection flow is calculated using the pressure upstream and downstream the aperture of the injection system. The conductance of the aperture under molecular flow conditions for the gases used is known and can be found in table 5.2. The aperture is operated under non-molecular flow conditions, therefore the conductance value must be determined. The conductance of a thin aperture for non-molecular flow environments can be calculated using the Knudsen number and the ratio C_{Kn}/C_{mol} that can be found in [JKS98]. The Knudsen number for a thin aperture is [JKS98]:

$$Kn = \frac{\pi \cdot \eta \cdot \overline{c}}{4 \cdot d \cdot p} \,, \tag{6.7}$$

d is the diameter of the aperture hole, η the viscosity of the gas, and $\overline{c}$ the thermal velocity.

In order to take the uncertainty in the adjustment into account, the systematic uncertainty was increased by 5 % from the values determined by the Gaussian propagation with a pressure uncertainty of 0.5 % and the uncertainty in C_{mol} in table 5.2. The values listed in table 6.2 were determined by a linear orthogonal regression fit of the data, using the error bars as weigh. The intercept values of these measurements can be interpreted as conductance under molecular flow conditions, and are in agreement with the simulated values in table 6.1. The measurements for helium 300 K and argon 300 K are shown in the figures C.1 and C.2.

6.3.2. High-flow regime

The conductivity flow dependence for a flow in the range from 10^{-1} mbar $\ell\,s^{-1}$ to 6 mbar $\ell\,s^{-1}$ is shown in figure 6.3. The conductivity follows roughly a quadratic or exponential function. Compared to the behavior of a thin aperture [JKS98] it can be assumed that for the tested gases the conductivity reaches saturation at a gas flow in the order of 10^1 mbar $\ell\,s^{-1}$. It was not possible to achieve higher flows than 6 mbar $\ell\,s^{-1}$ for helium which corresponds to a conductance of $C \approx 5\,\ell\,s^{-1}$ due to the experimental setup. The maximal possible flow for

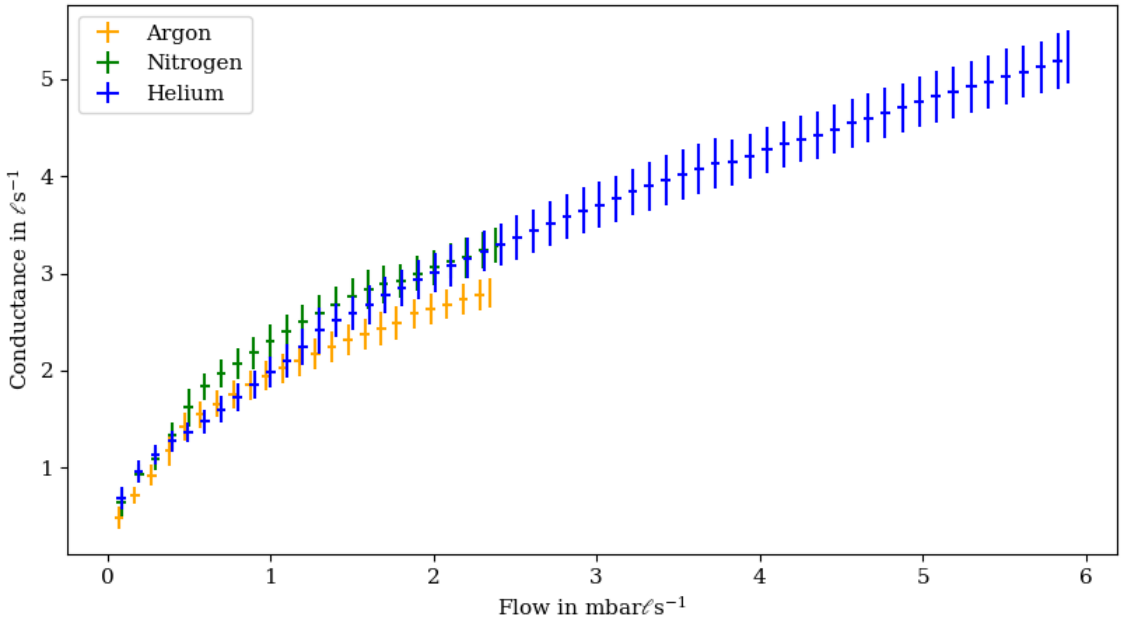

Figure 6.3.: Cold trap flow-conductance dependency for helium, argon, and nitrogen. The measured conductance values of the cold trap at room temperature are shown for helium (blue), argon (yellow), and nitrogen (green). The flow-conductance dependency is displayed in a transition to slip flow regime.

argon and nitrogen match a conductance of $C \approx 2.5\,\ell\,\mathrm{s}^{-1}$. A continuum flow regime should be accomplished for a flow in the magnitude of $1\,\mathrm{mbar}\,\ell\,\mathrm{s}^{-1}$ according to the calculations in section 5.1.5.

The conductivity depends on the viscosity of the fluid in laminar flow which is in case of a pipe:

$$C = \frac{\pi \cdot \mathrm{d}^4}{128 \cdot \eta \cdot \ell} \cdot \overline{p}\,, \tag{6.8}$$

d is the pipe diameter, ℓ the length, $\overline{p}$ the mean pressure, and η the fluid viscosity [Gmb13]. Laminar flow can be assumed to approximate the conductivity in first order. The viscosity of the used gases is at room temperature [Lid03]:

$$\begin{aligned} \eta_{\mathrm{Ar}} &= 22.9\,\mu\mathrm{Pa\,s} \\ \eta_{\mathrm{He}} &= 20.0\,\mu\mathrm{Pa\,s} \\ \eta_{\mathrm{N_2}} &= 17.9\,\mu\mathrm{Pa\,s}\,. \end{aligned} \tag{6.9}$$

The discrepancies of these values are negligible in respect to the accuracy of the measurement. Therefore, the displayed data can be considered identical in a flow regime of $10^{-1}\,\mathrm{mbar}\,\ell\,\mathrm{s}^{-1}$

Table 6.2.: Conductance values in low-flow regime for different gases. The fit parameters of equation (6.6) are displayed for helium, argon, and nitrogen at room temperature. The corresponding plots are shown in figures C.1,C.2, and 6.2.

Gas	m in mbar^{-1}	C_0 in $10^{-1}\,\ell\,\mathrm{s}^{-1}$
He	6.5 ± 1.7	3.91 ± 0.17
Ar	9.9 ± 1.3	1.38 ± 0.05
N_2	12.4 ± 0.8	1.44 ± 0.04

Table 6.3.: Conductance values in low-flow regime for helium at different temperatures. The fit parameters of equation (6.6) are shown for helium at 5 K, 30 K, and 80 K. The corresponding plots are shown in C.5, C.4, and C.3.

T in K	m in mbar^{-1}	C_0 in $10^{-1}\,\ell\,\mathrm{s}^{-1}$
5	27.4 ± 3.0	5.78 ± 0.38
30	38.4 ± 3.1	3.63 ± 0.26
80	26.0 ± 1.6	3.15 ± 0.15

to $2\,\mathrm{mbar}\,\ell\,\mathrm{s}^{-1}$. The data points are mean values of multiple measurements in an interval width of $0.1\,\ell\,\mathrm{s}^{-1}$. The error bar of the flow ϕ is the standard deviation of the mean. A malfunction of the two Baratron pressure gauges VG 4 and VG 5 was discovered at higher pressure values, which led to a constant value added to the reading of the gauges. It was not possible to repeat all the measurements, due to the late discovery. Therefore, a correction was applied to the previously measured data. Due to the constant nature of the error, it was possible to correct the values. The conductance uncertainty takes this circumstance into account, and an additional 5 % error of the reading value is added in addition to the standard deviation of the interval. The systematic uncertainty is analogue to section 6.3.2, but negligible in comparison.

The hierarchic derived by the viscosity is noticeable between argon and helium/nitrogen for $\phi > 2\,\mathrm{mbar}\,\ell\,\mathrm{s}^{-1}$, the gas with a higher viscosity leads to a lower conductance.

6.4. Temperature dependence of conductance

The conductance is dependent on the gas velocity and therefore temperature at molecular flow conditions. Gas fed into the system has a room temperature of about 300 K, while the cryo panels can cover a range from 5 K to 300 K. The cold trap temperature dependency is tested with helium at 5 K, 30 K, 80 K, and 300 K over the full flow range which is possible with the given setup.

6.4.1. Low-flow regime temperature dependence

The conductance for a low-flow regime in the range of $10^{-3}\,\mathrm{mbar}\,\ell\,\mathrm{s}^{-1}$ to $10^{-2}\,\mathrm{mbar}\,\ell\,\mathrm{s}^{-1}$ is tested at 5 K (C.5), 30 K (C.4), and 80 K (C.3) for helium gas with an injection temperature at 300 K. As in the previous test, the conductance has in first order a linear relationship to the gas flow. The fitted values can be found in table 6.3.

The reading for C_{mol} at 5 K is in agreement with the simulation, the values for 30 K and 80 K are below the expected value while $C_{80\,\mathrm{K}} = (0.32 \pm 0.02)\,\ell\,\mathrm{s}^{-1}$ value is below the value at $C_{300\,\mathrm{K}} = (0.39 \pm 0.02)\,\ell\,\mathrm{s}^{-1}$ (He in table 6.2). An explanation can be the sensitivity of the pressure gauges and the interpretation of C_{mol} as the intercept. With a steeper gradient, the approximation becomes less accurate.

6.4.2. High-flow regime temperature dependence

The conductivity temperature dependency at higher flow rates is shown in figure 6.4. It can be seen that the course of the conductance values is dependent on the cold trap temperature. The conductivity for laminar-flow conditions depends on the viscosity of the fluid (see equation (6.8)). This can be approximated by different theories like the elastic-sphere kinetic theory [CS70]:

$$\eta = \frac{5}{16 \cdot \sigma^2} \sqrt{\frac{k_B \cdot m \cdot T}{\pi}}\,, \tag{6.10}$$

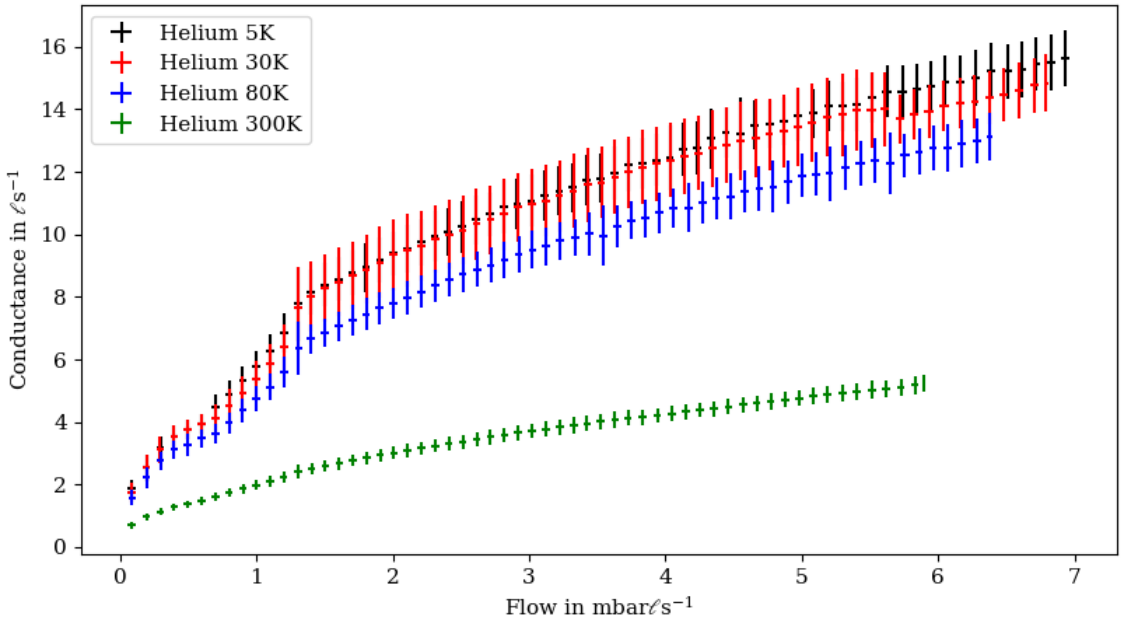

Figure 6.4.: Cold trap flow-conductance dependency for helium at a cold trap temperature of 5 K**,** 30 K**,** 80 K **and** 300 K**.** The condutance values for helium at 5 K (black), 30 K (red), 80 K (blue), and 300 K (green) are shown. The flow-conductance dependency is displayed in a transition to slip flow regime.

σ is the diameter and m the mass of the gas molecule. The point-centres of force model [CS70] is another approximation of the viscosity:

$$\eta = \eta' \left(\frac{T}{T'} \right)^s \ . \tag{6.11}$$

The primed values are known and $s = 0.657 \pm 0.001$ for Helium in a temperature range from 43 K to 1073 K.

Another possibility to describe the viscosity is the Lennard-Jones model [BB02][CS70]:

$$\eta = \frac{5}{16} \cdot \frac{\sqrt{m \cdot k_B \cdot T}}{\sqrt{\pi} \cdot \sigma^2 \cdot \Omega(T)} \ , \tag{6.12}$$

with

$$\begin{aligned} \Omega(T) = {} & 1.16145 \cdot (T^*)^{-0.14874} \\ & + 0.52487 \cdot \exp(-0.7732 \cdot T^*) \\ & + 2.16178 \cdot \exp(-2.43787 \cdot T^*) \ , \end{aligned} \tag{6.13}$$

while $T^* = T/\epsilon^*$ with the Lennard-Jones parameter $\epsilon* = \epsilon/k_B$ (for helium $\epsilon^* = 10.2$ K). These models account for different interaction forces and apply to different temperature ranges and various gas species.

The theoretical conductivity values are calculated for 80 K using the elastic-sphere kinetic, the point-centres of force, and the Lennard-Jones model in figure 6.5. In order to determine the theoretical viscosity, the measured values for 300 K are used as input values. The point-centres of force and Lennard-Jones model are the most accurate for 80 K reading. At 30 K (see figure C.7) the most accurate approximation is given by the elastic-sphere model. All three models are not suitable for an approximation at 5 K (see figure C.6). The

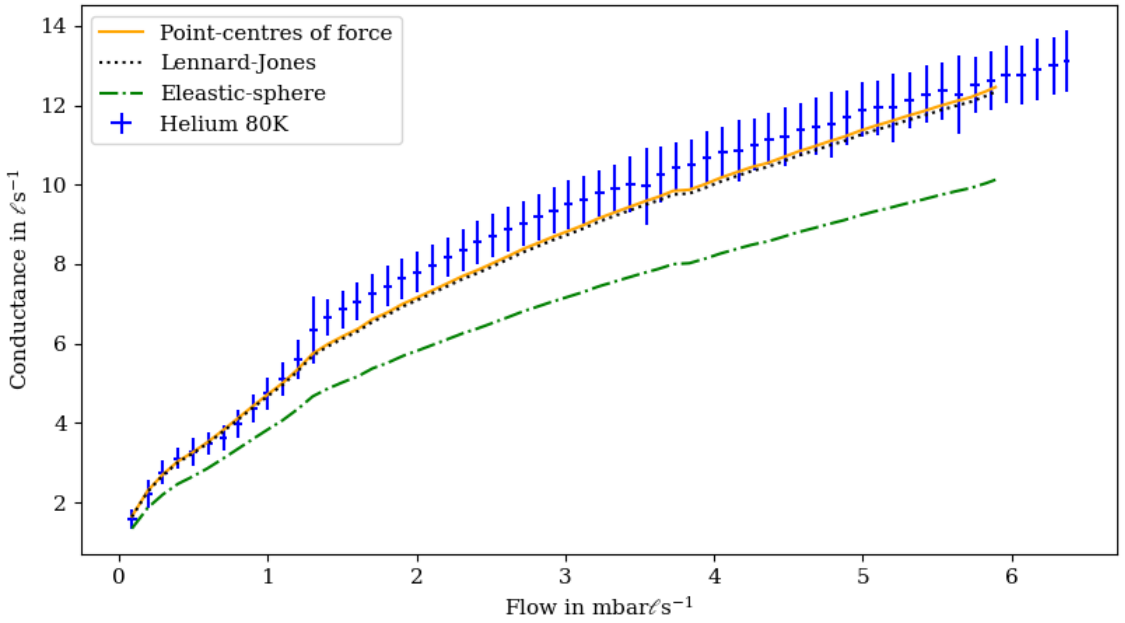

Figure 6.5.: Theoretical cold trap conductivity for helium at 80 K**.** The theoretical conductance values for different models are displayed. The values calculated for the elastic-sphere kinetic model are the green dash-dotted line, for the point-centres of force model the yellow line, and for the Lennard-Jones model the black dotted line. The measured values for helium at 80 K are plotted in blue.

parameter used in the point-centres of force model should not be used for temperatures below 43 K for helium. The Lennard-Jones parameter for helium is given for a range from 3 K to 3000 K, allowing the application to all tested temperatures.

One explanation for the inaccuracies of these models at temperatures below 80 K is that the temperature gradient between gas and cold trap increases. Furthermore, it was assumed that the mean pressure inside the cold trap $\overline{p}$ is constant for a given flow, but it varies due to the change in conductivity. Within the given limitations, the theoretical values show the expected behavior and agree with the measured values.

6.5. Summary

The aim of these measurements was to determine the conductivity under the flow conditions for which the cold trap is designed, therefore a flow in the order of 1 mbar $\ell\,\mathrm{s}^{-1}$ was required. With the used setup, it was possible to investigate the boundary to molecular flow. In order to verify the measured values under molecular flow conditions, flow simulations of the cold trap were performed with MolFlow+. The experimental results show a good agreement to the simulated ones.

Additionally, the conductance was determined for temperatures at which the cold trap is operated, as well as for the edge cases 5 K and at room temperature. With the result of this chapter, it is now possible to determine the conductance for a given gas temperature for future purposes of the cold trap.

7. Cold trap reduction measurements

The gas reduction capability is the main purpose of the cold trap. It is tested with a methane-deuterium mixture to simulate the tritium flow conditions in the WGTS. The device is examined with different parameters to determine its capabilities.

In order to interpret the measurements under pumping conditions, a reference measurement at room temperature is carried out in section 7.2. The pumping capabilities and behavior of the cold trap are investigated in section 7.3. The cold trap is tested with a deuterium-only injection, a methane-only injection and a deuterium-methane mixture. In order to investigate the temperature behavior, the cold trap is cooled down from room temperature to 20 K while a deuterium-methan mixture is injected in section 7.4. In order to back up the results of the reduction measurement, the empty and loaded cold trap is analyzed and the amount of the released methane is compared with the injected one in the reduction measurement in section 7.5.

7.1. Measurement procedure

A deuterium-methane mixture is generated and fed through the cold trap to test the reduction of methane with a non-radioactive gas mixture. The setup scheme of the methane injection system is shown in figure 5.5 and the scheme of the cold trap setup in figure 5.7. The following procedure is executed to create the required mixture, :

1. The 15.863 ℓ buffer vessel in figure 5.5 is filled with approximately 500 mbar using HV 4, HV 2, HV 3, HV 5, and LV 1 are closed.
2. CV 2 and CV 3 are both fully opened before gas injection to ensure the RGA does not operate in vacuum conditions larger than 10^{-5} mbar.
3. Valve HV 10 is opened to connect the upstream system to the cold trap (HV 6 and HV 8 open). The deuterium flow is set to 100 $\mathrm{sccm}_{\mathrm{H_2}}$ ($\phi_{\mathrm{D_2}} \approx 1.18\,\mathrm{mbar}\,\ell\,\mathrm{s}^{-1}$) via flow controller FC 1 (HV 9 open).
4. When the pressure at VG 3 is stable, HV 6 gets closed.
5. The pressure is set to the designated level via LV 1 to establish a constant methane flow.
6. CV 3 is set to maximize the total pressure at the RGA (up to 10^{-5} mbar) to increase the possibility of detecting methane flow.
7. The gas flow is analyzed by the RGA.

In order to determine the methane reduction factor by the cold trap, the methane and deuterium injection systems are decoupled by closing HV 10. CV 3 is closed and CV 2 is fully opened to maximize the sensitivity of the detection system. The cold trap is heated until released methane can be detected.

Table 7.1.: Methane fingerprint. The relative values are listed for the different gas species present in methane gas. The values are normalized to CH_4. [Lin97]

Gas species	Mass in u	Relative value in %
C	12	3.80
CH	13	10.69
CH_2	14	20.42
CH_3	15	88.79
CH_4	16	100.00
$^{13}CH_4$	17	1.64

Methane is a mixture of more than one gas specie (CH_4 with the corresponding mass of 16 u). In order to identify methane in the RGA spectrum, the measured values are compared with the relative values listed in table 7.1. An uncertainty of 10 % in the relative fingerprint peaks for each mass is allowed in order to positively identify methane. This takes into account the natural variations in the mixture of the gas species, the uncertainty of the RGA, and the presence of water and other out gassing of the system downstream the cold trap[1]. The time integrated fingerprint scans are compared with the integrated methane flow rate and the pressure loss of the 15.863 ℓ vessel which should be equal to the integration of the flow rate.

7.2. Reference measurement at room temperature

The measurement under the room-temperature environment is executed in order to determine the setup capabilities.

The measurement with 100 sccm_{H_2} deuterium and methane flow is shown in figure 7.1. The gas correction factor of deuterium and methane are $K_{D_2} = 0.35$ and $K_{CH_4} = 1.4$ for the installed RGA [MI20]. The RGA pressure reading for deuterium is represented by the 4 u pressure $p_{D_2}^{RGA} = 1.07 \times 10^{-6}$ mbar at 1.54 h. The methane pressure is represented by the sum of the methane species partial pressures with $p_{CH_4}^{RGA} = 1.54 \times 10^{-7}$ mbar.

The pumping speed S depends on the relative molecular mass [Vac03]. With the plotted course of the pumping speed over the molecular weight for the given values of the installed TMP (listed in table B.1), the pumping speed for deuterium and methane can be approximated to $S_{D_2} \approx 58\,\ell\,\mathrm{s}^{-1}$ and $S_{CH_4} \approx 67\,\ell\,\mathrm{s}^{-1}$.

For a configuration with split gas flow, the gas flow ratio is given by:

$$\frac{\phi_{D_2}}{\phi_{D_2}^{RGA}} = \frac{\phi_{CH_4}}{\phi_{CH_4}^{RGA}} \,, \tag{7.1}$$

with ϕ_{D_2} and ϕ_{CH_4} the injected deuterium and methane flow, $\phi_{D_2}^{RGA}$ and $\phi_{CH_4}^{RGA}$ the gas flow at the RGA. The flow at the RGA can be calculated with the pumping speed of the installed TMP and the partial pressure of the gas:

$$\phi_i^{RGA} = S_i \cdot \frac{p_i^{RGA}}{K_i} \,, \tag{7.2}$$

[1] The measurements show that the components downstream of the cold trap create a permanent background which is not negligible. This background is present because the setup has not been baked out. The background decreases over the course of the measurements, which are carried out over several weeks.

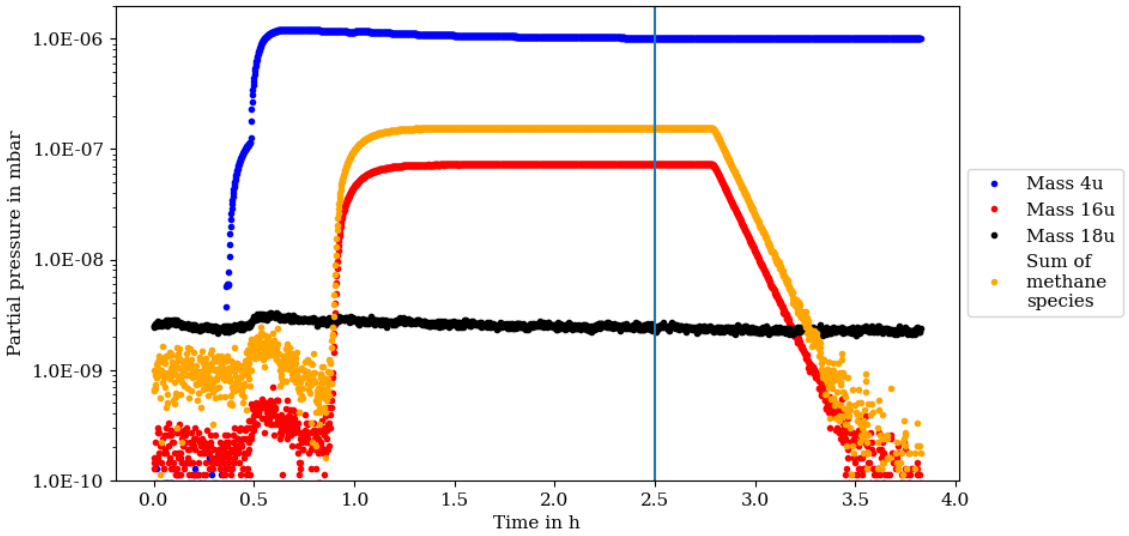

Figure 7.1.: Deuterium methane injection at 290 K**.** The constant deuterium injection of 100 $\mathrm{sccm}_{\mathrm{H_2}}$ is represented by the 4 u pressure reading (blue), the methane injection by the 16 u pressure reading (red) as well as the sum over the methane species (orange). The methane injection is constant in the time period of 1 h to 2.8 h. The constant water background is indicated by the 18 u pressure reading (black). The blue line at 2.5 h marks the position of the spectrum with the best agreement to the methane composition[2]in table 7.1, shown in figure D.13.

i is the gas specie. The methane flow is calculated with equations (7.1) and (7.2) and the Gaussian propagation of uncertainty. The exact values of the uncertainty for the following devices and values are not known, but are conservatively estimated to 10 % uncertainty in RGA pressure reading, 10 % uncertainty for the gas correction factors, 10 % uncertainty in the pumping speed, and a 30 % uncertainty in deuterium flow:

$$\begin{aligned}\phi_{\mathrm{CH_4}} &= \phi_{\mathrm{D_2}} \cdot \left(\frac{p^{\mathrm{RGA}}_{\mathrm{CH_4}} \cdot S_{\mathrm{CH_4}}}{K_{\mathrm{CH_4}}} \cdot \frac{K_{\mathrm{D_2}}}{p^{\mathrm{RGA}}_{\mathrm{D_2}} \cdot S_{\mathrm{D_2}}} \right) \\ &= (4.91 \pm 1.90) \times 10^{-2}\,\mathrm{mbar}\,\ell\,\mathrm{s}^{-1}\,. \end{aligned} \tag{7.3}$$

With a methane flow of $5 \times 10^{-2}\,\mathrm{mbar}\,\ell\,\mathrm{s}^{-1}$ corresponding to a pressure reading in the magnitude of $10^{-7}\,\mathrm{mbar}$, a minimal methane flow of approximately $10^{-4}\,\mathrm{mbar}\,\ell\,\mathrm{s}^{-1}$ can be recognized with CV 2 and CV 3 fully opened. The spectrum in figure D.13 shows the expected composition of methane and deuterium.

The constant water background, which can lead to a negative methane identification at a flow of $10^{-4}\,\mathrm{mbar}\,\ell\,\mathrm{s}^{-1}$, has to be considered.

7.3. Measurements at 30 K

In order to determine the pumping characteristics of the cold trap, different gas mixtures were injected and analyzed at a cold trap temperature of 30 K in the following.

7.3.1. Deuterium injection

In order to get a reference measurement for the analysis of the background at 30 K cold trap temperature and gas flow, the measurement was performed with deuterium only. A

[2] An algorithm compared all RGA spectra in order to identify the measurement with the lowest difference to the methane composition listed in table 7.1

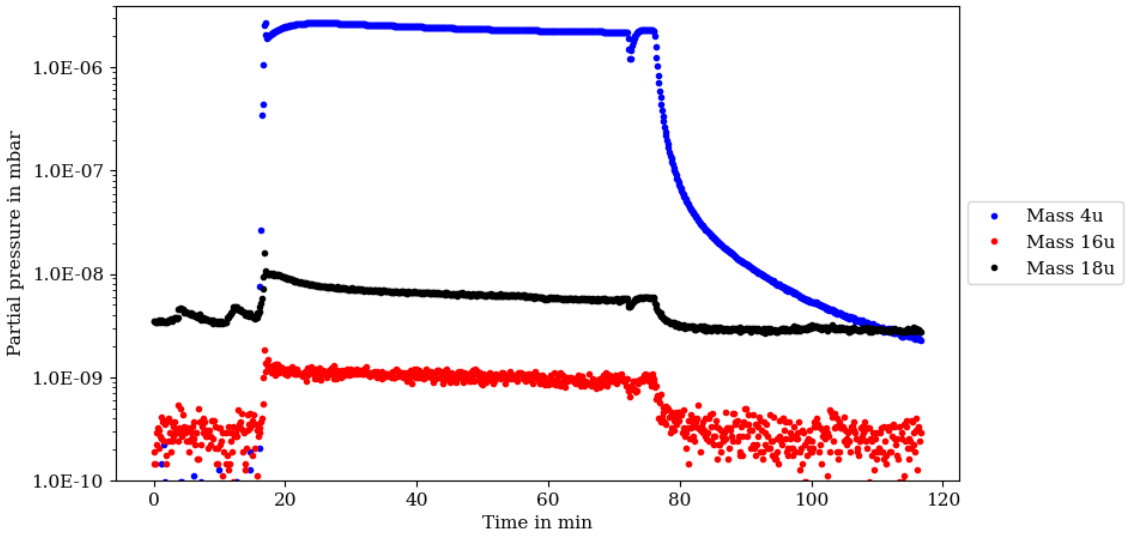

Figure 7.2.: Deuterium only injection at 30 K cold trap temperature. The deuterium is represented by the 4 u (blue), methane by the 16 u (red), and the water background by the 18 u (black) pressure reading. The 16 u pressure reading is in agreement with the water composition for the displayed 18 u pressure, no methane is visible in the system.

pure 100 $\mathrm{sccm}_{\mathrm{H_2}}$ deuterium injection in the 30 K cold trap is shown in figure 7.2 with CV 2 and CV 3 fully opened. The pressure for the 4 u reading is in the expected order of 10^{-6} mbar as determined in section 7.2 for the given gas split and injection when deuterium is not pumped. The pressure peak at 17 min indicates the start of the deuterium injection. The deuterium pressure has a slight decrease, which can be neglected. The kink at the end of the measurement at 72 min is the result of the decoupling of the main deuterium source from the 4 ℓ buffer vessel before the injection is stopped after 76 min.

The background shown by 16 u and 18 u readings indicates a reaction in the water background due to changes in the deuterium flow. A scan for all methane species according to the methane composition given in table (7.1) with an error margin of 10 % per species is negative over the test period. Hence, it is not possible to identify methane in the gas flow.

The background of 16 u and 18 u pressure readings in low 10^{-9} mbar to 10^{-8} mbar regions correlates in some 30 K measurements with the D_2 pressure of the systems (see section 7.3.3).

7.3.2. Methane injection

The measurement is executed with closed CV 3 in order to maximize the methane sensitivity leading to the result shown in figure 7.3. The methane injection starts after 50 s and is indicated by the rise of the 4 u background. Its origin is the degassing of deuterium by the upstream buffer vessel from previous measurements, indicating that deuterium is not reduced by the 30 K cold trap. The constant 16 u reading correlate with the constant 18 u readings signaling a water background caused by the downstream part of the cold trap installations. The RGA spectrum shows a clear water spectrum with a small amount of other gas species at its sensitivity threshold in figure D.8. The established upstream methane flow is in the magnitude of 10^{-4} mbar $\ell\,\mathrm{s}^{-1}$. This would lead to a noticeable RGA reading of 16 u, assuming that approximately 44 % of the flow is 16 u in table (7.1).

The amount of released methane pV is calculated by the pressure drop during injection from 637.84 mbar to 636.35 mbar recorded by VG 2, with the Gaussian propagation of

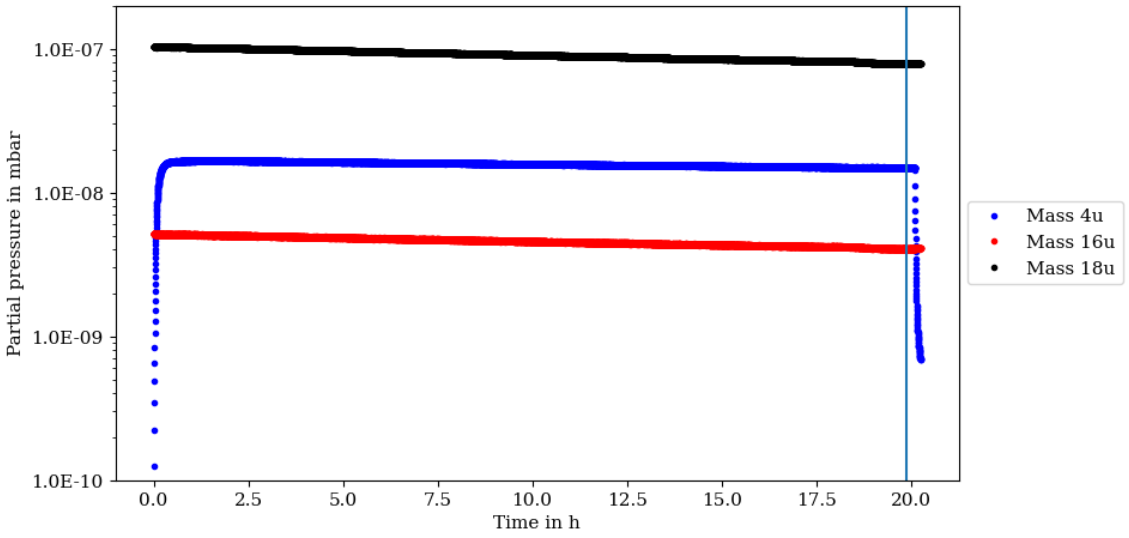

Figure 7.3.: Methane injection at 30 K cold trap temperature. The deuterium background (4 u (blue)) is due to the out-gassing of the installations upstream of the cold trap. The methane is represented by the 16 u (red), and water by the 18 u (black) pressure reading. The 16 u pressure is in agreement with the water composition for the displayed 18 u pressure, no methane is visible in the system. The blue line after 20 h marks the position of the spectrum which is in the best agreement[2] to the methane composition in table 7.1, shown in figure D.8.

uncertainty, the uncertainty of the installed pressure gauge of 0.08 % and the volume $\Delta V = 0.046\,\ell$:

$$\begin{aligned} pV = \Delta p \cdot V &= 1.49\,\text{mbar} \cdot 15.863\,\ell \\ &= (23.64 \pm 11.47)\,\text{mbar}\,\ell\ . \end{aligned} \tag{7.4}$$

The median methane flow can be determined accordingly with the duration of the methane injection of approximate 19.18 h and the Gaussian propagation with $\Delta t = 1\,\text{min}$:

$$\begin{aligned} \overline{\phi}^{\text{CH}_4}_{\text{vessel}} &= \frac{23.64\,\text{mbar}\,\ell}{19.18\,\text{h}} \\ &= (3.4 \pm 1.7) \times 10^{-4}\,\text{mbar}\,\ell\,\text{s}^{-1}\ . \end{aligned} \tag{7.5}$$

Assuming that 16 u makes up $\chi = 44\,\%$ of the total methane flow and it is not pumped, the 16 u RGA pressures reading should be:

$$\begin{aligned} p^{\text{max}}_{\text{RGA}_{16\text{u}}} &= \frac{\overline{\phi}^{\text{CH}_4}_{\text{vessel}}}{S_{\text{CH}_4}} \cdot \chi \cdot K_{\text{CH}_4} \\ &= (3.1 \pm 1.6) \times 10^{-6}\,\text{mbar}\ . \end{aligned} \tag{7.6}$$

The uncertainty is given by the Gaussian propagation, $\Delta S = 10\,\%$ and the error in the methane distribution $\Delta\chi = 1.8\,\%$.

The 16 u pressure reading have a magnitude of 10^{-9} mbar as shown in figure 7.3. This is well below the expected 10^{-6} mbar for the given flow and setup configuration. Hence, the measurement indicates that the methane flow is reduced by at least three orders of magnitudes.

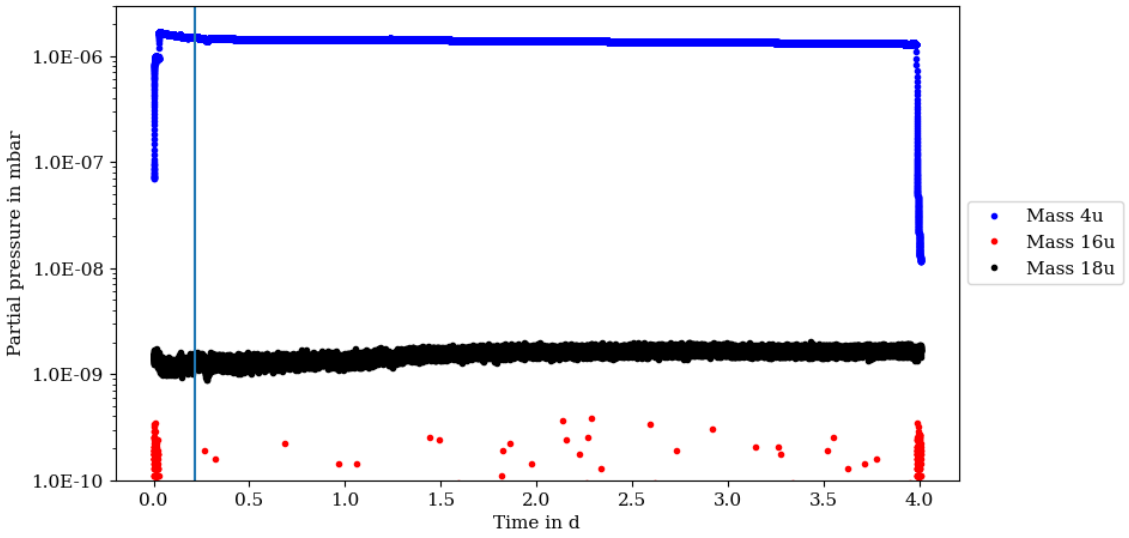

Figure 7.4.: Deuterium-methane injection at 30 K cold trap temperature. The constant deuterium injection with 100 $\mathrm{sccm_{H_2}}$ is represented by the 4 u (blue), methane by the 16 u (red), and water by the 18 u (black) pressure reading. The 16 u pressure is in agreement with the water composition for the 18 u pressure reading, no methane is visible in the system. The blue line after 0.2 d marks the position of the spectrum which is in the best agreement[2] to the methane composition in table 7.1, shown in figure D.9.

7.3.3. Deuterium-methane mixture injection

The measurement for a deuterium-methane flow at a cold trap temperature of 30 K is shown in figure 7.4.

A higher 16 u background is visible at the start (course is shown in figure E.14, spectrum in figure D.11) and the end (course shown in figure E.15, spectrum in figure D.12) of the measurement. This seems to correlate with the overall pressure at the RGA, monitored at the pumping station. The spectrum does not indicate that the readings correlate with the injected methane flow. The 4 u pressure drop at the end marks the decoupling of the installations upstream the cold trap and therefore the stop of the deuterium and methane injection. A scan for the methane fingerprint within an error margin of 10 % is negative during the measurement period. Hence, it is not possible to identify methane in the gas flow. The measured partial pressure is at the threshold of sensitivity of the RGA in Faraday mode.

The amount of injected methane can be calculated by the pressure drop from 551.60 mbar to 551.06 mbar in the methane buffer vessel:

$$pV = (8.6 \pm 9.9)\,\mathrm{mbar}\,\ell\ . \tag{7.7}$$

The methane is injected over a time period of 3.96 d. Hence, a median methane flow can be calculated to:

$$\overline{\phi}_{\mathrm{CH_4}} = (2.5 \pm 2.9) \times 10^{-5}\,\mathrm{mbar}\,\ell\,\mathrm{s}^{-1}\ . \tag{7.8}$$

Despite the high uncertainty in the flow, methane injection into the cold trap can be assured because the pressure upstream of the aperture of the injection system (displayed in figure 5.5) including the buffer vessel with its approximately 500 mbar, was larger than the pressure downstream the aperture.

In this measurement, the split between the RGA and the main vacuum pump downstream CV 3 is adjusted to higher sensitivity at the RGA. The tested ratio in section 7.2 is changed

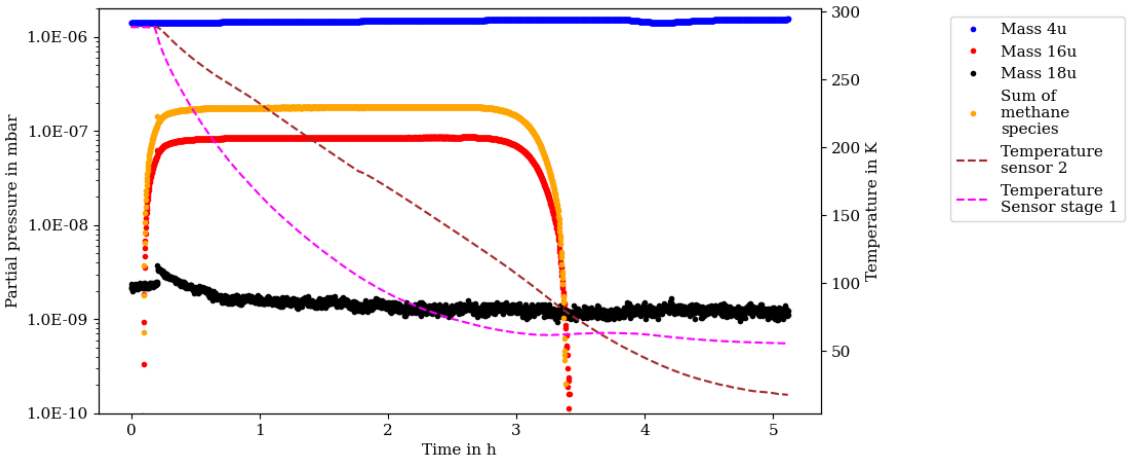

Figure 7.5.: Cool-down behavior of the cold trap. A constant deuterium 100 $\mathrm{sccm}_{\mathrm{H_2}}$ (4 u (blue)) and methane $\approx 4 \times 10^{-2}\,\mathrm{mbar}\,\ell\,\mathrm{s}^{-1}$ (16 u (red) and sum over the methane species (orange)) mixture injection is shown during cooling down of the cold trap from 300 K to 20 K. The water background is represented by the 18 u (black) pressure reading. The temperature of the cold trap are displayed by the thermal sensors 2 (coldest sensor) and cold head temperature sensor stage 1 (dashed lines).

when CV2 and CV 3 are fully opened. The deuterium pressure drops from 1.6×10^{-6} mbar to 9.9×10^{-7} mbar with the new setting.

The expected methane pressure at the RGA with a stabilized deuterium pressure of $p_{\mathrm{D_2}} = 1.42 \times 10^{-6}$ mbar for a deuterium flow of $\overline{\phi}_{\mathrm{D_2}} = 1.18\,\mathrm{mbar}\,\ell\,\mathrm{s}^{-1}$ is calculated to:

$$\begin{aligned} p_{\mathrm{RGA_{16u}}} &= \frac{\frac{\overline{\phi}_{\mathrm{CH_4}} \cdot \chi}{S_{\mathrm{CH_4}}} \cdot K_{\mathrm{CH_4}}}{\frac{\overline{\phi}_{\mathrm{D_2}}}{S_{\mathrm{D_2}}} \cdot K_{\mathrm{D_2}}} \cdot p_{\mathrm{D_2}} \\ &= (4.94 \pm 0.39) \times 10^{-10}\,\mathrm{mbar}\,. \end{aligned} \tag{7.9}$$

The uncertainty is given by the Gaussian propagation. A direct methane identification is not possible with the given setup as the result is below the RGA sensitivity. In section 7.5, the released gas during the regeneration will be analyzed to additionally verify the calculated values for the injected methane.

7.4. Temperature-dependent reduction

In order to determine the gas flow behavior at a wide-temperature range, the gas flow during a cool-down of the cold trap is monitored. The location of the temperature sensors is displayed in figure 5.1. The temperature readings of the four installed senors differ from each other due to the thermal inertia of the system and location of the sensors. The cold trap is cooled only at the head (see figure 5.4) leading to a faster cool-down of temperature sensors 1 and 2 which are close to the cold head. Sensors 3 and 4 are on the opposite side of the cold trap injection- and exhaust-pipe and cool-down slower but heat up faster. In order to pump gas, the lowest temperature is relevant (sensor 2) while stage 1 indicates the temperature of the cryocooler head. The temperature of stage 1 reaches its minimum at aproximatly 3 h, while sensor 2 reaches the minimum at aproximatly 5 h as shown in figure 7.5. Therefore, the temperature reading of stage 1 is an indication of the thermal inertia of the system as well as for the cooling power. The cold trap temperature ranges

from approximately 290 K at the start of the measurement to 20 K at the end. The partial pressures of 4 u (deuterium), 16 u (methane), and 18 u (water background) are shown in figure 7.5, with the deuterium flow set to $100\,\mathrm{sccm}_{\mathrm{H_2}}$. The peak in the water background can be explained by impurities in the methane mixture originating from the installations of the methane injection system. In the tested temperature range, the deuterium flow is not affected by the temperature of the cold trap. The water background is noticeably higher at the start of the measurement ($\approx 2 \times 10^{-9}$ mbar) than at the end ($\approx 10^{-9}$ mbar), its reduction starts at a cold trap temperature of approximately 250 K.

With the partial pressure readings from the RGA and the pumping speed of the installed TMP, the methane flow is calculated to:

$$\begin{aligned} \phi_{\mathrm{CH_4}} &= \phi_{\mathrm{D_2}} \cdot \left(\frac{p^{\mathrm{RGA}}_{\mathrm{CH_4}} \cdot S_{\mathrm{CH_4}}}{K_{\mathrm{CH_4}}} \cdot \frac{K_{\mathrm{D_2}}}{p^{\mathrm{RGA}}_{\mathrm{D_2}} \cdot S_{\mathrm{D_2}}} \right) \\ &= (4.19 \pm 1.03) \times 10^{-2}\,\mathrm{mbar}\,\ell\,\mathrm{s}^{-1}\ . \end{aligned} \tag{7.10}$$

$p^{\mathrm{RGA}}_{\mathrm{CH_4}} = 1.76 \times 10^{-7}$ mbar is the sum of the pressure reading of the methane species, and $p^{\mathrm{RGA}}_{\mathrm{D_2}} = 1.43 \times 10^{-6}$ mbar the pressure of the 4 u reading representing deuterium.

The methane reading starts to decline at approximately 2.8 h at a minimum cold trap temperature of 122 K. It reaches the RGA sensitivity threshold at 3.4 h at a minimum cold trap temperature of 77 K.

A lower limit for the reduction factor ξ of methane can be determined using the reading of the 16 u pressure gas species $p^{\mathrm{RGA}}_{16\,\mathrm{u}} = 8.48 \times 10^{-8}$ mbar, and the RGA treshold of 10^{-10} mbar:

$$\begin{aligned} \xi_{\mathrm{min}} &= \frac{8.48 \times 10^{-7}\,\mathrm{mbar}}{10^{-10}\,\mathrm{mbar}} \\ &= 848\ . \end{aligned} \tag{7.11}$$

The data indicates that the cold trap starts filtering methane at a temperature of 120 K. It has to be taken into account that the corresponding cold head temperature is approximately 68 K which is in the temperature range where methane starts to depump (section 7.5). An effective methane reduction is given when the entire cold trap inner surface reaches the needed temperature. This is based on these measurements given at a temperature reading of 77 K. The measurements in section 7.5 show that methane can be released at 80 K. Considering the thermal inertia, it can be assumed that part of the cold trap inner surface is below the reading of the sensor with the lowest temperature. The lower limit for methane reduction is in the order of three magnitudes (equation 7.11).

7.5. Regeneration measurement

The regeneration of the cold trap is used to restore the pumping capacity. In this work the process of regeneration is also used to confirm the pumping ability by measuring the methane released during the process.

Determination of the empty cold trap measurement system

In order to interpret the measurements of the cold trap, the characteristics of a “clean” system has to be determined. Therefore, the cold trap is warmed up to approximate room temperature and afterwards cooled down to 30 K for more than one day. This procedure is executed under high-vacuum conditions with running TMPs. The regenerated cold trap is decoupled (HV 10 closed) and heated to 85 K. This measurement is followed by opening

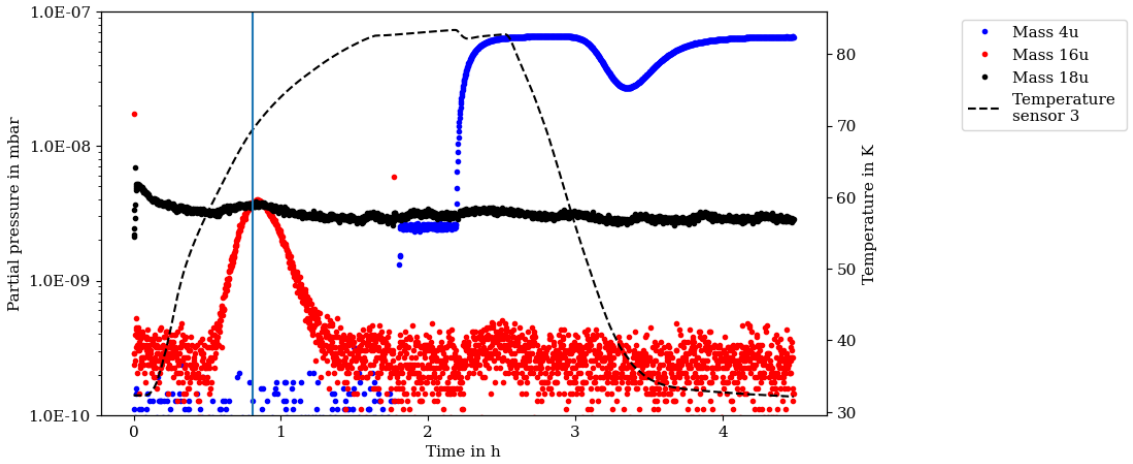

Figure 7.6.: Pressure evolution of a clean system during heating. The masses 4 u (blue), 16 u (red) and 18 u (black) indicate deuterium, methane, and water. The dashed line is the temperature of the cold trap represented by the warmest sensor reading (sensor 3), the blue line marks the position of the spectrum displayed in figure 7.7. From 1.8 h to 2.2 h, HV 5 and HV 6 are accidentally opened, which couple TMP 1 to the system.

HV 10 to couple the 4 ℓ vessel and the CH_4 injection system with closed LV 1 and HV 5. All measurements are executed with CV 3 closed, and CV 2 open.

The evolution of pressure during heating and cooling down is shown in figure 7.6 for the masses of 4 u, 16 u and 18 u.

The system has a permanent water background with a pressure of approximately 3×10^{-9} mbar represented by the 18 u reading (black). The heater power is increased to the target temperature of 80 K. A peak in 18 u pressure reading appears a few seconds after powering up the heaters while the recorded temperature is constant at approximately 30 K. This can be explained by thermal radiation which leads to a short initial loss of some water molecules. Besides this phenomenon, the 18 u pressure reading can be considered as constant. The 4 ℓ vessel is coupled to the system (HV 10 open) after approximately 1.8 h, no pressure change in 18 u is noticeable. This leads to the assumption that the water background is caused by the tubing and installations downstream of the cold trap.

The 16 u pressure reading (red) has a significant peak after approximately 0.8 h with a value of 4×10^{-9} mbar at a temperature of 65 K. The RGA mass spectrum from 1 u to 20 u (figure 7.7) does not match the expected fingerprint of the methane spectrum (table 7.1). The spectrum seems to be a mixture of different gases, as 16 u is present in water, oxygen, and methane. Oxygen, for example, has a similar saturation pressure curve to methane and is part of both water and carbon dioxide. The gases can be accumulated by the cold trap due to outgassing and leaking into the system. Furthermore, the components upstream of the system can outgas methane from previous measurements which get stored in the cold trap during the cool-down period. Besides the peak from 0.5 h to 1.4 h, the measured values for 16 u are at the RGA sensitivity threshold with values in the middle and lower 10^{-10} mbar range and are therefore not accessible for further investigations.

The deuterium background, which is represented by the 4 u reading, only appears when the HV 10 is opened and the background upstream the cold trap becomes visible to the RGA.

A drop in the deuterium reading can be recognized during the cool-down period from approximately 3 h to 4 h which corresponds to a temperature range from 55 K to 32 K. The origin of this phenomenon is unknown, the only variable in the system at this time period is the decrease in temperature (ramping down of the heater power). After dropping

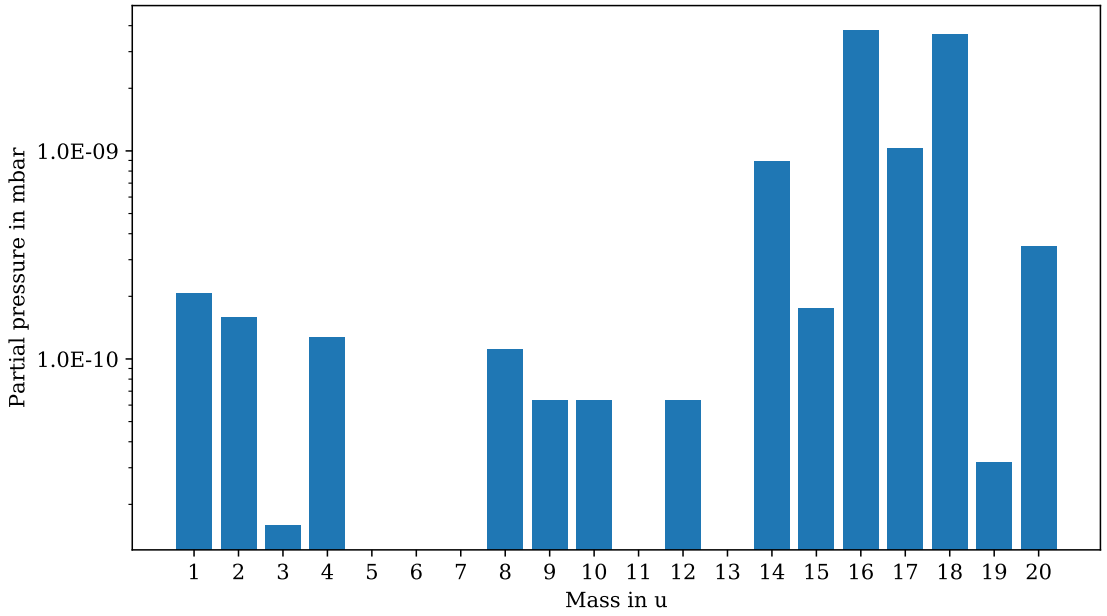

Figure 7.7.: Spectrum of a clean system during heating. The spectrum extracted from figure 7.6 is diplayed. The spectrum shows a water background with a large 16 u peak. No methane matching the composition in table 7.1 can be recognized.

from 7×10^{-8} mbar to 3×10^{-8} mbar, the pressure stabilizes at the previous 7×10^{-8} mbar level.

This measurement shows that an empty cold trap has no evidence for releasing methane during the regeneration to a temperature of approximately 80 K. The short peak in the 16 u reading can be explained by accumulated gas in the cold trap, which originates from the outgassing of the components upstream of the cold trap.

Heating of the loaded cold trap

The methane reduction function of the cold trap during the test in section 7.3.3 is verified by comparing the released methane during heating to the previously injected methane.

RGA readings of the loaded cold trap (section 7.3.3) are shown in figure 7.8. The measurement is performed with closed CV 3 and decoupled upstream installations (HV 10 closed).

At the beginning of the test, a deuterium background (blue) in the magnitude of 10^{-7} mbar is still present from the previous reduction measurement. It drops after approximately 2.8 h to the expected pressure in the magnitude of 10^{-10} mbar.

The 18 u reading represents the water background, which reacts in low magnitude to the cold trap temperature, with the expected pressure level in the magnitude of 10^{-9} mbar. A deuterium peak is visible after approximately 0.7 h. The reaction of water and deuterium to the heating of the cold trap is below the saturation pressure temperature. This can be explained by heat radiation with the evaporation of the methane molecules as a side effect.

The integration of the methane masses, which fit the composition in table 7.1, is calculated by:

$$pV = \frac{\sum_i p_i \cdot \mathrm{d}t}{K_{\mathrm{CH_4}}} \cdot S_{\mathrm{CH_4}} \ , \tag{7.12}$$

where i is the number of iterations, $\mathrm{d}t$ the duration of the measurement, and p_i the pressure sum of the methane species by the RGA at the given iteration. Methane was present in this

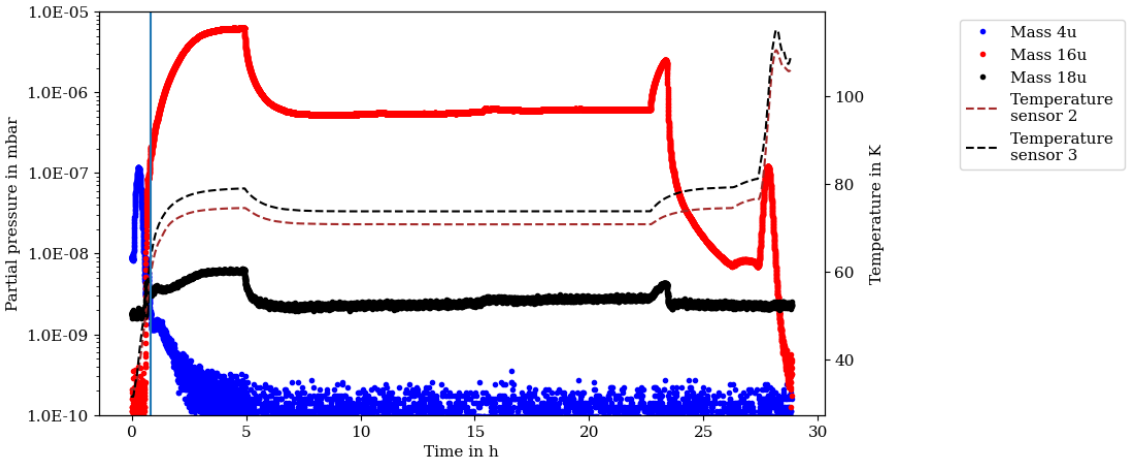

Figure 7.8.: Heating loaded cold trap. The masses 4 u (blue), 16 u (red) and 18 u (black) indicate deuterium, methane, and water during cold trap regeneration. The cold trap temperature is represented by the temperature sensor reading of sensor 2 (coldest) and sensor 3 (warmest) (dashed lines). The blue line marks the position of the spectrum which is in the best agreement[2] to the methane composition in table 7.1 shown in figure D.10.

measurement for 27.23 h. For a negligible error of $\Delta dt = 0$ recorded by the RGA software is $\sum_i p_i \cdot dt = x$, and $\Delta x = 10\,\%$ the uncertainty in the pressure of the RGA. Hence, with the Gaussian propagation of uncertainty, the total pV amount is:

$$pV = (10.6 \pm 1.6)\,\mathrm{mbar}\,\ell\,. \tag{7.13}$$

This result is well within the amount of stored methane calculated in equation (7.7) of $(8.6 \pm 9.9)\,\mathrm{mbar}\,\ell$. It shows that the cold trap has pumped the methane in the previous measurement and is therefore operational.

7.6. Summary

In this chapter, the characteristics of the cold trap regarding the ability to pump methane were determined. With a measurement at room temperature, it was shown that the setup is able to detect methane in a deuterium-methane mixture that is injected into the cold trap. The background of a system under flow conditions at a cold trap temperature of 30 K was analyzed with an injection of only deuterium and only methane. With the findings of the background it was possible to interpret the measurements. A reduction measurement was performed at 30 K with an injection of a deuterium-methane mixture, the result of this measurement was backed up by the analysis of the gas released during regeneration. Furthermore, the behavior of the cold trap during cooling was analyzed and the reduction factor was determined to at least three orders of magnitude.

The executed tests show that the stored amount of methane during the test period matches the released amount of methane. The calculated methane flow of the long-term measurements are mean values over the pressure of the methane buffer vessel. The comparison of stored and released methane and the investigation of the cool-down behavior of the cold trap lead to the conclusion that the cold trap is operational within the given parameters.

8. Conclusions

The KATRIN experiment aims to determine the effective electron neutrino mass by investigating the endpoint region of the β-decay spectrum of molecular tritium. In order to achieve a sensitivity of 0.2 eV, one major requirement is a stable tritium circulation on the 0.1 % level.

In the first full tritium measurement in spring 2019, a decrease in the tritium throughput over the WGTS was discovered which affected the stability of the tritium source. The decrease was caused by methane impurities in the gas freezing out at part of the 30 K cold injection capillary, which caused a change in conductance and therefore gas flow. Tritium can produce tritiated methane by radio-chemical reactions in the presence of stainless steel, which the WGTS and the LOOP system are primarily made of. In order to remove these methane impurities, the cold trap tested in this thesis was commissioned with non-radioactive gases.

First, the conductance of the cold trap was determined for different gases in a range from molecular flow conditions up to the edge of contentious flow conditions and for different temperatures. An analytical determination is not possible due to the complex geometry of the cold trap. Therefore, a simulation for molecular flow conditions was made in order to verify the measurement results. It shows that the measured values agree with the simulation results. The conductance for different temperatures was measured by using helium. The measured values were compared with theoretical conductance values based on different theories for the viscosity calculation. These calculations indicate a significant temperature gradient for the gas flow.

The methane reduction was tested by analyzing the exhaust gas of the cold trap using a RGA. Different gas mixtures of deuterium and methane were used to test the reduction capabilities of the cold trap. In order to get an overview of the temperature behavior of the cold trap, tests with different cold trap temperatures were performed. During the measurements with a 30 K cold trap, it was not possible to detect any methane leaving the cold trap. This leads to the conclusion that the cold trap reduces methane in a deuterium-methane flow of approximately 1 mbar $\ell\,s^{-1}$ by a factor of at least three orders of magnitude. Furthermore, it was found that the cold trap can be regenerated at a temperature of approximately 80 K. During the regeneration, the released amount of methane matched the injected amount. This confirms the conclusion of the determined lower limit for the reduction factor.

As a result of the measurements, it can be confirmed that the cold trap is capable to reduce methane impurities by a significant factor from a deuterium-methane gas flow. Theoretical considerations suggest that neither the pumping speed nor the conductance are significantly influenced in a realistic time frame of operation. Therefore, the cold trap fulfills its design requirements.

Later measurements at KATRIN shows that methane production reached saturation. Therefore, it is not necessary to install the cold trap in the LOOP system. The tested cold

trap can also be used in different applications outside the LOOP system of KATRIN. In the configuration used in this thesis, the cold trap has proven its capabilities as a stand-alone system. Due to the wide-temperature range in which it can be operated, this configuration can be used as a gas purifier for a variety of gases, e.g. test setups for the DARWIN experiment. The storage capacity of the system also qualifies the cold trap for this case. In conclusion, the cold trap is fully characterized in the scope of the thesis enabling an easy installation for any requested applications.

Appendix

A. Constants

Stefan-Bolzmann constant $\sigma = 5.678 \times 10^{-8}\,\mathrm{WK^{-4}m^{-2}}$

Universal gas constant $R = 8.314\,\mathrm{J\,K^{-1}\,mol^{-1}}$

Boltzman constant $k_B = 1.380\,649 \times 10^{-23}\,\mathrm{J\,K^{-1}}$

Rydberg constant $R_H = 10\,973\,731.568\,160\,\mathrm{m^{-1}}$

Avogadro constant $N_A = 6.022\,140\,76 \times 10^{23}\,\mathrm{mol^{-1}}$

B. Pumping speed of HiPace 80

Table B.1.: Pumping speed HiPace 80. Pumping speeds are listed for different gases depending on the molecular weight for the HiPace 80 TMP [Pfe20].

Gas species	Mass in u	Pumping speed S in $\ell\,\mathrm{s^{-1}}$
H_2	2	48
He	4	58
N_2	28	67
Ar	40	66

C. Flow-conductance dependency plots

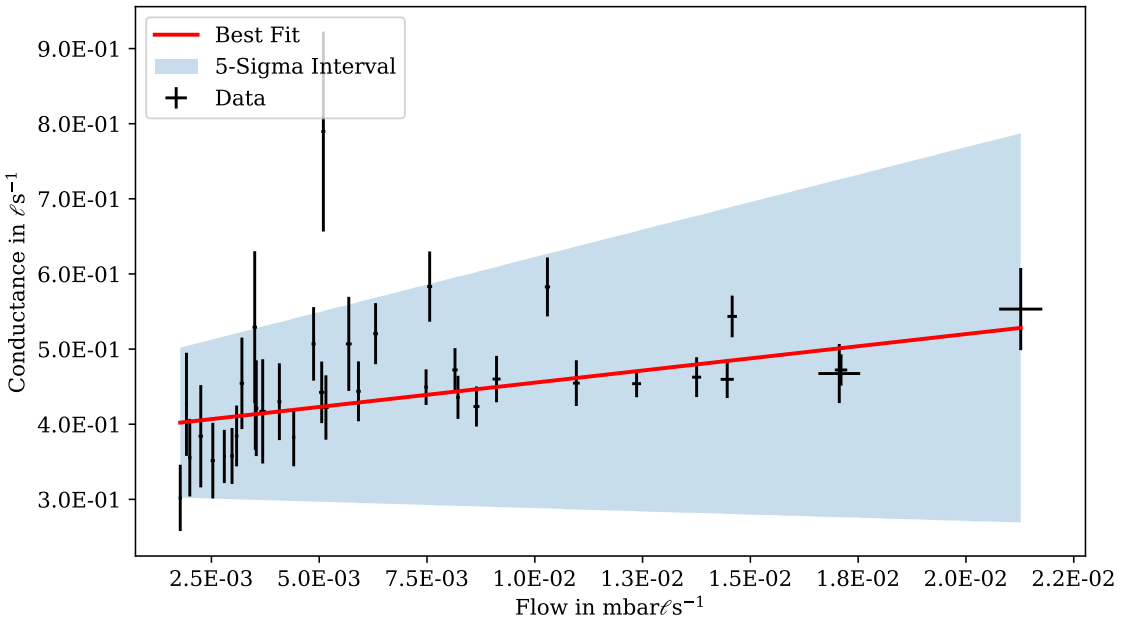

Figure C.1.: Flow-conductance dependency for cold trap with helium gas at room temperature. The displayed conductance values are on the edge of a molecular flow regime. The data is fitted with a linear orthogonal distance regression, the error bars are used as a weight.

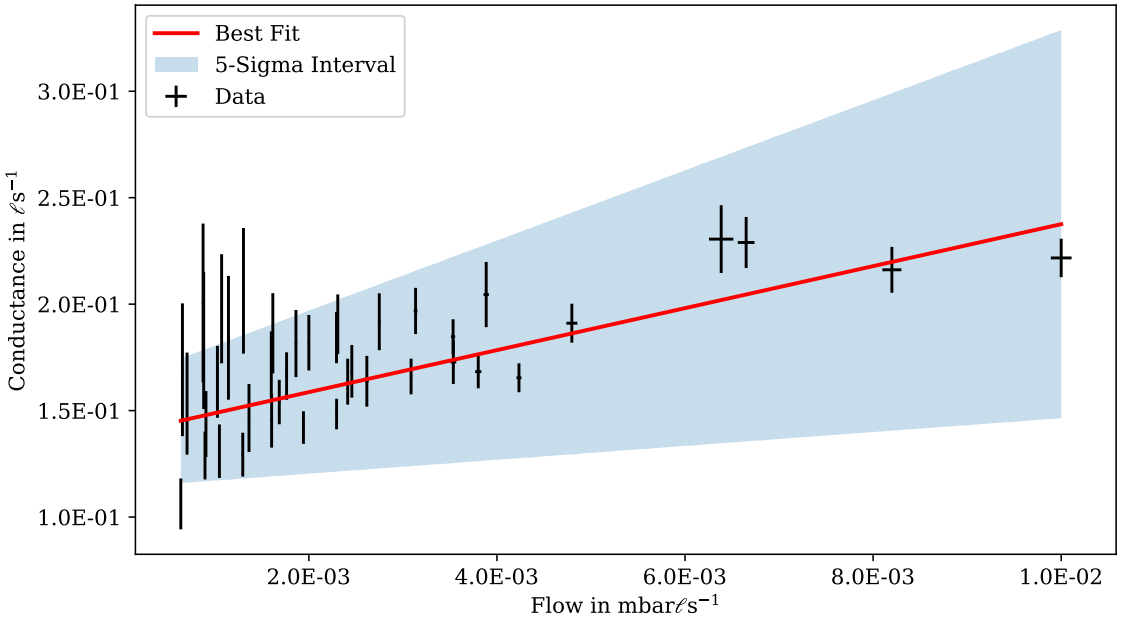

Figure C.2.: Flow-conductance dependency for cold trap with argon gas at room temperature. The displayed conductance values are on the edge of a molecular flow regime. The data is fitted with a linear orthogonal distance regression, the error bars are used as a weight.

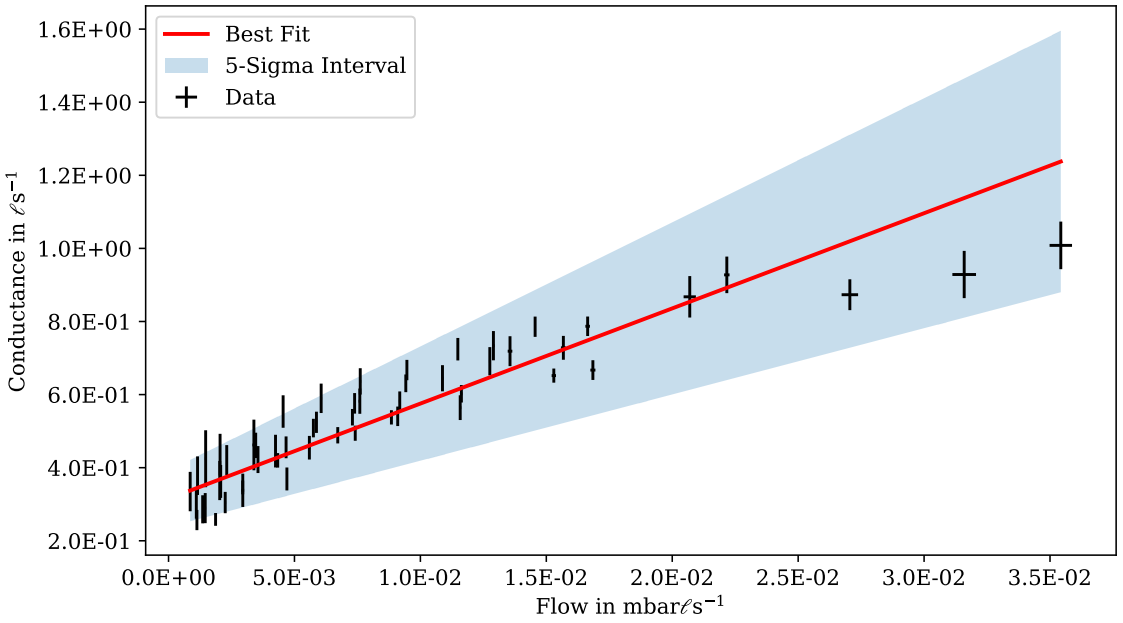

Figure C.3.: Flow-conductance dependency for cold trap with helium gas at 80 K. The displayed conductance values are on the edge of a molecular flow regime. The data is fitted with a linear orthogonal distance regression, the error bars are used as a weight.

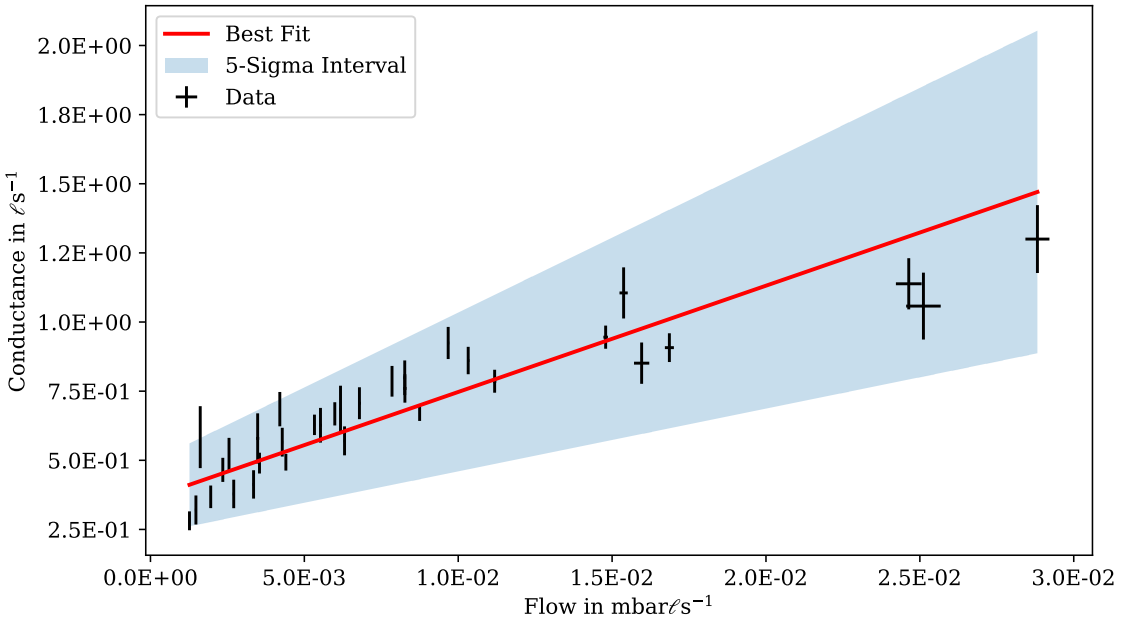

Figure C.4.: Flow-conductance dependency for cold trap with helium gas at 30 K. The displayed conductance values are on the edge of a molecular flow regime. The data is fitted with a linear orthogonal distance regression, the error bars are used as a weight.

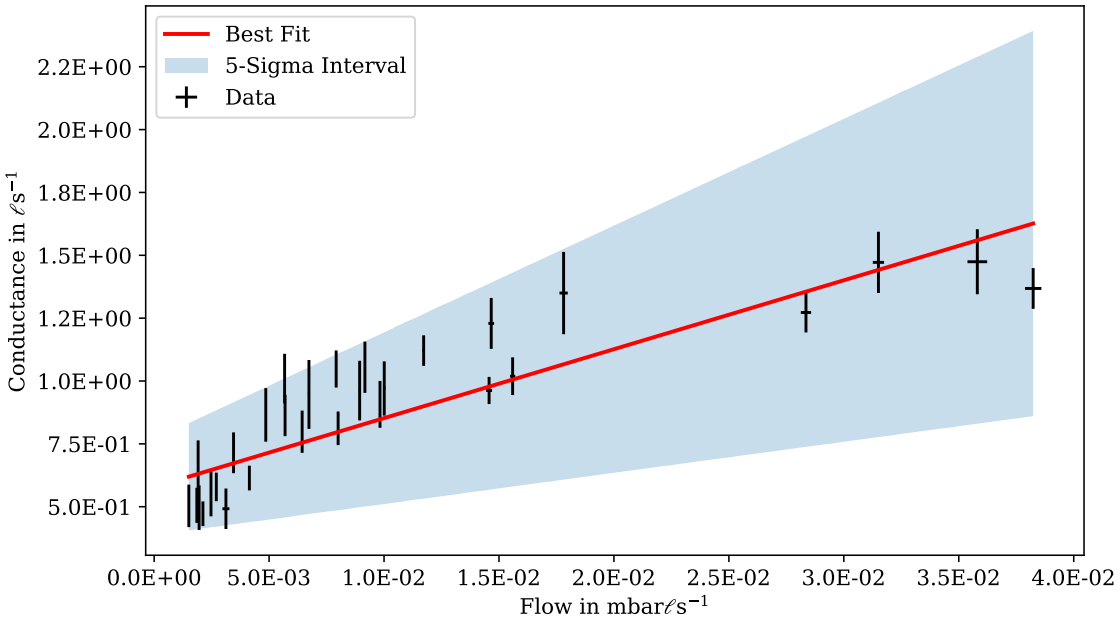

Figure C.5.: Flow-conductance dependency for cold trap with helium gas at 5 K. The displayed conductance values are on the edge of a molecular flow regime. The data is fitted with a linear orthogonal distance regression, the error bars are used as a weight.

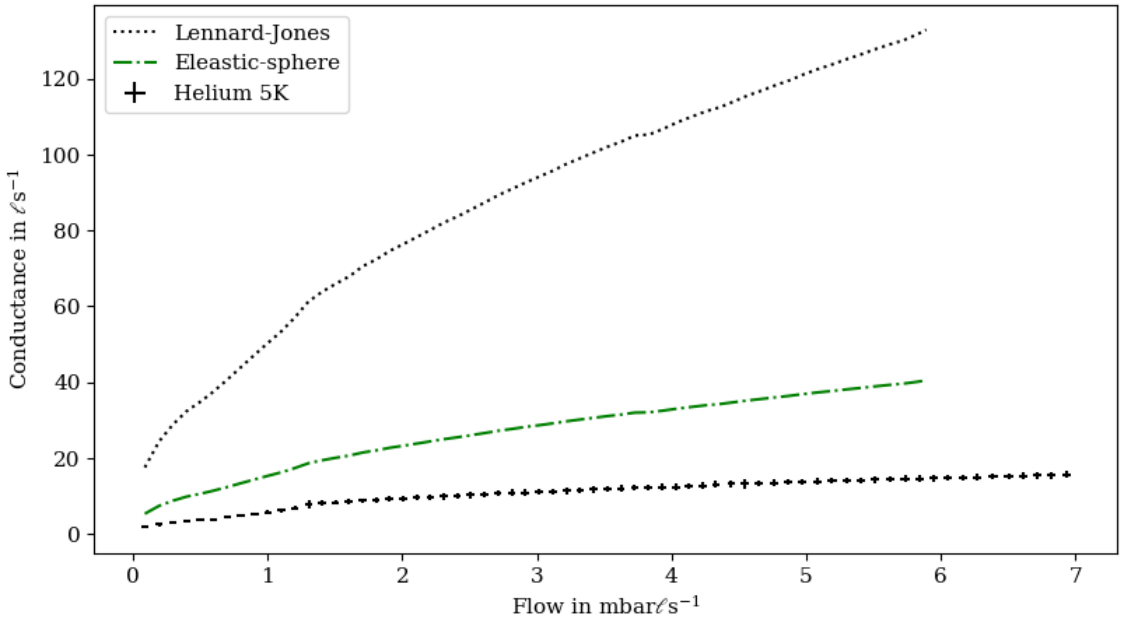

Figure C.6.: Theoretical cold trap conductivity for helium at 5 K. The theoretical conductance values are calculated using the elastic-sphere kinetic (green dash-dotted line) and Lennard-Jones (black dotted line) model. The measured values for helium at a cold trap temperature of 5 K are plotted in black.

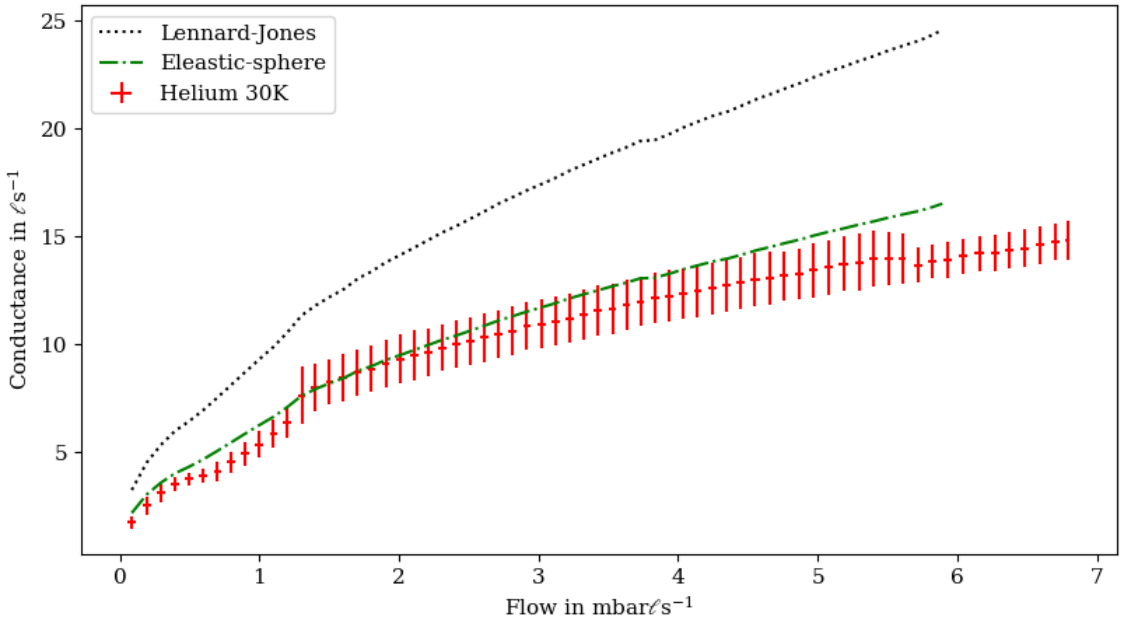

Figure C.7.: Theoretical cold trap conductivity for helium at 30 K**.** Theoretical conductance values are calculated using the elastic-sphere kinetic (green dash-dotted line) and Lennard-Jones (black dotted line) model. The measured values for helium at a cold trap temperature of 30 K are plotted in red.

D. RGA spectra behind the cold trap

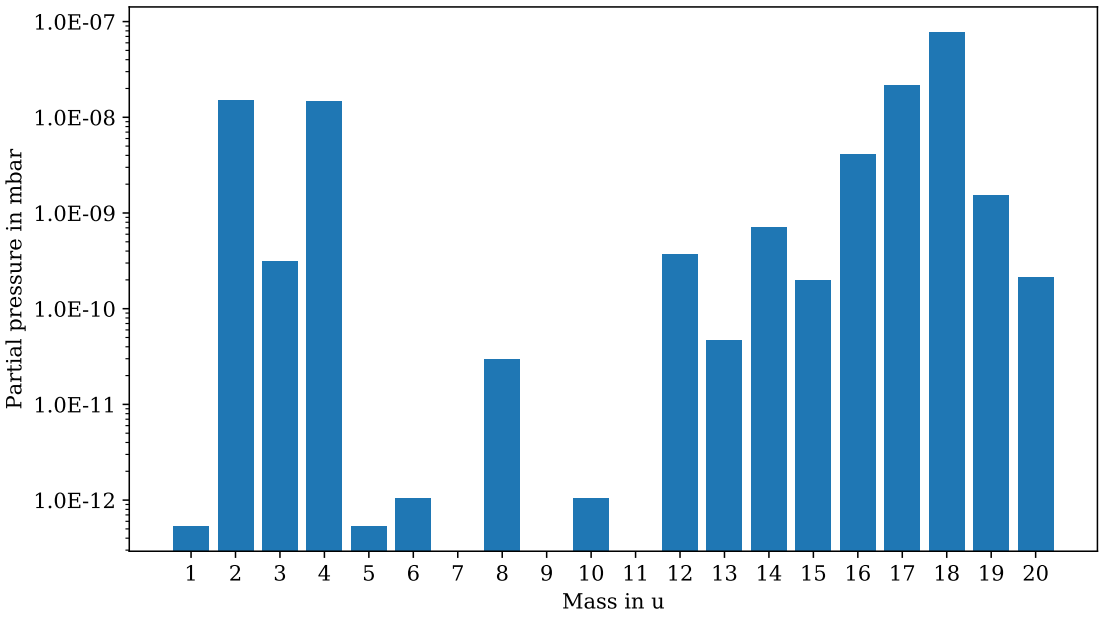

Figure D.8.: Spectrum of a methane only injection at 30 K cold trap temperature. The spectrum extracted from figure 7.3 is displayed. The water and deuterium background can be recognized, no methane is visible in this spectrum.

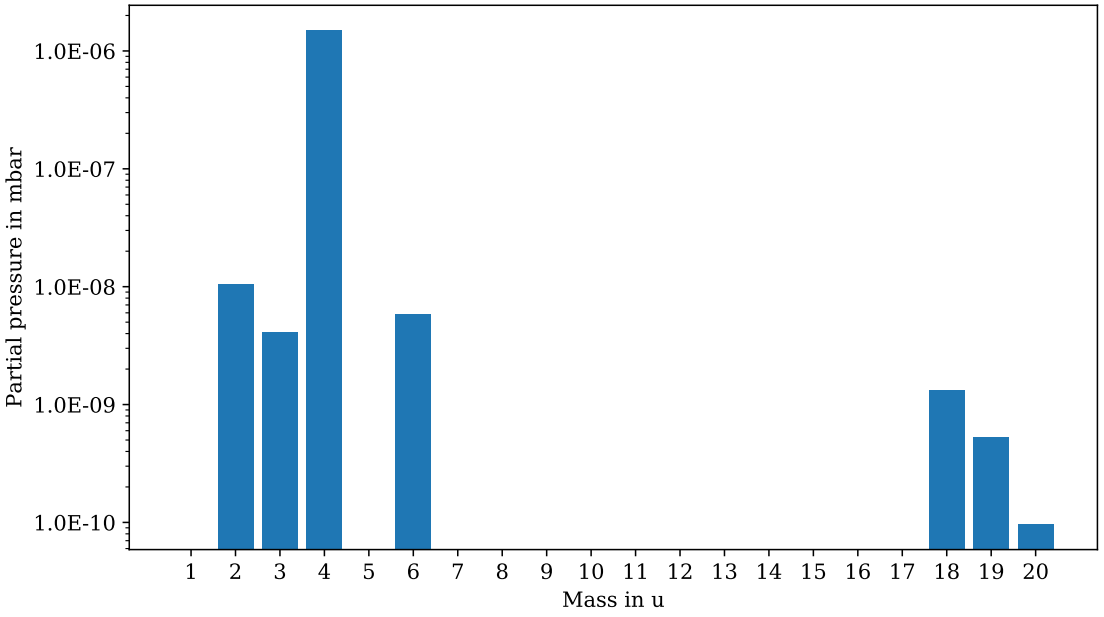

Figure D.9.: Spectrum of a deuterium-methane injection at 30 K cold trap temperature. The spectrum extracted from figure 7.4 is displayed. The pressure reading represents the deuterium injection is dominant, and the water background is visible.

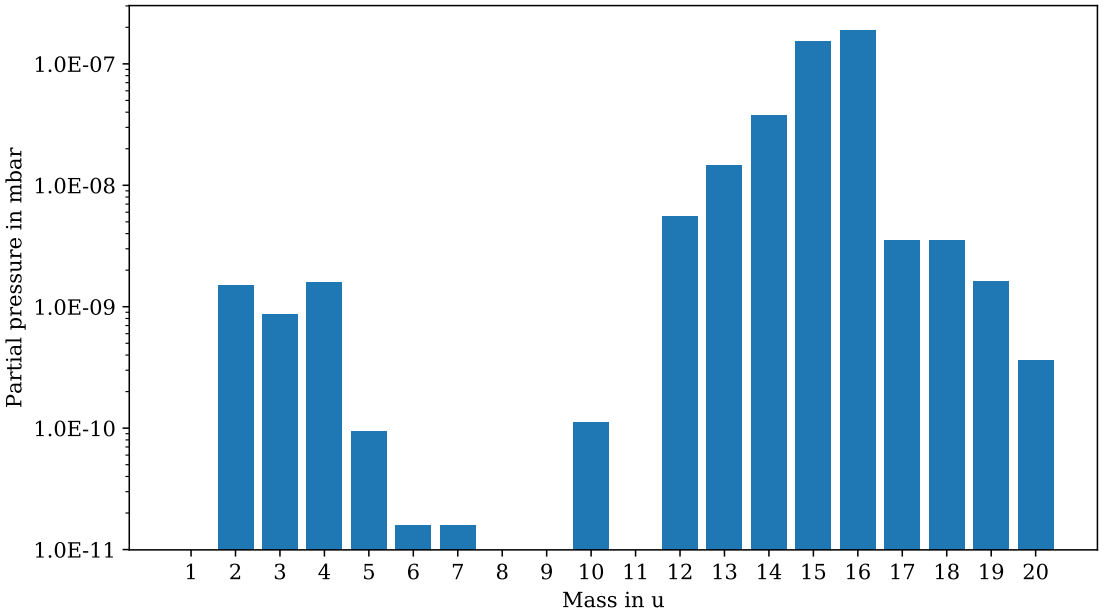

Figure D.10.: Spectrum of the loaded cold trap during regeneration. The spectrum extracted from figure 7.8 is displayed. A methane spectrum matching the composition in table 7.1 is visible. Water and deuterium backgrounds are present in this spectrum.

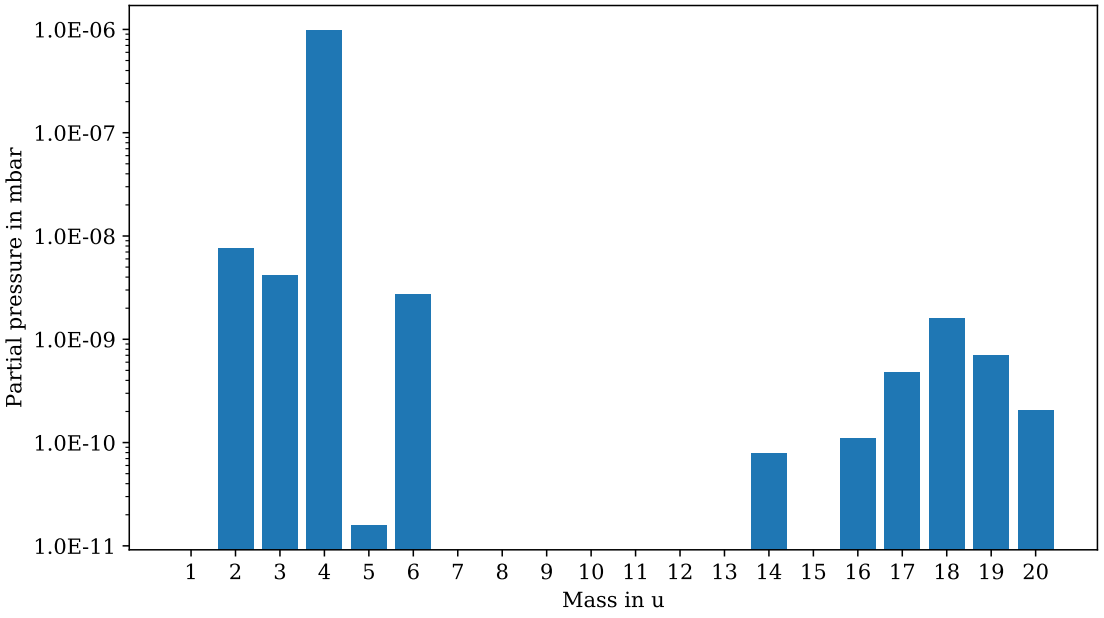

Figure D.11.: Spectrum of the 30 K cold trap at the beginning of a deuterium-methane injection. The spectrum is generated 16.67 min after starting the injection in figure 7.4. The water background and deuterium are noticeable, no methane matching the composition in table 7.1 can be recognized. The position, when the spectrum was recorded, is shown in figure E.14.

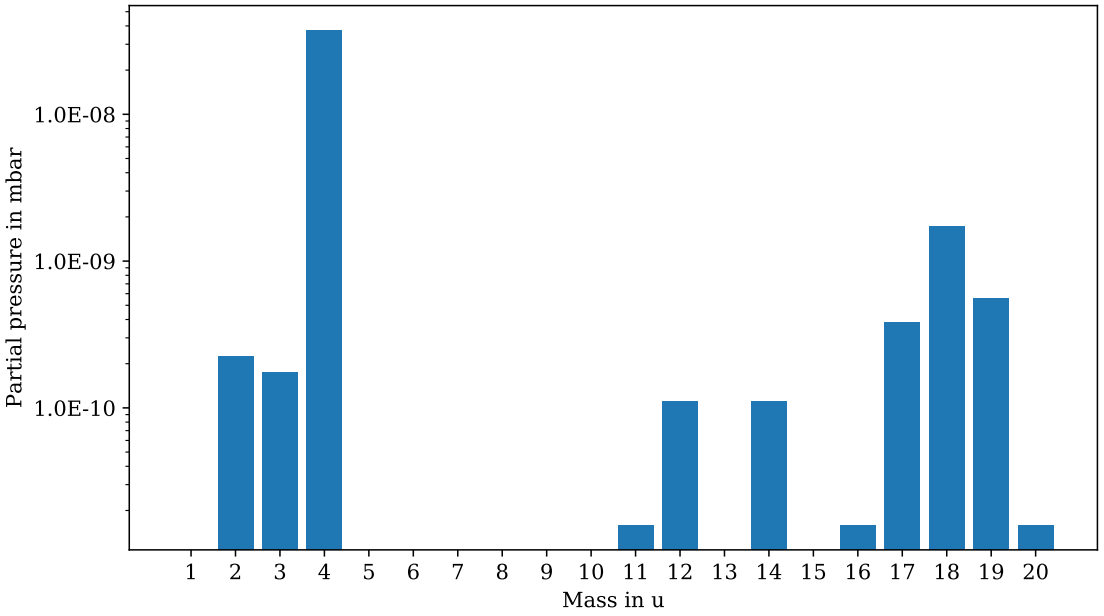

Figure D.12.: Spectrum of the 30 K cold trap at the end of a deuterium-methane injection. The spectrum is generated 3.99 d after starting the gas injection. The water background and deuterium are noticeable, no methane matching the composition in table 7.1 can be recognized. The position when the spectrum was recorded, is shown in figure E.15.

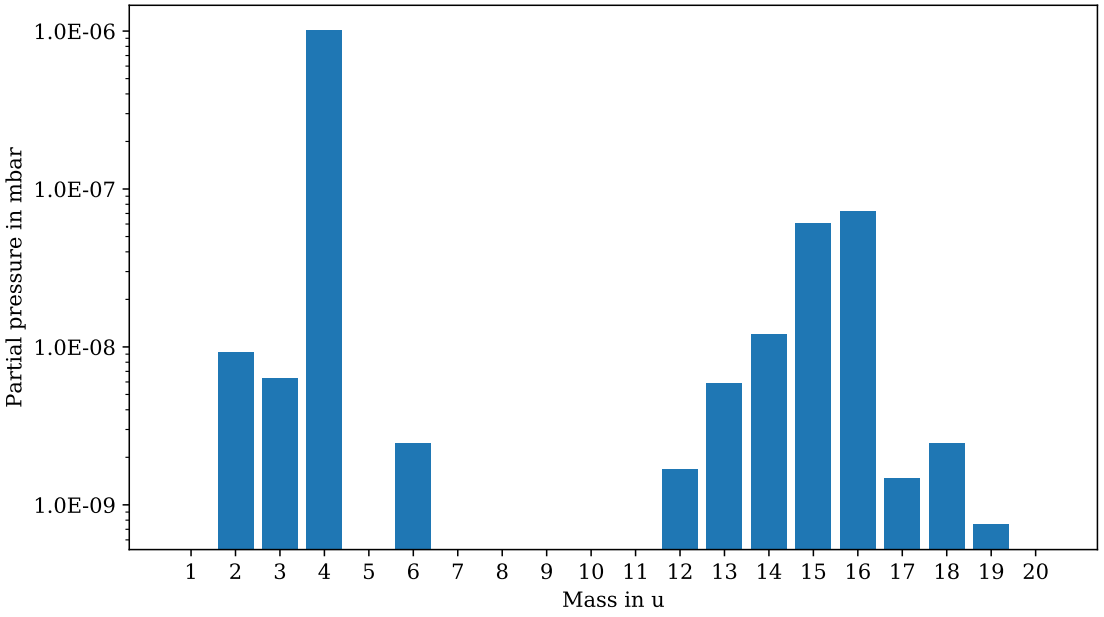

Figure D.13.: Spectrum of a deuterium-methane injection at 290 K cold trap temperature. The spectrum extracted from figure 7.1 is displayed. Deuterium and the methane composition (see table 7.1) as well as the water background are visible.

E. Additional plots

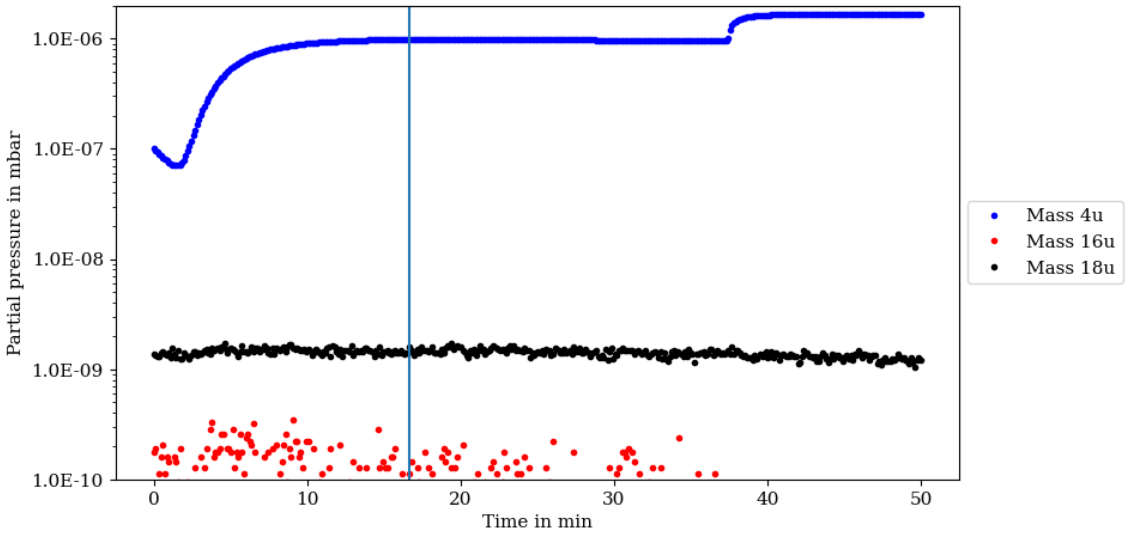

Figure E.14.: Begin of deuterium-methane injection at 30 K cold trap temperature. The first 50 min from the measurement in figure 7.4 are shown. The larger 16 u (red) background compared to the rest of the measurement is noticeable. The blue line marks the position of the spectrum shown in figure D.11.

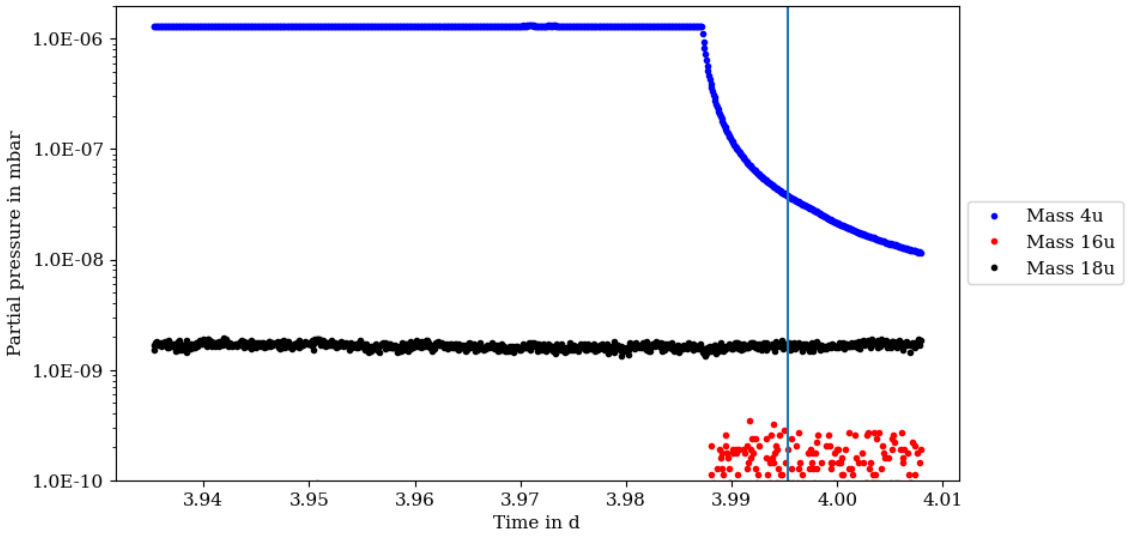

Figure E.15.: End of deuterium-methane injection at 30 K cold trap temperature. The last 17 min from the measurement in figure 7.4 are shown. After stopping the gas injection (indicated by the kink in the 4 u pressure reading in blue) the 16 u pressure reading becomes visible. The blue line marks the position of the spectrum shown in figure D.12.

Bibliography

[AAA+01] Q. R. Ahmad, R. C. Allen, T. C. Andersen, et al. Measurement of the Rate of $\nu_e + d \rightarrow p + p + e^-$ Interactions Produced by ^8B Solar Neutrinos at the Sudbury Neutrino Observatory. *Physical Review Letters*, 87:071301, Jul 2001. doi:10.1103/PhysRevLett.87.071301.

[AAA+12] Y. Abe, C. Aberle, T. Akiri, et al. Indication of Reactor $\overline{\nu}_e$ Disappearance in the Double Chooz Experiment. *Physical Review Letters*, 108:131801, Mar 2012. doi:10.1103/PhysRevLett.108.131801.

[AAA+19] M. Aker, K. Altenmüller, M. Arenz, et al. Improved Upper Limit on the Neutrino Mass from a Direct Kinematic Method by KATRIN. *Physical Review Letters*, 123(22), Nov 2019. doi:10.1103/physrevlett.123.221802.

[AAB05] J. Angrik, T. Armbrust, and A. Beglarian. KATRIN design report 2004. Technical report, Forschungszentrum, Karlsruhe, 2005. doi:10.5445/IR/270060419. 51.54.01; LK 01.

[ABB+12] F. P. An, J. Z. Bai, A. B. Balantekin, et al. Observation of Electron-Antineutrino Disappearance at Daya Bay. *Physical Review Letters*, 108:171803, Apr 2012. doi:10.1103/PhysRevLett.108.171803.

[ABB+15] J. F. Amsbaugh, J. Barrett, A. Beglarian, et al. Focal-Plane Detector System for the KATRIN Experiment. *Nuclear Instruments and Methods in Physics Research Section A: Accelerators, Spectrometers, Detectors and Associated Equipment*, 778:40–60, April 2015. doi:10.1016/j.nima.2014.12.116.

[ACC+12] J. K. Ahn, S. Chebotaryov, J. H. Choi, et al. Observation of Reactor Electron Antineutrinos Disappearance in the RENO Experiment. *Physical Review Letters*, 108:191802, May 2012. doi:10.1103/PhysRevLett.108.191802.

[Ady16] Márton Ady. Monte Carlo Simulations of Ultra High Vacuum and Synchrotron Radiation for Particle Accelerators. 2016. doi:10.5075/EPFL-THESIS-7063.

[Bah64] John N. Bahcall. Solar Neutrino Cross Sections and Nuclear Beta Decay. *Physical Review*, 135(1B):B137–B146, July 1964. doi:10.1103/PhysRev.135.B137.

[BB02] Edwin N. Lightfoot Byron Bird, Warren E. Stewart. *Transport phenomena.* J. Wiley, 2002.

[Bre73] Donald Breck. *Zeolite molecular sieves: structure, chemistry, and use.* Wiley, New York, 1973.

[BSB05] John N. Bahcall, Aldo M. Serenelli, and Sarbani Basu. New Solar Opacities, Abundances, Helioseismology, and Neutrino Fluxes. *The Astrophysical Journal Letters*, 621(1):L85, January 2005. doi:10.1086/428929.

[Cha14] J. Chadwick. Intensitätsverteilung im magnetischen Spectrum der β-Strahlen von radium B + C. *Verhandl. Dtsc. Phys. Ges.*, 1914.

[CRH+56] C. L. Cowan, F. Reines, F. B. Harrison, H. W. Kruse, and A. D. McGuire. Detection of the Free Neutrino: A Confirmation. *Science*, 124(3212):103–104, July 1956. doi:10.1126/science.124.3212.103.

[CS70] Cercignani C. Chapman S., Cowling T.G. *The Mathematical Theory of Non-uniform Gases*. Cambridge University Press, 1970.

[Dav94] Raymond Davis. A Review of the Homestake Solar Neutrino Experiment. *Progress in Particle and Nuclear Physics*, 32:13–32, January 1994. doi:10.1016/0146-6410(94)90004-3.

[Day07] C Day. Basics and applications of cryopumps, 2007. doi:10.5170/CERN-2007-003.241.

[dFT+18] P.F. de Salas, D.V. Forero, C.A. Ternes, M. Tórtola, and J.W.F. Valle. Status of neutrino oscillations 2018: 3σ hint for normal mass ordering and improved CP sensitivity. *Physics Letters B*, 782:633 – 640, 2018. doi:https://doi.org/10.1016/j.physletb.2018.06.019.

[DGG+62] G. Danby, J-M. Gaillard, K. Goulianos, et al. Observation of High-Energy Neutrino Reactions and the Existence of Two Kinds of Neutrinos. *Physical Review Letters*, 9(1):36–44, July 1962. doi:10.1103/PhysRevLett.9.36.

[DHH68] Raymond Davis, Don S. Harmer, and Kenneth C. Hoffman. Search for Neutrinos from the Sun. *Physical Review Letters*, 20(21):1205–1209, May 1968. doi:10.1103/PhysRevLett.20.1205.

[DMVV16] S. Dell'Oro, S. Marcocci, M. Viel, and F. Vissani. Neutrinoless Double Beta Decay: 2015 Review. *Advances in High Energy Physics*, 2016:1–37, 2016, 1601.07512. doi:10.1155/2016/2162659.

[ET20] (2003) Engineering ToolBox. Emissivity coefficients materials, February 2020. URL `https://www.engineeringtoolbox.com/emissivity-coefficients-d_447.html`.

[FHI+98] Y. Fukuda, T. Hayakawa, E. Ichihara, et al. Evidence for Oscillation of Atmospheric Neutrinos. *Physysical Review Letters*, 81:1562–1567, Aug 1998. doi:10.1103/PhysRevLett.81.1562.

[Fri17] Fabian Friedel. *Studien Zur Inbetriebnahme Der Kryogenen Pumpstrecke Des KATRIN-Experiments*. Masterthesis, Karlsruher Institut für Technologie, January 2017.

[fS81] International Organization for Standardization. ISO 3529-2:1981(en), Vacuum technology — Vocabulary — Part 2: Vacuum pumps and related terms, December 1981. URL `https://www.iso.org/`.

[Fur39] W. H. Furry. On Transition Probabilities in Double Beta-Disintegration. *Physical Review*, 56(12):1184–1193, December 1939. doi:10.1103/PhysRev.56.1184.

[GBH+13] S. Grohmann, T. Bode, M. Hötzel, et al. The thermal behaviour of the tritium source in KATRIN. *Cryogenics*, 55-56:5 – 11, 2013. doi:https://doi.org/10.1016/j.cryogenics.2013.01.001.

[Gil80] John T. Gill. Effect of Container Preparation on the Growth of Protium and Methane Impurities into Tritium Gas. *Journal of Vacuum Science and Technology*, 17(2):645–654, March 1980. doi:10.1116/1.570532.

[Gmb13] Pfeiffer Vacuum GmbH. *The Vacuum Technology Book Volume 2*. Pfeiffer Vacuum GmbH, April 2013. URL `https:`

//www.pfeiffer-vacuum.com/filepool/file/vacuum-technology-book/vacuum-technology-book-ii-part-2.pdf?referer=1456&request_locale=en_US.

[Goe35] M. Goeppert-Mayer. Double Beta-Disintegration. *Physical Review*, 48(6):512–516, September 1935. doi:10.1103/PhysRev.48.512.

[Gro19] SHI Cryogenics Group. Rdk - 415d 4k cryocooler series, December 2019. URL http://www.shicryogenics.com/products/4k-cryocoolers/rdk-415d-4k-cryocooler-series/.

[Har15] Fabian Thomas Harms. Characterization and Minimization of Background Processes in the KATRIN Main Spectrometer. 2015. doi:10.5445/ir/1000050027.

[HH06] Hans C. Wolf Hermann Haken. *Molekülphysik und Quantenchemie*. Springer Berlin Heidelberg, 2006. URL https://www.ebook.de/de/product/5165902/hermann_haken_hans_c_wolf_molekuelphysik_und_quantenchemie.html.

[Hub20] Anton Huber. *Analysis of first KATRIN dataand searches for keV-scalesterile neutrinos*. PhD thesis, Karlsruher Instituts für Technologie, 2020.

[Hö12] Markus Hötzel. *Simulation and Analysis of Source-Related Effects for KATRIN*. PhD thesis, KIT, Karlsruhe, 2012. doi:10.5445/IR/1000031259.

[IKM15] Ahmad Fauzi Ismail, Kailash Chandra Khulbe, and Takeshi Matsuura. *Gas Separation Membranes*. Springer-Verlag GmbH, 2015. URL https://www.ebook.de/de/product/24291522/ahmad_fauzi_ismail_kailash_chandra_khulbe_takeshi_matsuura_gas_separation_membranes.html.

[JKS98] W Jitschin, S Khodabakhshi, and PJ Szwemin. Strömungsleitwert der dünnen Blende. *Vakuum in Forschung und Praxis*, 10(4):316–320, 1998.

[Jou04] Karl Jousten, editor. *Wutz Handbuch Vakuumtechnik*. Vieweg+Teubner Verlag, Wiesbaden, 2004. doi:10.1007/978-3-322-96971-2.

[Kle19] Manuel Klein. *Tritium ions in KATRIN: blocking, removal and detection*. PhD thesis, Karlsruher Institut für Technologie (KIT), 2019. doi:10.5445/IR/1000093526. 51.03.01; LK 01.

[Kof15] Jared Nance Kofron. *A Novel Method for Electron Energy Measurement: Cyclotron Radiation Emission Spectroscopy*. PhD Thesis, 2015.

[KUA+01] K. Kodama, N. Ushida, C. Andreopoulos, et al. Observation of tau neutrino interactions. *Physics Letters B*, 504(3):218–224, apr 2001. doi:10.1016/s0370-2693(01)00307-0.

[Lid03] David Lide. *CRC handbook of chemistry and physics : a ready-reference book of chemical and physical data*. CRC Press, Boca Raton, Fla, 2003.

[Lin97] Peter Linstrom. Nist chemistry webbook, nist standard reference database 69, 1997. doi:10.18434/T4D303.

[LP14] Julien Lesgourgues and Sergio Pastor. Neutrino Cosmology and Planck. *New Journal of Physics*, 16(6):065002, June 2014. doi:10.1088/1367-2630/16/6/065002.

[MI20] Inc. MKS Instruments. *Gas Correction Factors for Ionization Vacuum Gauges*, March 2020. URL https://www.mksinst.com/n/gas-correction-factors-for-ionization-vacuum-gauges.

[MKS20] MKS. 722B 1-25,000 Torr, General Purpose Absolute Baratron Capacitance Manometer. Technical report, March 2020. URL https://www.mksinst.com/f/722b-compact-absolute-capacitance-manometers.

[MS86] S. P. Mikheyev and A. Yu. Smirnov. Resonant Amplification of ν Oscillations in Matter and Solar-Neutrino Spectroscopy. *Il Nuovo Cimento C*, 9(1):17–26, January 1986. doi:10.1007/BF02508049.

[MYFP06] Scott Matteucci, Yuri Yampolskii, Benny D. Freeman, and Ingo Pinnau. *Transport of Gases and Vapors in Glassy and Rubbery Polymers*, chapter 1, pages 1–47. John Wiley and Sons, Ltd, 2006, https://onlinelibrary.wiley.com/doi/pdf/10.1002/047002903X.ch1. doi:10.1002/047002903X.ch1.

[PAB+75] M. L. Perl, G. S. Abrams, A. M. Boyarski, et al. Evidence for Anomalous Lepton Production in $e^+ - e^-$ Annihilation. *Physical Review Letters*, 35(22):1489–1492, December 1975. doi:10.1103/PhysRevLett.35.1489.

[Par18] Particle Data Group. Review of Particle Physics. *Physical Review D*, 98(3):030001, August 2018. doi:10.1103/PhysRevD.98.030001.

[Pau64] Wolfgang Pauli. Collected Scientific Papers. 2 Vols. Edited by r. Kronig and VF Weisskopf. 1964.

[Per08] Donald H. Perkins. *Particle Astrophysics*. Oxford University Press, 2008. URL https://www.ebook.de/de/product/7769984/donald_h_perkins_particle_astrophysics.html.

[Pfe20] Pfeiffer. *HiPace80*, 2020. URL https://www.pfeiffer-vacuum.com/en/products/vacuum-generation/turbopumps/hybrid-bearing/hipace-80/32024/hipace-80.

[Pla14] Planck Collaboration. Planck 2013 Results. XVI. Cosmological Parameters. *Astronomy & Astrophysics*, 571:A16, November 2014. doi:10.1051/0004-6361/201321591.

[Pon68] Bruno Pontecorvo. Neutrino Experiments and the Problem of Conservation of Leptonic Charge. *Sov. Phys. JETP*, 26(984-988):165, 1968.

[Pri13] Florian Priester. *Tritiumtechnologie für die fensterlose Quelle WGTS von KATRIN*. PhD Thesis, KIT, Karlsruhe, 2013. doi:10.5445/IR/1000035699.

[PSB15] Florian Priester, Michael Sturm, and Beate Bornschein. Commissioning and detailed results of KATRIN inner loop tritium processing system at Tritium Laboratory Karlsruhe. *Vacuum*, 116:42 – 47, 2015. doi:https://doi.org/10.1016/j.vacuum.2015.02.030.

[Rö19] Carsten Röttele. *Tritium suppression factor of the KATRIN transport section*. PhD thesis, Karlsruher Institut für Technologie (KIT), 2019. doi:10.5445/IR/1000096733. 51.03.01; LK 01.

[Sch16] Kerstin Schönung. *Development of a Rear Wall for the KATRIN Rear Section and investigation of tritium compatibility of Rear Section components*. PhD thesis, Karlsruher Institut für Technologie (KIT), 2016. doi:10.5445/IR/1000056077.

[Vac03] Pfeiffer Vacuum. *Working with Turbopumps, Introduction to high and ultra high vacuumproduction*. 2003. URL https://mmrc.caltech.edu/Vacuum/PfeifferTurbo/Turbos.pdf.

[vW35] C. F. v. Weizsäcker. Zur Theorie der Kernmassen. *Zeitschrift für Physik*, 96(7):431–458, July 1935. doi:10.1007/BF01337700.

[Win11] Alexander Windberger. Berechnungen und Simulationen zumVerhalten von Ionen in derdifferenziellen Pumpstrecke desKATRIN-Experiments. Master's thesis, Karlsruher Institut für Technologie, 2011.

[Wol78] L. Wolfenstein. Neutrino Oscillations in Matter. *Physical Review D*, 17(9):2369–2374, May 1978. doi:10.1103/PhysRevD.17.2369.

[Zub11] Kai Zuber. *Neutrino Physics*. CRC press, 2011.

Acknowledgement

Ich danke Herrn Professor Drexlin für die Möglichkeit am KATRIN Experiment meine Masterarbeit zu schreiben und Frau Professorin Valerius für die Zweitkorrektur dieser Arbeit.

Ein großer Dank geht an Dr. Carsten Röttele für seine Betreuung, konstruktive Kritik und das Korrekturlesen dieser Arbeit.

Ein weiterer Dank geht an alle MitarbeiterInnen im Ingenieur- und Elektrik-Team von KATRIN, die mir immer hilfreich zur Seite standen.